INAUGURAL-DISSERTATION

Sebastian Dedera - 2015

INAUGURAL - DISSERTATION

zur Erlangung der Doktorwürde
der
Naturwissenschaftlich-Mathematischen Gesamtfakultät
der
Ruprecht-Karls-Universtität Heidelberg

vorgelegt von
Diplom-Geologe Sebastian Dedera
aus Bad Schönborn-Mingolsheim

Tag der mündlichen Prüfung: 21. 07. 2015

Visualization of Ion-Induced Tracks in Carbonate Minerals

Gutachter: apl. Prof. Dr. Ulrich A. Glasmacher
Prof. Dr. Christina Trautmann

Keywords: visualization of ion-induced tracks, swift heavy ion irradiation, calcite, dolomite, aragonite, malachite, visualization by etching techniques, EDTA + acetic acid, HNO_3, characterization and statistics of etch pits, preperation of calcite for ion irradiation, thermal neutrons, characterization of dislocations, annealing of etch pits and dislocations, online Raman measurements, UV-light excitation

ACKNOWLEDGEMENT

My very special thanks go to my supervisor apl. Prof. Dr. Ulrich A. Glasmacher, who introduced me to the world of materials science and made this study possible. I also want to thank Prof. Dr. Christina Trautmann who kindly agreeing to write an expertise for the present doctoral thesis, and for all her help concerning questions of ion-irradiation.

I want to thank the materials research group of Prof. Dr. Christina Trautmann at GSI for all their support and advice during the beamtimes, and for accepting me as part of the group.

I want to thank all my colleagues in Heidelberg for all the fruitful discussions and for moral support in hard times. In particular I want to thank Margit Brückner for the priceless support in the chemistry laboratory and Hans Ebert for his help and patience while designing and constructing the accessories for the Online Raman System.

I gratefully acknowledge the financial support provided by the BMBF within the framework of the "BMBF Verbundprojekte" 05KK7VH1 and 05K13VH1.

I want to thank all my friends for their support, especially my roommate Arif who always had a ready ear for my problems.

My special thanks go to my parents for their unconditional support and their endless patience during my doctoral study.

Thank you very much!

ABSTRACT

The present study addresses the visualization of ion-induced tracks in calcite crystals by etching and spectrographic techniques with respect to the question, whether calcite ($CaCO_3$) can be used as an archive for fission-track dating. Due to the erratic uranium content of calcite and the consequent uncertain areal density of fission tracks, artificial tracks, the ion tracks, had to be produced to create a basis of tracks which could be used for etching experiments. To create these artificial ion tracks in natural samples, calcite crystals were irradiated with swift heavy ions (2.18 GeV) at the Universal Linear Accelerator (UNILAC), GSI Helmholtzzentrum für Schwerionenforschung, Darmstadt. The resulting ion tracks were used for the etching experiments described in this study.

The **main research objective** focused on the visualization of ion-induced tracks in calcite by etching techniques. Therefore, published etching procedures were tested for their usability to visualize induced or natural tracks on the calcite's surface. To obtain optimal results, and to gain general knowledge about etching procedures, the existing etching recipes had to be modified. The parameters modified were the concentration of the etching agent, the etching time and the etching temperature which should not exceed 30 °C in order to avoid accidental annealing of the tracks through thermal processes within the crystal lattice. Additionally, the etching process should be as safe as possible, with etching solutions as non-toxic as possible. The experiments revealed two etching solutions suitable to visualize ion-induced tracks in calcite: Na-EDTA + 5 % acetic acid at a temperature of 21 °C, and 0.091 % HNO_3 at a temperature of 15 °C. Na-EDTA + 5 % acetic acid reveals pseudohexagonal etch pits with a length of about 10 µm and a width of about 8 µm after 20 s of etching. HNO_3 reveals pseudopentagonal etch pits with a length of about 9 µm and a width of about 7 µm after an etching time of 4 s. The etch pits are very shallow, with a depth of about 300 nm after 20 s, respectively 4 s of etching. Both etching procedures are optimized to reveal non-overlapping etch pits for an areal density of the tracks of 1×10^6 tracks/cm^2. The fact that these two etching solution reveal different shapes of the etch pits confirms investigations in the literature, some of them very old, which also report different shapes of the etch pits for every etching agent used. These two etching solutions were also used successfully to etch tracks in calcite crystals induced by irradiation with fission fragments of about 170 MeV. Results showed that the etching behavior of fission fragments caused tracks is almost the same as the etching behavior of tracks caused by swift heavy ions. Additionally, the annealing behavior of the tracks was investigated. Tracks induced by irradiation with swift heavy ions anneal when exposed to temperatures of about 240 °C for 100 h, whereas natural dislocations in the crystal lattice do not anneal at this temperature. Thus annealing presents an interesting tool to distinguish between artificial tracks and natural dislocations. Overall, experiments showed, that calcite can be used as an archive for fission-track dating, if the uranium content is high enough.

The **second objective** dealt with the visualization of irradiation damage using non-destructive research methods. This part of the study deals with the characterization and quantification of ion-induced damage in calcite crystals by spectrographic methods. For this purpose, an online Raman measurement system was installed at the multipurpose chamber at the M3 beamline at GSI. With this system it is possible to measure Raman spectra of the samples before, during, and after irradiation with swift heavy ions. This makes it possible to detect ion-induced changes in the Raman bands of the calcite investigated. Experiments showed that calcite forms a new Raman band at 435 cm^{-1} at fluences above 5×10^{10} ions/cm^2. Additionally, malachite was investigated and was found to show various changes in its Raman signal when irradiated with swift heavy ions. To obtain an independent measurement procedure for the fluence applied to a sample by irradiation with swift heavy ions, an experiment was performed based

on the photoluminescence of irradiated calcite when excited by UV light. Experiments showed that the greenish photoluminescence of irradiated areas in calcite increases in intensity with increasing fluence. This approach might be a powerful new tool to determine fluences applied to samples and has to be further developed, because it is sensitive even to very low fluences of 1×10^6 ions/cm^2.

A **third part** of this thesis addresses technical issues like the preparation of samples for the irradiation with swift heavy ions. Etching experiments showed, that the surface of the calcite crystals has to be as smooth as possible, otherwise the desired etch pits will be obscured by the etched crystal-topography. Therefore, a preparation procedure for calcite samples has been developed, which produces almost perfectly smooth surfaces, which can display etched ion tracks. Additionally, a procedure was tested which is able to automatically count the etch pits on the crystals with the help of an image processing software and therefore can determine the areal density of the etch pits on an irradiated samples within seconds.

ZUSAMMENFASSUNG

Die vorliegende Doktorarbeit behandelt die Visualisierung von Defekten in Kalzit Kristallen durch Ätztechniken und spektrografische Methoden in Bezug auf die Fragestellung, ob Kalzit als Archiv für Fission-Track Dating genutzt werden kann. Da der Urangehalt und damit auch die Dichte der Spaltspuren im Kalzit sehr stark variieren, wurden künstliche Defekte im Kristallgitter erzeugt, um eine Basis für die auszuführenden Experimente zu schaffen. Um diese künstlichen Defekte, die Ionenspuren, in natürlichen Proben zu erzeugen, wurden Kalzit Kristalle im Universal Linear Accelerator (UNILAC) des GSI Helmholtzzentrums für Schwerionenforschung in Darmstadt mit Schwerionen bestrahlt (2.18 GeV). Die so erzeugten Ionenspuren wurden für die Ätzexperimente benutzt.

Der **Forschungsschwerpunkt** richtete sich auf die Visualisierung von ioneninduzierten Defekten in Kalzit durch Ätztechniken. Zu diesem Zweck wurden bereits veröffentlichte Ätzprozeduren auf ihre Tauglichkeit getestet, induzierte oder natürliche Defekte (Dislokationen) auf der Oberfläche der Proben darzustellen. Um optimale Ergebnisse zu erzielen und um Basiswissen über Ätzprozesse aufbauen zu können, mussten die vorhandenen Ätzrezepte modifiziert werden. So wurden die Konzentration der Ätzlösung, die Ätzdauer und die Ätztemperatur abgeändert. Dabei sollte die Ätztemperatur 30 °C nicht überschreiten, um ein versehentliches Ausheilen der Defekte im Kristallgitter zu verhindern. Zusätzlich sollte der Ätzvorgang so sicher wie möglich sein, indem man möglichst ungiftige Ätzlösungen verwendet. Durch Experimente ergaben sich zwei Ätzlösungen, die geeignet sind, ioneninduzierte Defekte in Kalzit darzustellen: Na-EDTA + 5 % Essigsäure bei einer Ätztemperatur von 21 °C und 0,091 % HNO_3 bei einer Temperatur von 15 °C. Bei der Ätzung mit Na-EDTA + 5 % Essigsäure entstehen nach 20 s Ätzdauer pseudohexagonale Ätzgruben mit einer Länge von ungefähr ca. 10 µm und einer Breite von ungefähr ca. 8 µm. Ätzungen mit HNO_3 ergeben nach 4 s Ätzdauer pseudo-pentagonale Ätzgruben mit einer Länge von ca. 9 µm und einer Breite von ca. 7 µm. Die Ätzgruben sind mit einer Tiefe von ca. 300 nm nach 20 s Ätzdauer mit Na-EDTA + 5 % Essigsäure, bzw. 4 s Ätzdauer mit 0.091 % HNO_3, sehr flach. Beide Ätzprozeduren sind auf eine Defektdichte von 1×10^6 Defekte/cm^2 ausgelegt, das heißt, idealerweise sind die Ätzgruben voll ausgebildet und überlappen sich nicht. Die Tatsache, dass die beiden genutzten Ätzlösungen unterschiedliche Formen der Ätzgruben ergeben, bestätigt die teilweise sehr alte gesichtete Literatur, die für jede genutzte Ätzlösung eine andere Form der Ätzgruben beschreibt. Die beiden dargestellten Ätzlösungen wurden auch erfolgreich zur Visualisierung von Defekten eingesetzt, die durch Spaltprodukte mit einer Energie von ca. 170 MeV entstanden sind. Die Ergebnisse zeigten, dass das Ätzverhalten der Defekte sehr ähnlich ist, unabhängig davon, ob sie durch hochenergetischen Schwerionen oder mit Spaltprodukten mit niedrigen Energien erzeugt wurden. Des Weiteren wurde das Verheilungsverhalten der Defekte untersucht. Künstlich induzierte Defekte verheilen bei einer Temperatur von ca. 240 °C bei einer Heizdauer von 100 h, wohingegen natürliche Dislokationen bei dieser Temperatur nicht verheilen. Mithilfe dieser Technik lässt sich relativ einfach zwischen natürlichen Dislokationen und künstlich induzierten Defekten unterscheiden. Zusammenfassend lässt sich sagen, dass Kalzit als Archiv für Fission-Track Dating benutzt werden kann, falls der Urangehalt des Kalzits hoch genug ist.

Die **zweite Fragestellung** beschäftigt sich mit der zerstörungsfreien Visualisierung von Schäden im Kristallgitter, die durch die Bestrahlung mit Schwerionen hervorgerufen wurden. Dieser Teil der Arbeit beinhaltet die Charakterisierung und Quantifizierung von ioneninduzierten Schäden in Kalzit Kristallen durch spektrografische Methoden. Dazu wurde an der Spektroskopiekammer des M3-Strahlzweiges der GSI ein online Ramansystem aufgebaut. Mit diesem System ist es möglich, Ramanspektren der Probe vor, während und nach der Bestrahlung mit Schwerionen zu messen. So lassen sich durch die Bestrahlung

mit Ionen hervorgerufene Veränderungen der Ramanbanden des untersuchten Kalzits detektieren. Die Untersuchungen zeigten, dass Kalzit ab einer Fluenz von 5×10^{5} Ionen/cm^{2} eine neue Ramanbande bei 435 cm^{-1} ausbildet. Zusätzlich wurde Malachit mit dem neuen System untersucht. Dieser zeigt vielfältige Veränderungen seines Ramanspektrums durch die Bestrahlung mit Schwerionen. Des Weiteren wurde ein Experiment, basierend auf der UV-Licht induzierten Fotolumineszenz von mit Schwerionen bestrahltem Kalzit durchgeführt. Dieses Experiment hatte zum Ziel, eine von der Ätzung von PC-Folien unabhängige Bestimmung der induzierten Fluenz zu erhalten. Die Resultate zeigten, dass die grünliche Fotolumineszenz von bestrahltem Kalzit mit steigender Fluenz zunimmt. Dieser vielversprechende Ansatz könnte sich zu einer neuen Methode zur Messung der induzierten Fluenz entwickeln, da die Methode auch für sehr niedrige Fluenzen von 1×10^{6} Ionen/cm^{2} nutzbar ist.

Der dritte Teil dieser Arbeit beschäftigt sich mit der Lösung technischer Herausforderungen, wie z. B. die Vorbereitung von Proben für die Bestrahlung mit Schwerionen. Ätzexperimente zeigten, dass die Oberflächen von Kalzit sehr eben sein müssen, damit die gewünschten Ätzgruben nicht von der angeätzen Kristalltopographie überlagert werden und somit nicht zu sehen sind. Deswegen wurde ein Herstellungsverfahren für Kalzitproben entwickelt, das fast perfekt glatte Oberflächen hervorbringt, auf der die Ätzgruben sichtbar sind. Zusätzlich wurde eine Methode entwickelt, die in der Lage ist, mit Hilfe einer Bildverarbeitungssoftware automatisch die Anzahl der Ätzgruben zu zählen und die Flächendichte der Ätzgruben in Sekundenschnelle bestimmt.

TABLE OF CONTENTS

1

INTRODUCTION

The visualization of ion tracks in carbonate minerals is of major interest for geological methods to determine the thermal history of rocks, and subsequently understand long-term landscape evolution by using the acquired data for numerical models that describe the history of landscapes. Carbonate minerals such as calcite ($CaCO_3$) are abundant in carbonate rocks, forming whole landscapes with huge caves and ore deposits in nature. Calcite stalagmites and stalactites are used for reconstruction of the ancient climate history by combining the dating technique U-Th disequilibrium with oxygen and carbon stable isotopes (Fleitmann et al., 2003). This dating technique is only applicable up to a formation age of about 400 kyr. The formation of older carbonate minerals has been dated so far by applying the (U-Th)/He dating technique (Copeland et al., 2007, Cros et al., 2014). Unfortunately, this dating technique has the analytical obstacle of non-radiogenic helium stored in fluid inclusions in carbonate minerals (Kluge et al. 2008, Scheidegger et al. 2008). A dating technique that does not require isotopes as the daughter products would be ideal in geological environments. Therefore, it is of significant importance to test the capability of carbonate minerals, especially calcite, to be used for the established dating technique of fission-track dating which is based on the ^{238}U fissioning dependent accumulation of linear crystal defects.

Visualization of fission tracks in calcite can be performed by etching the fission-tracks, thus enlarging the etch pits to dimensions that can be viewed with an optical microscope. In addition, spectroscopic techniques such as Raman and UV-spectroscopy can be used to visualize the volume density of fission tracks without destroying the spontaneous fission tracks by etching. (Pabst et al., 2011)

Only two independent research studies on visualization of fission-tracks in calcite by etching have been published so far (Sippel & Glover, 1964; Macdougall & Price, 1974). Whereas Sippel and Glover indicated the possibility of using calcite as a thermochronological tool by describing possible etching techniques, Macdougall and Price discarded calcite as a thermochronological dating tool on the basis of their statement, that the fission tracks anneal at ambient temperatures. To my knowledge, no further research on fission-track dating of calcite or other carbonate minerals has been performed since 1974.

To unravel the discrepancy between these two publications, a new research study was initiated with the aim of establishing a reproducible etching procedure for calcite crystals in order to reveal etch pits from artificial ion tracks, natural dislocations, and from fission tracks in natural calcite crystals. Other objectives were to describe, differentiate and quantify the great variety of etch pits. Accelerated heavy ions were used to create a defined density of ion tracks in calcite, as the natural ^{238}U-concentration in calcite is very variable. This defined areal density of ion tracks helps to distinguish between the etch pits of ion tracks and etch pits of dislocations of the crystal lattice. The samples were irradiated with swift heavy ions at the linear accelerator UNILAC at the GSI Helmholtzzentrum für Schwerionenforschung GmbH, in Darmstadt. This thesis is divided into several different projects, which build upon each other's results. Each project is individually discussed at the end of the relevant chapter. Additionally, a final conclusion can be found at the end of this doctoral thesis.

2

LITERATURE RESEARCH

CONTENTS

2.1 HISTORY OF MINERAL ETCHING

Minerals and gems have fascinated human beings for centuries. Therefore it is no surprise that knowledge of the structure of minerals was of general interest very early on. The following chapter provides a brief overview of the history of etching minerals.

2.1.1 The 19th century

The etching of minerals to investigate their crystal structure has a long history in mineralogy, especially in Germany and Austria. Basic research has been done, starting at the beginning of the 19th century and peaking initially in the 1880s.

In 1894, HEINRICH BAUMHAUER published a first overview of the works of his contemporaries and wrote a first compendium on methods for etching crystals including apatite, dolomite, magnesite and siderite. In his *"Die Resultate der Aetzmethode in der krystallographischen Forschung" (Results of the etching method for use in crystallographic research)* he gives a historic recapitulation and summarizes many very important observations and results, many of which are still valid today (Fig. 2.1).

According to BAUMHAUER, the first etching of crystals was performed by DANIELL in 1817. He tested many minerals for their solubility and discovered that different etching solutions work with different minerals, for example hydrochloric acid with calcite. The next important work was published almost 40 years later by FRANZ LEYDOLT in 1854. He delivered the first real scientific research on the etching of minerals to investigate their crystal structure.

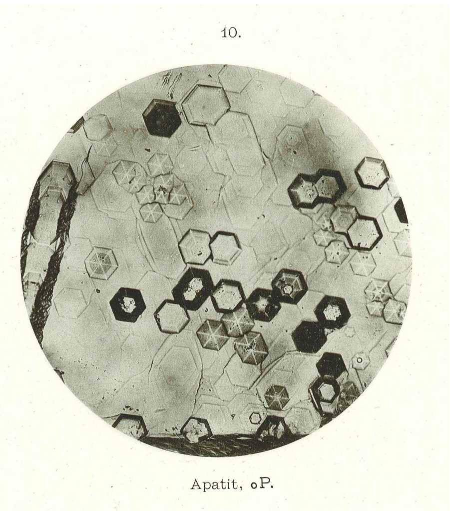

Fig. 2.1: Image of etched apatite. In Baumhauer 1894

In this work very important general principles of etching are described for the first time. For example, he documents the connection between the shape of the etch pits and the parameters of the etching solution. He notes that different etching solutions and variable concentrations of the same etching solution have a significant effect on the etch pits. He also points out the important role played by the temperature of the etching solution. Additionally, he found out that the etch pits grow depending on the etching time, and that the etch pits overlap if the crystal is etched for too long, which is why he recommends performing the etching under a microscope in order to remove the sample from the etchant at exactly the right point.

Then in the 1880s there was a first rush of interest in the etching method. Many mineralogists like VIKTOR VON EBNER, FRIEDRICH KLOCKE, GUSTAV TSCHERMACK and FRIEDRICH BECKE performed extensive experiments on etching minerals, mainly to investigate the crystal structure of the minerals examined (BECKE, F., 1925; KÖHLER, A., 1925).

Especially the work of VIKTOR VON EBNER, who investigated the solubility of calcite and aragonite in 1884 and 1885, is of importance for this doctoral thesis. In his publication *"Die Lösungsflächen des Kalkspathes und des Aragonites" (The dissolution planes of calcite and aragonite)* he investigated the shape of "etch figures" in calcite and aragonite with numerous different etching solutions in different concentrations at different temperatures. His work will be reviewed in detail in Chapter 7.3.

2.1.2 The 20th century

Over the next decades, at the beginning of the 20th century many others focused on the etching of minerals with the aim of learning more about the crystal structure. In the 1930s, the group of

Prof. Dr. O. Erdmannsdörfer in Heidelberg, and especially his student Wilhelm Kleber (who today is known as the founder of the modern crystallography), continued the crystallographic research. He published various papers on the topic of dissolution of minerals. A complete list of Kleber's work can be found in H. Wondratschek´s obituary of Willhelm Kleber from 1971. Other important works of this period are: Honess & Jones (1937), who investigated the etch figures of minerals etched with optically active solvents, and Boos (1942) who performed etching experiments on calcite, rhodochrosite and siderite.

Up to this point, all experiments were performed with the purpose of determining the crystal structure of the minerals and their symmetries by studying the shape of the etch pits and the etching speed of the latter. Before the invention of XRD in 1913 (Friedrich et al. 1913, Bragg et al. 1913) and the establishment of this method in the 1940s, etching of minerals was the only possibility to determine the crystal structure.

In the 1960s some experiments were performed aiming to visualize small defects on the crystal surface. Especially the works of Keith & Gilman (1960) and Thomas & Renshaw (1964) are important. Both teams dealt with the visualization and characterization of dislocations on the crystal surface using etching techniques. Moreover, these two studies contain detailed etching recipes. Additionally, these authors also performed first annealing experiments.

After the invention of fission-track dating only two important works have been published which focused on fission damage in carbonate minerals, especially in calcite: Sippel & Glover (1964) and Macdougall & Price (1974). These two papers are of significant importance for this doctoral thesis, so they are discussed in detail in Chaper 2.3. Due to Macdougall & Price's statement in their 1974 paper, no further paper dealt seriously with this topic. Later publications like MacInnis & Brantley (1993) or Lüttge (2003) basically deal with general dissolution kinetics.

2.2 FISSON TRACK DATING - A BRIEF OVERVIEW

The overall objective of this thesis is to ascertain whether carbonate minerals, and especially calcite, are suitable as an archive for thermochronological methods like fission-track dating. Fleischer, Price and Walker published in 1975 a first compendium to fission-track dating.

The following chapter describes in a short overview what thermochronological methods are capable of, and how they work.

Fission-track dating is based on the production of radiation damage, resulting from spontaneous fission, and the subsequent, thermally controlled retention of the spontaneous fission tracks. The radioisotope production decreases exponentially with time, but is predictable and otherwise steady, which gives the thermochronometer the ability to keep time. Due to the thermal sensitivity of thermochronometers, their revealed ages provide information about the cooling history of the rock, rather than the crystallization ages of its minerals (although in cases of very fast cooling of the minerals, they do record crystallization ages as well).

The basic concept of the fission-track dating technique is the spontaneous fission of ^{238}U, during which the heavy fragments of this fission process leave chemically etchable latent tracks in minerals (e. g. apatite, zircon) and natural glasses. Information on the thermal history of the minerals investigated, which are apatite and zircon, for default methods, is stored in three archives: the etch pit areal density on an artificially polished, previously internal surface, the track length distribution, confined to horizontal tracks, and the etch pit size. Fission-track data is mainly used to model the thermal history of rocks and is to determine the cooling and exhumation rates for crustal segments, for example mountain ranges. A good summary and more detailed information about fission-track dating can be found in the book: *Fission-track Dating* by Wagner & van den Haute, published in 1992.

2.3 Overview of former Works to use Calcite for Fission-Track Dating

The usability of calcite for fission-track dating is the subject of controversial discussion in the literature. Basically there are 2 major papers dealing with the application of calcite for fission-track dating, which are introduced in this chapter.

2.3.1 Sippel & Glover 1964

In their paper "Fission Damage in Calcite and the Dating of Carbonates", published in "Science" 1964, Sippel & Glover investigated whether fission-track dating, which had been discovered and developed by Price & Walker (1962a, b) two years earlier, could be performed on calcite crystals. For their investigations they used concentrated formic acid and etched artificially irradiated (U_2O_8 film) Iceland spar crystals for 1 minute. They succeeded in visualizing rectangular etch pits which could not be distinguished from etched dislocations (Fig. 2.2). They then used annealing methods to compare areal densities of annealed and non-annealed crystals. By subtracting the fission tracks – which annealed sooner – from the dislocations, they wanted to arrive at a realistic areal density of the fission tracks. This apparently worked, because their general conclusion was that calcite can very probably be used for fission-track dating.

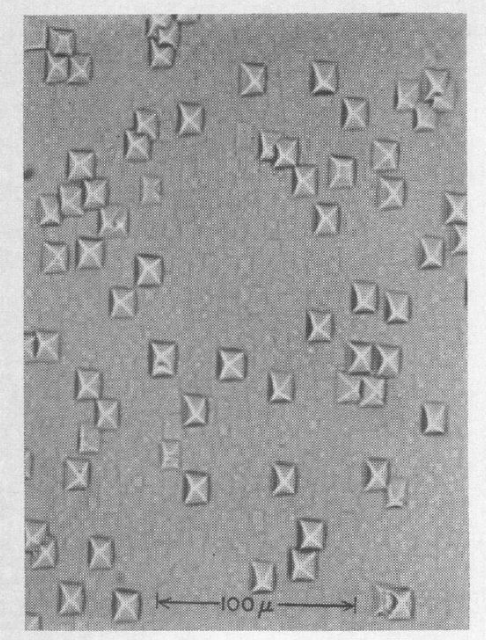

Fig. 2.2: Etch figures of calcite etched with hydrochloric acid, Sippel & Glover 1964

2.3.2 Macdougall & Price 1974

Macdougall & Price wanted to apply the new method, and tried to date calcite hominid fossils from a cave in South Africa using fission-track dating, based on the paper of Sippel & Glover. For their experiments, they used a different etching solution from Sippel & Glover: Na-EDTA + acetic acid, an etching solution developed by Krishnaswami et al. (1971) to etch olivines. Their result was that they failed to get useful data from the calcite samples used, and they stated following reasons:

The calcite used did not accumulate uranium; despite the fact that the bones themselves had a uranium content of around 80 ng/g. According to their research, the fission tracks anneal at ambient temperature, and therefore are gone, if they were ever present. With their final statement: "*... and that in general calcite will not be a useful mineral for fission-track dating*" they basically terminated further research on using calcite for fission-track applications.

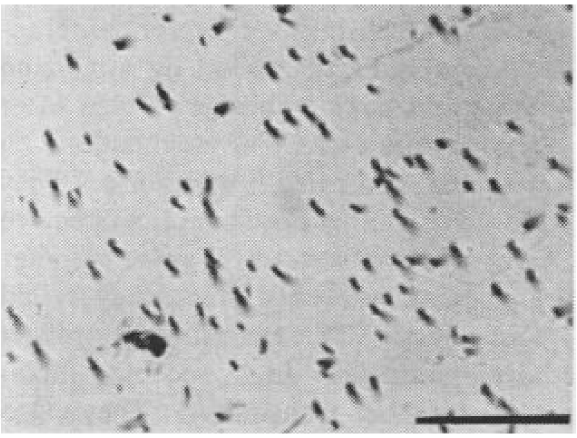

Fig. 2.3: Etch pits in calcite according to Macdougall & Price.

2.3.3 Summary

In general, the two publications had two completely different concepts: Sippel & Glover wanted to test whether it is generally possible to use calcite for fission-track dating, whereas Macdou-

GALL & PRICE wanted to apply the method to a scientific problem. This reveals major differences between the two approaches: Whereas SIPPEL & GLOVER used optimal laboratory conditions with prepared samples irradiated by an external uranium source to get fission tracks, an experimental approach which worked, MACDOUGALL & PRICE used natural samples, their knowledge of which was limited to the uranium content, and their experiments failed.

To summarize, it can be stated that SIPPEL & GLOVER say, based on their good results and positive experiments, that it is possible to use calcite for fission-track dating; 10 years later, MACDOUGALL & PRICE postulate that it is not possible, due to their failure.

2.4 URANIUM CONTENT OF CALCITE

To perform fission-track dating, the mineral under study must have considerable uranium content. Apatite for example, as one of the standard minerals for fission-track dating typically has a uranium content of between 10- 50 µg/g, zircon as the second really important mineral for fission-track dating has a uranium content averaging between 100-300 µg/g. One of the explanations put forward by MACDOUGALL & PRICE as to why they failed in their attempt to get fission-track data from calcite, is that an unsufficient amount of uranium is integrated in the crystal structure. This was the reason for conducting a detailed research on the uranium content of calcite in the present study.

Over the last 10 years many studies have been published for various reasons which deal with the uranium content of calcite. In summary, there are many calcite deposits around the world, some of which have a very high uranium content. Table 2-1 shows an overview of selected publications, but much more literature on this topic is available.

These publications determine uranium content with values of up to 168 µg/g, which is amply sufficient to perform fission-track dating. So already at this early point in this doctoral thesis one important statement of MACDOUGALL & PRICE is doubtable.

2.5 CONCLUSION

The literature research revealed much interesting and helpful information. The conclusions of these publications, some of which are over 100 years old, on aspects such as the influence of etching solution, temperature and etching time on the shape of the etch pits, are very helpful for the upcoming study and will be discussed in detail. Although these etching experiments were performed for a different purpose than the experiments in this study, these old publications provide a great deal of basic knowledge about etching minerals and in some cases surprisingly good images. Due to the lack of more recent data, the etching recipes used in this study are based on recipes of publications from the 1960s, which then were modified to fulfil the requirements of this work.

The most interesting part, however, is the conflict between SIPPEL & GLOVER and MACDOUGALL & PRICE. Although they used different approaches to visualize fission damage in calcite, the great divergence of these two publications is very informative: the basic research of SIPPEL & GLOVER

Tab. 2-1: Overview of the uranium content of calcite

Author	Year	Uranium content [µg/g]	Material
Alcaraz-Pelegrina, A.	2007	0.07- 0.14	Travertine
Andersen et al.	2008	1.78- 2.56	Fossil corrals
Neff, Ph.D Thesis	2001	0.12- 15.56	Stalagmites
Hoffmann et al.	2009	10- 168	Stalagmites

Fig. 2.4: Flow chart oft the progress/development of the doctoral thesis

revealed a general proof of principal, but Macdougall & Price failed in an attempt to apply the method to a real scientific problem. The question is: Is it really not possible to use calcite for fission-track dating, or did Macdougall & Price give up too early? Additionally, the impact of the Macdougall & Price paper is astonishing. Presumably due to the reputation of P. B. Price as one of the founders of the fission-track dating method, no other paper could be found dealing with the suitability of calcite for fission-track dating, as P. B. Price said it would not work. So a fresh review of the results described in these two papers, using modern methods, makes sense. The results of both studies have been reviewed in this doctoral thesis. The comparison of the results of Sippel & Glover and Macdougall & Price respectively with the results of this study can be found in Chapter 7.3.

2.6 Flow Chart

The flow chart of Figure 2.4 shows the progress of this doctoral thesis step by step. The chart is intended to illustrate the chronological order of the experiments, which were performed on the basis of the results already obtained. The flow chart helps to understand why an experiment is performed and what considerations lie behind it.

The stages mentioned below are displayed at the bottom right of each box.

Stage 1

At the beginning of the thesis, a careful literature research was performed, to evaluate former works for their applicability to the new project. Many publications were checked for the following contents: Are there experiences in etching carbonate minerals? Which minerals were etched? Which etching properties (etching solvent, time, temperature) have been used? Why did they etch the minerals? The results of this research are shown in Chapter 2.

Stage 2

Stage 2 includes the first etching experiments based on the results of stage 1. Of the four etching solvents tested, a mixture of a saturated EDTA solution and diluted acetic acid provided the best results. Chapter 5 deals with this stage of the doctoral thesis.

Stage 3

After the first success of stage 2, this stage deals with the optimization of the etching process, the clear definition of the etch pits and first applications. To optimize the EDTA + acetic acid mixture, experiments with the concentration of the acetic acid, the etching time and etching temperature were made (see Chapter 5). After establishing a standard etching recipe, extensive investigations to define the etch pits (3a) and their annealing behavior (3d) were made. These experiments are described in Chapters 9 & 10. Additionally, first experiments with uranium bearing carbonate rocks failed (3b). 3b’ shows the attempt to transfer the etching recipe for calcite to dolomite and aragonite. These experiments failed and the search for a useful etching solution for these minerals was postponed to focus on the etching of calcite. This stage of the thesis also includes the development of a procedure to prepare non-idiomorphic crystals for ion irradiation (3c). This project was completed successfully, resulting in a standard procedure, which is described in Chapter 4.

Stage 4

Stage 4 represents a setback, described in Chapter 6.1. Experiments to etch prepared batches led to a undefined coating in the batches and made them useless. This result led to the developing of an alternate etching solution.

Stage 5

Stage 5, the new etching solvent HNO_3 is the result of the failure of stage 4. Additional literature research and extensive testing revealed a useful and reliable etching solvent that works with

Epofix embedded samples. Chapter 6.2 shows the detailed results of this stage.

Stage 6

Stage 6 includes the improvement of the etching solution discovered in stage 5. In various experiments, concentration, etching time and etching temperature were modified to obtain an optimal etching result. More detailed information is given in Chapter 6.3. The successful testing of the solvent with Epofix embedded samples (6b) and the development of an automated counting procedure to determine the areal density of the etched samples is also described (6c). At this stage of the doctoral thesis, a second attempt to visualize tracks on carbonates with natural uranium content was undertaken. Like the first experiment in stage 3, these experiments were not successful (Chapter 8.2.5) and led to a complete reconsideration of the methods applied (6a).

Stage 7

The reconsideration of the experimental setup to test the ability of calcite to display tracks originating from irradiation fission fragments after the failure of stage 3 and stage 6 led to a complete new setup. At this stage, calcite crystals were covered with (7a) uranium glass for a defined areal density and with zircon grains (7b). This setup led to external penetration of the samples with fission products at natural energy instead of the irradiation from “inside”. Both experiments were very successful and showed that induced fission tracks can be displayed with the developed preparation and etching methods. The results are shown in Chapter 8.

Stage 8

Gives the answer, whether the experiments of this doctoral thesis lead to a satisfying result. A more detailed conclusion can be found in Chapter 13.

3

METHODOLOGY

CONTENTS

3.1 Calcite - Characterization of a Mineral

3.1.1 Carbonate minerals

Calcite is classified as a carbonate mineral (Chang, Howie & Zussman, 1998). Carbonate minerals are abundant in the earth's crust. There are approximately 150 known carbonate minerals but many of them are extremely rare. Carbonate minerals occur in carbonate rocks like limestone (see Chapter 3.1.3), in solution in the oceans of the planet, and in the shell of many animals. The common rock forming carbonate minerals, of which calcite is the most important, are grouped into three main units: The Calcite-, Aragonite- and Dolomite- type.

Basically, carbonates are a group of minerals which have a $[CO_3]^{2-}$ complex in common. The associated cations can have a bigger or smaller ion radius than the Ca^{2+} cation, which has a radius of 1.08 Å. Carbonates with a smaller cation like Mg^{2+}, Zn^{2+}, Fe^{2+} or Mn^{2+} crystallize ditrigonal-scalenoedrically like calcite ($CaCO_3$) and therefore have "Calcite Structure". On the other hand carbonates with a cation > 1.08 Å like Sr^{2+}, Pb^{2+} or Ba^{2+} crystallize rhombically like aragonite and therefore have "Aragonite Structure". This classification system only works for carbonates with a single cation. Carbonates with more than one cation, like the "Dolomite Group" or even more complex structures like the "Azurite-Malachite Group" have other crystal structures. Table 3-1 shows the most common carbonate minerals with their basic properties.

3.1.2 Calcite

Calcite is the most common mineral of the "Calcite Group" within the group of the carbonate minerals. The name calcite comes from the Latin word "calx" which means lime. Consisting of $CaCO_3$, it crystallizes with a trigonal crystal structure and develops different habits (Fig. 3.1). Calcite is very soft, with a hardness (Mohs) of 3, and can have many different colors: most calcites are

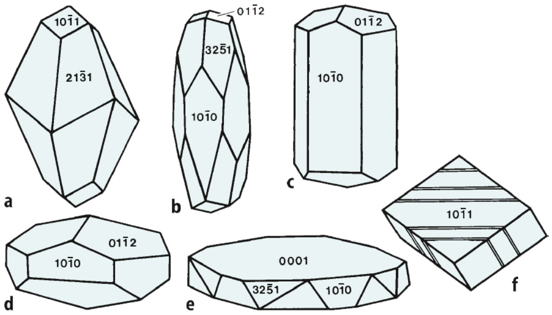

Fig. 3.1: Different habita of Calcite. Okrusch & Matthes (2010)

Tab. 3-1: Most important carbonate minerals. After Okrusch & Matthes 2010

Carbonate	Formula	Density	Ion	Ion radius	Carbonate Group
Calcite	$CaCO_3$	2.71	Ca^{2+}	1.08	Calcite-Group
Siderite	$FeCO_3$	3.97	Fe^{2+}	0.69	
Rhodochrosite	$MnCO_3$	3.70	Mn^{2+}	0.75	
Smithsonite	$ZnCO_3$	4.43	Zn^{2+}	0.83	
Magnesite	$MgCO_3$	3.00	Mg^{2+}	0.80	
Aragonite	$CaCO_3$	2.95	Ca^{2+}	1.26	Aragonite Group
Strontianite	$SrCO_3$	3.7	Sr^{2+}	1.35	
Cerussite	$PbCO_3$	6.55	Pb^{2+}	1.41	
Witherit	$BaCO_3$	4.3	Ba^{2+}	1.55	
Dolomite	$CaMg(CO_3)_2$	2.85	Ca^{2+} Mg^{2+}	1.08 0.80	Dolomite-Group
Ankerite	$CaFe(CO_3)_2$	3.01	Ca^{2+} Fe^{2+}	1.08 0.69	

Tab. 3-2: Properties of calcite. After Chang et. al. (1998)

Physical Properties of Calcite	
Chemical Formula:	$CaCO_3$
Crystal System:	trigonal- hexagonal scalenohedral
Cleavage:	$\{10\bar{1}1\}$ perfect
Twinning:	$\{01\bar{1}2\}$ and $\{0001\}$ common
Color:	Colorless, White, Green, Yellow, Blue, Pink
Diaphaneity:	Transparent to translucent to opaque
Thin section:	Colorless
Density:	2.71 g/cm^3
Hardness (Mohs):	3

colorless, but yellow, green, blue, or even black calcites are possible (Fig. 3.2). Table 3-2 gives an overview of the most important physical properties of calcite. A characteristic property of calcite is its extraordinarily high birefringence (Fig. 3.3). Light entering the crystal is separated into an ordinary and extraordinary ray with different refraction indices. This leads to the effect that objects monitored through the crystal seem to appear twice. This property of calcite is very helpful in identifying calcite, also in thin section investigations. Calcite is barely resistant to weathering: even slightly acetous water can dissolve it. If exposed to acids, calcite dissolves with heavy gassing. Calcite is able to integrate a certain amount of rare earth elements into its crystal structure. This leads to the different colors on the one hand, on the other it leads to a fluorescence in bright colors during excitation with UV light or electrons during cathodoluminescence. Calcite is formed by the reaction:

$$Ca^{2+} + 2HCO_3^- \leftrightarrow CaCO_3 + H_2O + CO_2$$

The equation moves to the right with increasing temperature. This is the reason for the deposition of calcite for example in boilers or cooking pots. Calcite is a widely distributed mineral and is mainly formed sedimentarily. Calcite is the main ingredient of limestone and clay and often forms the matrix of clastic sediments. The biggest reservoirs of calcite are marine deposits on the ocean floors of shallow, intertidal oceanic platforms. As a biogenic mineral, calcite forms the skeletons and shells of countless creatures, such as shellfish or corals. After the death of these animals these materials form carbonate mud mainly consisting of calcite on the ocean floor. With pressure, temperature and time, calcite forms from this carbonate mud. Another and very special reservoir of calcite is the Ol Doinyo Lengai. This volcano in the northern part of Tanzania extracts mainly natrocarbonatite lava but subsequent reaction of the lava with meteoric water results in the formation of several other carbonate minerals including a good amount of calcite. (Dawson,

Fig. 3.2: Calcite crystals with different colors

Fig. 3.3: Demonstration of the double refraction of calcite

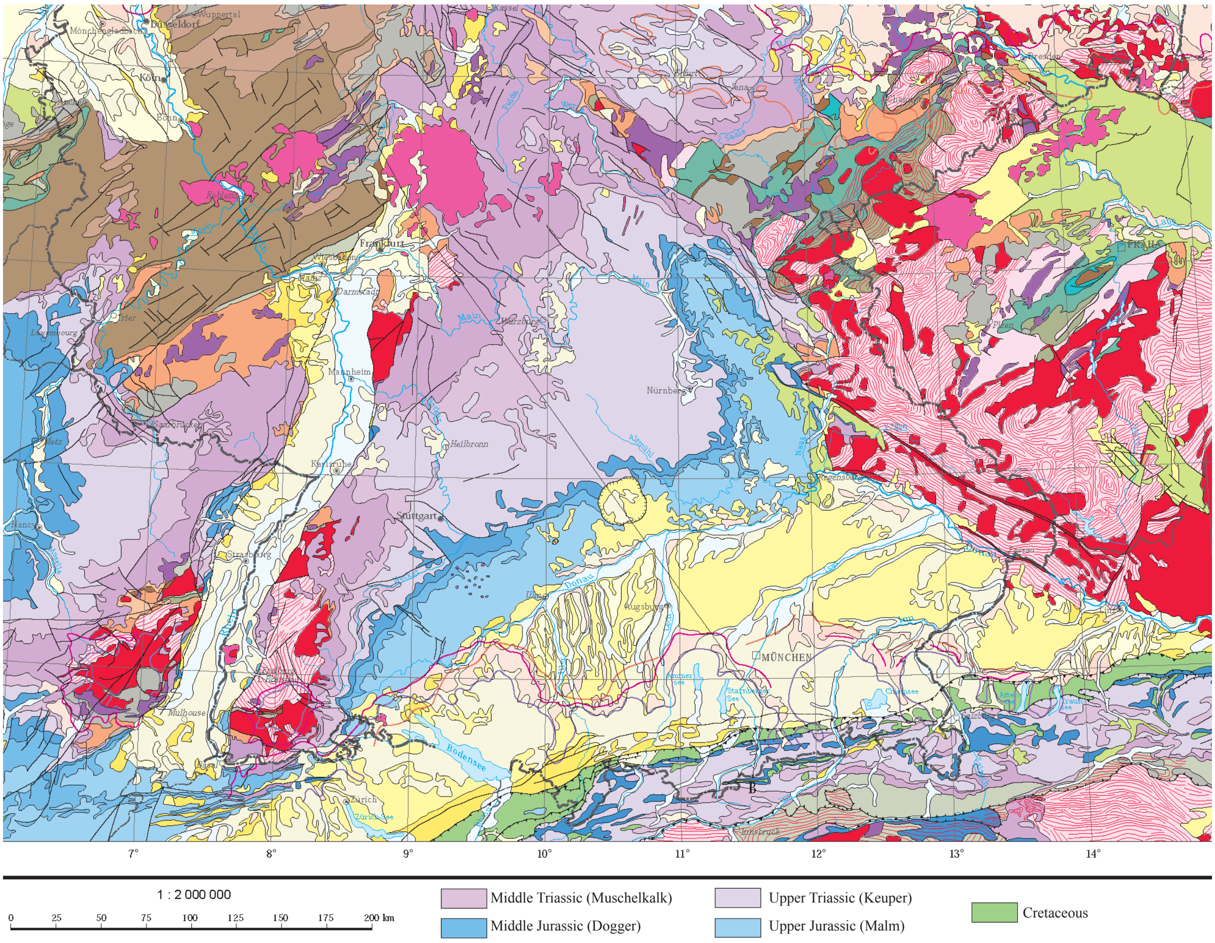

Fig. 3.4: Geological map of Southern Germany. The middle and bright purple sequences are the middle and upper Triassic sequences which bear a major amount of limestone, as do the blue Jurrasic sequences of the Schwäbische Alb and the Fränkische Alb.

1962; Zaitsev & Keller, 2006). Commercially, clear calcite crystals are used in the optical industry. The different carbonate rocks are a very important resource as construction material of various kinds and are used in the chemical industry in the production of glass, pulp and fertilizer.

3.1.3 Calcite in carbonate rocks - limestone

Limestone is a sedimentary rock mainly consisting of the minerals calcite and aragonite. Limestone is abundant in the Earth's crust and a very important rock in geology, and therefore has its own discipline: carbonate sedimentology, which deals with the formation and properties of the different limestones.

Besides its main components calcite and aragonite, limestone can contain other minerals, for example dolomite, quartz, gypsum and clay minerals.

The majority of limestone is formed by biogenic processes, either as pure biogenic limestone, which is formed from rock-forming corals, or as limestone formed by deposition of the shells of fossil microorganisms, mainly coccoliths. The limestone is formed when the microorganisms drop to the ocean floor after death, where they form what is known as carbonate mud. This mud is transformed to limestone by the process of diagenesis. Another form of biogenic carbonate rocks is the limestones which consist of bigger fossils like snails, shellfish or sponges. Apart from the bigger "grain size", these limestones are formed by the same process as limestone from microorganisms. Limestones may also form in lacustrine and evaporite depositional environments. A third possibility for the formation of limestone is clastic sediments. Due to the softness of most carbonate minerals, only very short transportation routes are possible for clastic carbonates. Typically, they can be found underneath a coral reef as carbonate breccia made of reef debris.

Limestones are widely distributed throughout the world. By far the biggest percentage formed on the ocean floor and was then lifted above sea level by tectonic processes. In Europe, landscapes almost completely formed of limestone can be found in the southern part of Germany (Fig. 3.4), the Schwäbische Alb (Swabian Alb), and the Fränkische Alb (Franconian Alb), the Solnhofener Plattenkalk (Solnhofen Limestone, famous for its very rich fossil content) and the Swiss and French Jura. Also well-known are the northern "Kalkalpen" ("Limestone Alps") which form 600 km of mountain range consisting of limestone. Another very famous example of limestone landscapes is the chalk mountains in the North Sea region with the famous White Cliffs of Dover in Kent, England (Fig. 3.5) as well as their counterpart, the Cap Blanc Nez on the other side of the Strait of Dover Strait. These chalk rocks consist almost completely of calcite in a fine grade matrix of microorganisms.

Depending on its properties, limestone is highly variable in various applications, mainly in the construction materials industry. Limestones with a high density are used as a natural building material for every kind of building. Milled limestone is used for the production of concrete, in the glass industry, as a fertilizer, and to neutralize acid in soils. Furthermore, porous limestones are the most important reservoir rock for oil and gas. The biggest oil and gas reservoirs on the Arabian Peninsula are located in reef limestone.

For more information about carbonate minerals, calcite and carbonate rocks, see for example "Rock-Forming Minerals" by Chang, Howie & Zussman, "Mineralogie" by Okrusch & Matthes, or "Allgemeine Geologie" by Press & Siever.

3.2 SAMPLES USED FOR THIS STUDY

3.2.1 Calcite

Calcite samples used in this study are calcite crystals ($CaCO_3$, trigonal) from Eskifjörður, Iceland (12991 collection Heidelberg). The Helgustadir quarry near the village of Eskifjörður, East Iceland is the type location for large, transparent cleavage rhombohedrons of calcite, which therefore are also called Iceland spar. (Kristjanson, 2002). From 1668 to 1925 the quarry supplied large quantities of Iceland Spar.

From the beginning of the 19th century onwards, these crystals were essential in the development of petrographic microscopes, polarimeters and various other optical instruments. The crystals used in this study originally had a feed size of about 3 cm (Fig. 3.12) and were cleaved for further use. A sample of the calcite used in this study has been sent to the ACME Laboratories to perform a geochemical analysis of the mineral. The results show a very clean $CaCO_3$ crystal with almost no other elements than CaO and C. Table 15-6 in the appendix

Fig. 3.5: The White Cliffs of Dover

Fig. 3.6: Aragonite crystals from the Číčov mountain near Hořenec, Czech Republic

shows the detailed results for the geochemical analysis.

3.2.2 Aragonite

The aragonite crystals ($CaCO_3$, orthorhombic) used in this study are from the Čížov Mountain near Hořenec in the Czech Republic. The summit of the Čížov consists of basalt. This summit is a unique location for finding crystalline aragonite of excellent quality. The samples used were originally hexagonal pillars of transparent aragonite approximately 3 cm high with a diameter of about 5 mm (Fig. 3.6). For the experiments, smaller pieces were sawed off the pillars.

3.2.3 Dolomite

The dolomite crystals ($CaMg[CO_3]_2$, trigonal) used in this study are from the “Grube Lengenbach”, Binntal, Switzerland (Fig. 3.7). The “Grube Lengenbach” is one of the most famous and best investigated locations for minerals. The dolomite used in this study is transparent to greyish and breaks into rhombic fragments. For irradiation experiments, small pieces were broken off the bigger pieces. The mineral collection of the Institute for Geoscience in Heidelberg is very old and the “Grube Lengenbach” was one of the first “must-go” mineral locations within easy reach of Heidelberg, so it is a very likely assumption that the first mineralogists brought some samples from Switzerland to Heidelberg for closer investigations (Fig. 3.8).

3.2.4 Zircon

For the experiments with a natural uranium source, zircon crystals from a titanium mine in Paraíba, Brazil were used.

3.2.5 Uranium doped glass

For the experiments with uranium sources in the fission fragments energy range, CN-5 glass was used as the uranium source. The CN-5 glasses used had a uranium content of 12.17 (± 0.62) ppm (Bellemans et al., 1995). These glasses were produced by J. Schreurs at the Corning Inc. (Corning, New York). CN-5 glasses are the standard material used in fission-track laboratories to check the amount of neutrons applied to samples during irradiation, by counting the emerging fission products on overlaying mica.

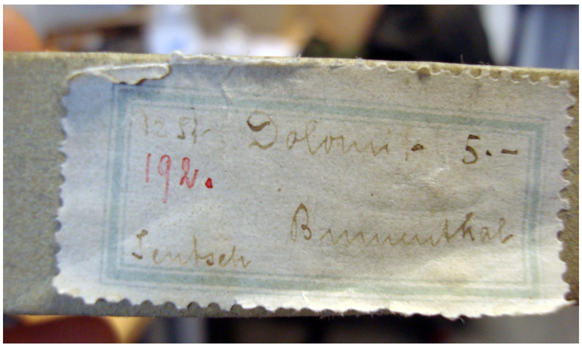

12 St. Dolomit 5.-
192.
Lentsch Binnenthal

Fig. 3.7: Original label of the box from the mineral collection of the Institute of Geoscience, University of Heidelberg, containing the dolomite crystals used in this study

Fig. 3.8: Dolomite crystal

Fig. 3.9: Aerial view of the GSI Helmholtzzentrum für Schwerionenforschung

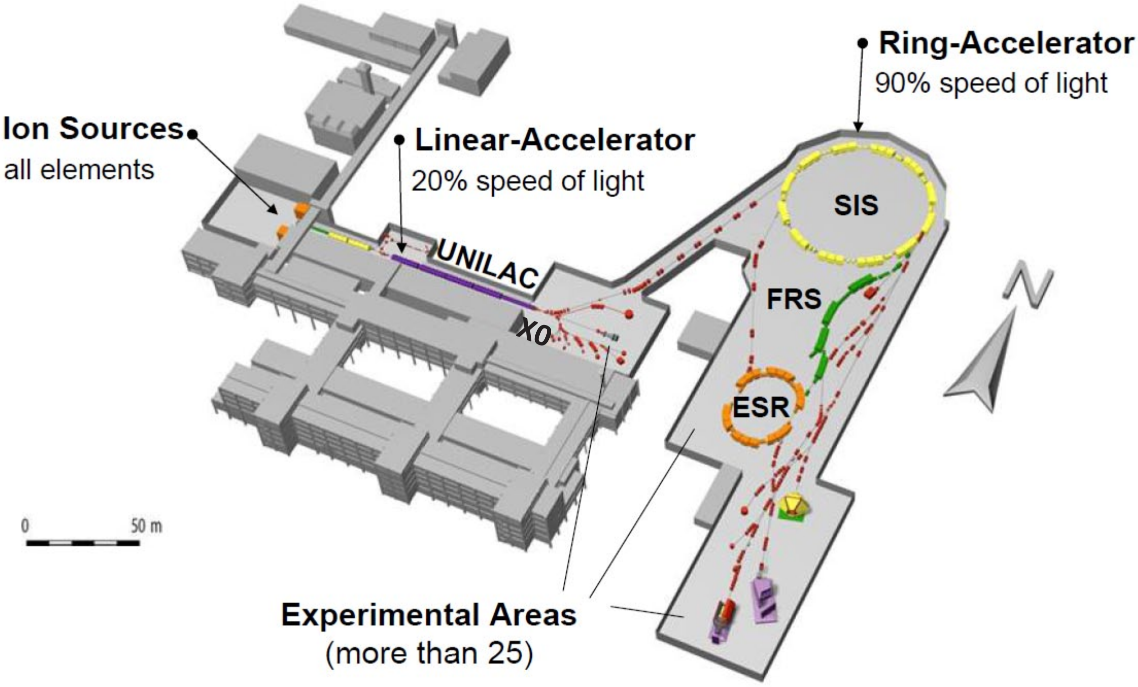

Fig. 3.10: Sketch of the accelerator facility at GSI, Darmstadt.

3.3 IRRADIATION WITH SWIFT HEAVY IONS

3.3.1 Acceleration facility at the GSI Helmholtzzentrum für Schwerionenforschung

The GSI Helmholtzzentrum für Schwerionenforschung in Darmstadt, Germany was founded in 1969 as the Gesellschaft für Schwerionenforschung (Fig. 3.9). As a national laboratory (Helmholtz Association) it has a yearly budget of approximately 108 million Euro, about 1100 employees, of which 500 are permanent, and about 1000 external users per year. GSI operates 3 accelerator facilities:

- The UNILAC linear accelerator which accelerates all elements from proton up to uranium and specific energy up to 11.4 MeV per nucleon (MeV/u) corresponding to about 15% of the speed of light.
- The SIS18, a synchrotron injected by the UNILAC, which accelerates uranium ions up to an

energy of 1000 MeV/u, corresponding to 90 % of the speed of light.

- The Experimental Storage Ring ESR which is able to store ions accelerated by the SIS18 for up to a couple of hours.

More than 25 experimental areas are distributed between the three accelerators. The focus of the research at GSI is on atomic physics, plasma physics, biophysics, and materials research. Big successes in the past have been the synthesis and analysis of the superheavy elements bohrium, hassium, meitnerium, darmstadtium, roentgenium and copernicium. As well as these, a highly effective method for the treatment of brain tumors has been developed at GSI.

The normal course of the beam starts at the ion source (Fig. 3.10). In this facility, all ions from hydrogen to uranium can be generated. After generation, the ions are accelerated a first time in the UNILAC (Fig. 3.10) to an energy of max. 11.4 MeV/u. After this first acceleration the ions reach the experimental hall, where they are distributed to the experimental sites X0- X8 or the M-Branch, depending on the requirements. Some of the ion pulses are injected into the SIS18 synchrotron. There, this pre-accelerated ions feed the SIS18 synchrotron where the ions are further accelerated up to an energy of 1000 MeV/u. These high energetic ions are now extracted from the SIS18, going either to the experimental storage ring ESR, to the fragment separator FSR or to one of the experimental caves in the target hall.

All experiments in this study were performed in X0 in the experimental hall. Beamline X0 provides a flexible system for efficient irradiation of samples for internal and external users. For this, X0 is equipped with an automated sample exchange system where magazines containing 20 sample holders each (see Chapter 3.4) can be irradiated automatically.

3.3.2 Irradiation parameters of samples used in this study

The samples used in this thesis were irradiated with 11.1 MeV/u ^{238}U or ^{197}Au ions at the X0 beamline of the UNILAC, applying fluences between 1×10^{6} and 1×10^{8} ions/cm^{2}. All irradiations (except indicated explicitly) were perpendicular to the surface of the crystals. An exact calibration of the fluence takes a lot of time, so in most cases it is relatively inaccurate and the fluence applied can have an error of factor 2 off the desired value.

All calcite samples were irradiated and therefore etched on the $10\bar{1}1$ plain.

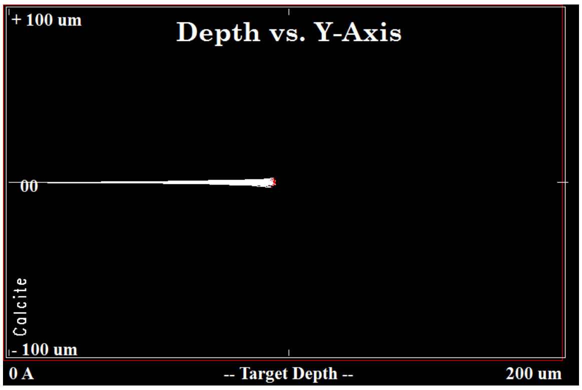

Fig. 3.11: SRIM simulation of 100 Au ions in Calcite

3.3.3 SRIM

To calculate the energy loss of the ions while entering the crystals and the penetration depth of swift heavy ions during irradiation, the simulation software “SRIM” (Ziegler et al., 2010) is used. After entering the irradiation parameters, ion energy, and the properties of the target material in SRIM, the software delivers values for energy loss, projected range, longitudinal straggling and lateral straggling (Tab. 3-3). Experiments show that - after cross-checking the values of SRIM with optical and electron microscopy- the calculated projected range of SRIM tends to be approximately 10 % higher than in reality. Nevertheless, SRIM is

Tab. 3-3: Calculation of the penetration parameters of a calcite crystal irradiated with Au ions with an energy of 11.1 MeV/u. Calculation made with SRIM.

```
Ion              dE/dx                 dE/dx                     Projected
Energy [GeV]     Elec.[keV/µm]         Nuclear [keV/µm]          Range [µm]
----------       ----------            ----------                ----------
2,19             2,442E+04             2,267E+01                 94,39
```

Fig. 3.12: Calcite crystal from the Heidelberg Mineral Collection. 12991 is the registration number of this particular type of calcite from Eskifjörður, Iceland.

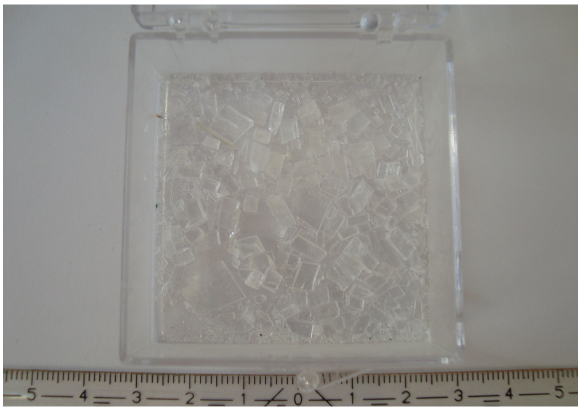

Fig. 3.13: Small pieces of a calcite crystal

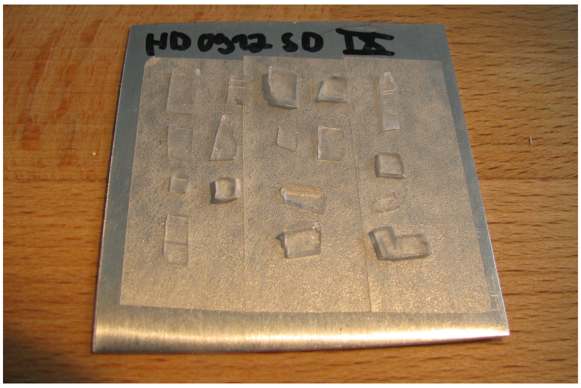

Fig. 3.14: A 5 x 5 cm aluminium plate with attached calcite crystals

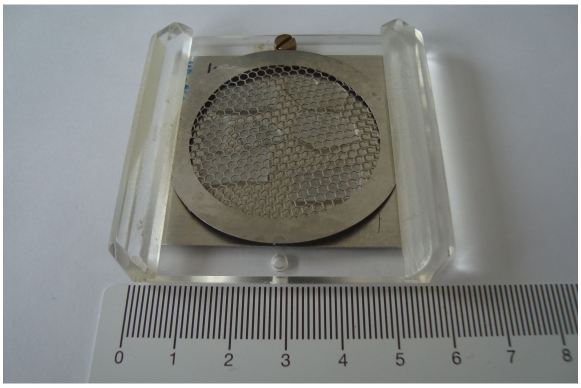

Fig. 3.15: Sample holder with attached hexagonal grid.

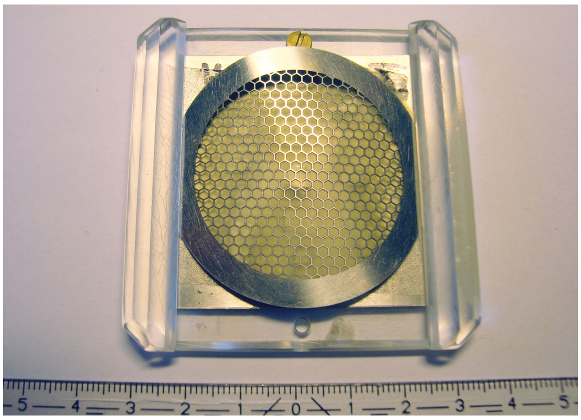

Fig. 3.16: Sample holder with attached hexagonal grid and PC-Foil. This batch is now ready to be irradiated.

an irreplaceable tool for estimating the distance ions travel in matter.

Another function of SRIM (TRIM) simulates visually the path of the ions in matter. An example (Fig. 3.11) shows the path of 100 Au-ions injected at 11.1 MeV/u at the same spot in calcite. The simulation shows the variations of the trajectories.

3.4 Preparation of Samples for Irradiation with Swift Heavy Ions

The samples from the mineral collection of the Institute of Geoscience Heidelberg used in this thesis were originally quite large idiomorph single crystals (Fig. 3.12). These crystals were cleaved by treating them with a screwdriver or other tools to produce smaller specimens for better handling. Due to the almost perfect cleaving properties of calcite in three directions (see Chapter 3.1.2), these smaller pieces are basically smaller versions of the large piece, with the same geometrical relations. The small pieces are about 5 - 10 mm in length, 2 - 4 mm in width and about 1 mm thick. Besides handling better, the size of these small pieces is sufficient for the irradiation experiments at GSI and the available sample volume is used in a very efficient way (Fig. 3.13).

For irradiation with swift heavy ions, the samples were mounted on a 5 x 5 cm aluminium plate to be installed in special sample holders provided by GSI, which are part of the sample exchange system of the X0 - beamline. The small crystals are glued to the plate with double-sided adhesive tape which has enough strength to hold the crystals in position during irradiation. All prepared sample plates were documented twice: with a photograph (Fig. 3.14) to document the condition of the samples, and a sketch of the sample holder, noting the purpose for which a sample taken from the holder had been used. All sample holders and all samples have a unique number to identify the single crystals before and after the irradiation, and after further investigations with associated treatments like etching or annealing of the crystals. During irradiation, the surfaces of calcite crystals were covered with a hexagonal mask with 90 % transmission to create irradiated and non-irradiated sites next to each other (Fig. 3.15). This is necessary because the calcite crystals used have a natural origin and therefore have natural defects in the crystal lattice. The hexagonal pattern helps to clearly identify the ion tracks induced by swift heavy ions. Additionally all samples were covered with a 30 µm polycarbonate foil (PC) (Fig. 3.16). Due to the difficulty of precise fluence calibration, it is important to have a second medium besides the crystals themselves, to determine the real fluence applied to the samples. This foil is very sensitive to irradiation with swift heavy ions, and is able to display every ion applied when etched with NaOH.

3.5 PREPARATION OF THE ETCHING SOLUTIONS

The etching solvents were produced and stored at 21°C (± 0.5°C) under laboratory conditions. For all solutions, purified water and chemicals from the companies *Sigma-Aldrich*, *AppliChem* and *Roth* were used.

3.6 ETCHING PROCESS

The etching experiments were performed under laboratory conditions in an extractor hood. The temperature of the laboratory is kept at a constantly controlled 21 °C by an air conditioning system. The etching procedure includes four beaker glasses: one with the etchant, two with purified water and the fourth containing ethanol (Fig. 3.17). The specimen were etched for defined time periods and then cleaned: firstly in purified water and then in ethanol for some seconds. The single crystals are immersed with tweezers into the etching agent. The etching solution was replaced by a fresh solution after every etching step. Due to rather short etching times of 20 s max, no special tools or mounts had to be developed. Results showed that it is sufficient to introduce the specimen with tweezers into the etching agent. During the etching process, the etching solvent is stirred with a magnetic stir bar. Etching times are highly dependent on the etching solvent. If other temperatures than the 21 °C room temperature were needed for the experiments, a ***Lauda*** E 100 water bath was used to cool down or heat the etchant. To provide an optimal and stable temperature, the bottles containing the etching solutions were introduced into the water bath the evening prior to the experiment.

Fig. 3.17: Setup for the etching experiments. From left to right: stopwatch, etching solution, 2x pur. water, ethanol.

3.7 ANALYTICAL METHODS AVAILABLE IN HEIDELBERG

Before and after the etching process, the samples were carefully analyzed to describe changes in surface morphology, optical & geometrical characteristics and material properties.

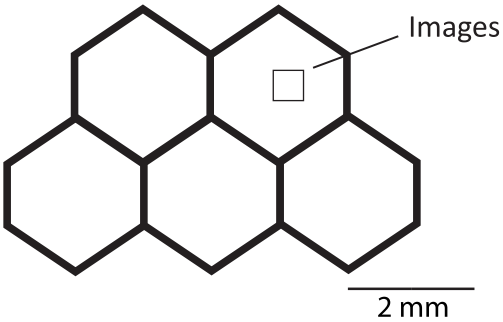

Fig. 3.18: Sketch of the hexagonal mask overlaying the samples. In the majority of cases the images in this study are taken from the middle of the pattern

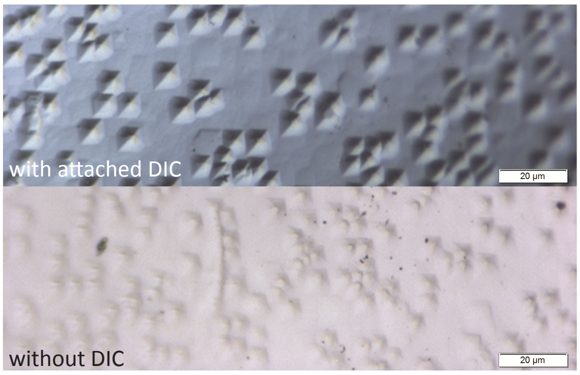

Fig. 3.19: Image with and without DIC. The etch pits are barely visible without DIC

3.7.1 Optical microscopy

For all optical analysis and statistical examination, a reflected and transmitted light Olympus BX-50 microscope with attached Nomarski Differential Interference Contrast (DIC, NOMARSKI, 1955) and high resolution camera combined with Stream™ image analyzing software were used. The microscope is equipped with 5x, 20x, 50x and 100x objectives and a variable lens barrel with a range of 1x to 2x magnification. Most of the images were taken at high magnification inside the hexagonal pattern, so in most images the borders between the single hexagons are not visible (Fig. 3.18). All images were taken with attached DIC because due to their relatively shallow depth, the etch pits are barely visible in reflected light without DIC (Fig. 3.19). The DIC device is also responsible for the blueish colors of the images observed in most cases. All crystals are actually colorless. The microscope's length scales were calibrated with a ***Geller*** magnification standard prior to the measurements.

3.7.2 Raman spectroscopy

To determine potential changes in the material's properties, all samples were investigated using Raman spectroscopy before and after the irradiation and etching process. The Raman system

Fig. 3.20: Raman spectrometer of the Institute of Geoscience, University Heidelberg

available in Heidelberg is a ***Horiba Jobin Yvon*** iHR 320 spectrometer with a Pelletier cooled camera, and a laser system consisting of a ***Laser Quantum*** Ventus 532 nm Laser with 90 mW power and the laser control unit ***Laser Quantum*** MPC 6000 (Fig. 3.20). The system is controlled with the ***Horiba*** LabSpec 5 software. This system is extended with a ***Horiba*** Superhead + ***Euromex*** EK1 cold light source, mounted on a microscope with 5x, 10x, 20x and 50x objectives and a manual XYZ stage. The ***Horiba*** Superhead enhances the system to a confocal Raman system, for very precise measurements of only irradiated layers of the samples.

3.7.3 Furnace

The laboratory furnace used for the annealing experiments of Chapter 9 is a ***Heraeus Instruments*** M 110 muffle furnace with an temperature uncertainty of ± 2 °C.

3.8 IRRADIATION WITH THERMAL NEUTRONS

For the experiments with fission fragments in Chapter 8, all samples were irradiated with thermal neutrons at the Forschungsreaktor München (Research Reactor Munich) II, the FRM II. There, the prepared sample batches were loaded into small capsules, which were then introduced into the reactor via a sample lock for the irradiation process.

3.9 STATISTICS

3.9.1 Length and width

To determine the length and width of the etch pits, images of the samples taken with ***Stream*** image analyzing software on the calibrated ***Olympus*** BX-50 microscope were evaluated. In most cases, the 50 x objective was used. At least 50 values were taken for each length and width, if necessary on several images. Only etch pits which stood alone, not overlapping with other etch pits, and therefore showed their full dimensions, were measured (Fig. 3.23). In each case the arithmetic mean of these values is used as a single data point in diagrams. The error of the measurements is calculated by standard deviation for all measurements (Fig. 3.21).

$$SD = \sqrt{\frac{\sum_{i=1}^{n}(x_i - \bar{X})^2}{N}}$$

Fig. 3.21: Standard deviation formula

3.9.2 Areal density

To determine the areal density of the etched ion tracks on the calcite crystal, the amount of etch pits on several images at the same magnification (50 x) were counted and an arithmetic mean of all of this values was calculated (Fig. 3.24).

3.10 BASICS OF TRACK ETCHING

The etching process to etch ion tracks in calcite is dictated in the simplest way by two constant etching processes which run simultaneously: The etching rate along the track (v_t) at a linear rate, and the etching rate of the undamaged bulk material (v_b) at a lesser rate (FLEISCHER & PRICE, 1963 a, b). Both etching velocities are depending on the etching conditions. Additionally , v_t is also affected by the energy loss of the induced ion; it increases linearly with increasing dE/dx (SCHIEDT, 2007). Figure 3.22 shows the etching process schematically. The opening angle ϕ and the diameter D of the etched ion track are related to the ratio of v_b and v_t.

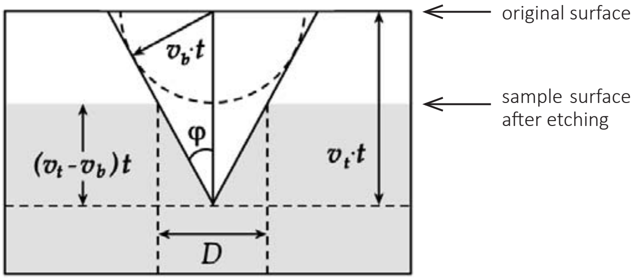

Fig. 3.22: Schematics of track etching. After SCHIEDT, 2007

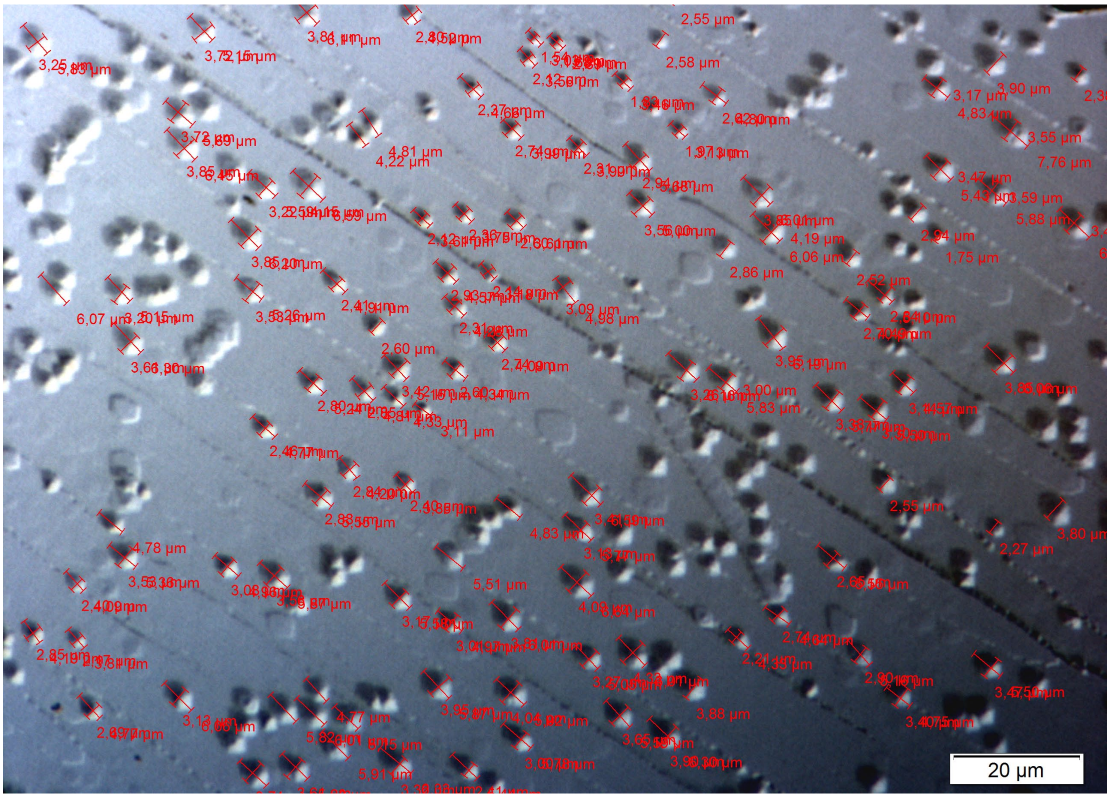

Fig. 3.23: Measurement of the length and width of the etch pits (red values). Only etch pits which are standing alone have been measured

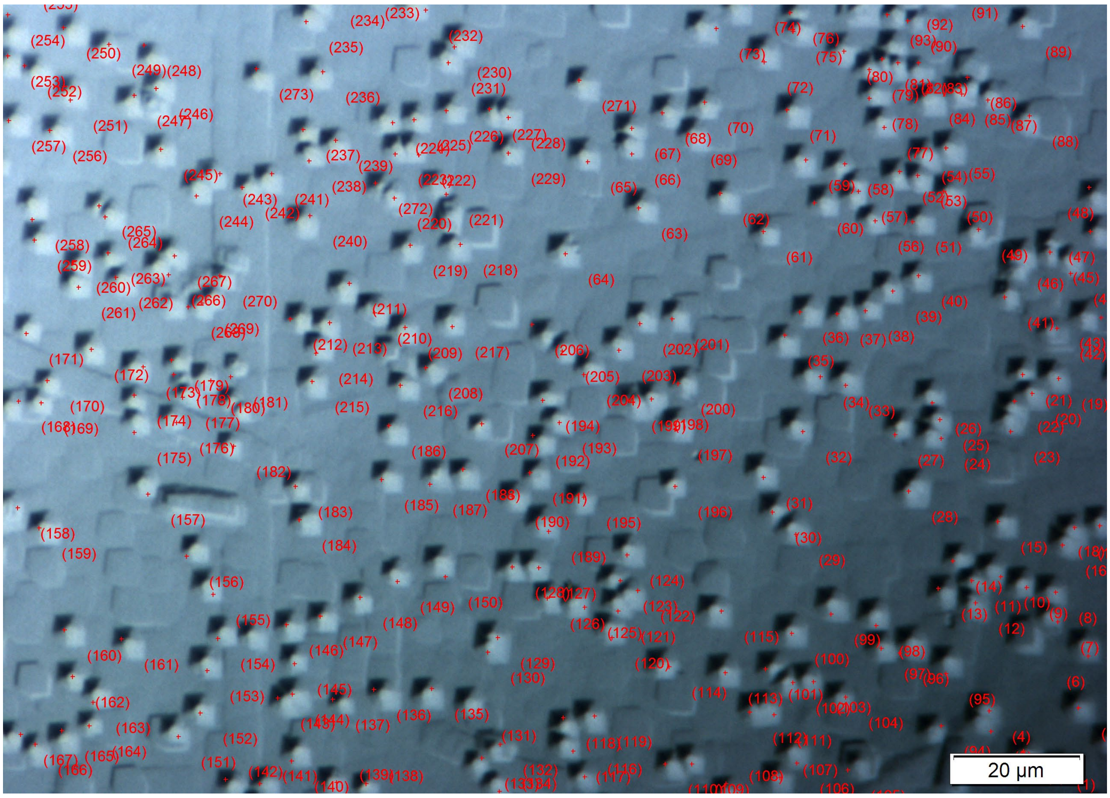

Fig. 3.24: Determination of the areal density. Each etch pit is counted. Every cross and number (marked in red) represents one etch pit.

4

PREPARATION OF CARBONATE ROCKS FOR IRRADIATION WITH SWIFT HEAVY IONS

CONTENTS

4.1 INTRODUCTION

For irradiation and etching experiments with calcite, it is necessary to have a perfectly flat surface of the mineral or else the scratches and the roughness of the surface obscure the etched ion tracks and nothing can be seen on the surface. One possibility to get almost perfect surfaces is to use the cleavage abilities of calcite to produce freshly cleaved plains. Unfortunately, this method works for perfect idiomorph calcite crystals only and is not suitable for all other minor perfect crystals or for calcite crystals embedded in a carbonate rock matrix. Therefore, for most of the samples collected from nature, another preparation method had to be developed so that these samples were also usable for irradiation and etching experiments.

Due to its trigonal crystal structure and its perfect cleavage properties calcite is a very soft mineral with a Mohs-hardness of 3. Thus it is too soft for normal grinding and polishing techniques and the surface is too easily damaged, so that even 1 µm diamond paste is not smooth enough to get a perfect surface. This chapter gives detailed instructions on how to grind and polish calcite crystals properly.

4.2 PREPARATION

4.2.1 First, unsuccessful attempts

In order to establish a preparation procedure for calcite crystals for ion irradiation, calcite crystals from Eskifjörður, Iceland (12991 collection Heidelberg) were sawed into slices to simulate the rough surface of non-idiomorphic samples (Fig. 4.1). These slices were ground with 2400 sandpaper and polished with 1 µm diamond paste (DP Paste). The quality control of the sample with the naked eye showed a very smooth surface and even under the microscope the quality seemed satisfactory. After irradiation with swift heavy ions (1×10^7 ions/cm^2 Au, 11.1 MeV/u) the samples were etched with EDTA + 5 % acetic acid at 21 °C for 20 s. This etching process revealed a very rough surface with numerous scratches and bumps. Additionally, no etch pits of etched ion tracks were visible. After a very careful investigation of the samples some sparse etch pits were found on the border area of the sample. In this particular area the crystal was not sawed but had broken along its cleavage plane at the very end of the sawing procedure, and therefore this small area had all properties of a cleaved crystal (Fig. 4.2). This revealed two points:

Fig. 4.1: The surface of a sawed calcite crystal.

- The irradiation process was correct
- The surface of the calcite crystal was not smooth enough to display the etch pits. The etching solvent widens and therefore highlights all the micro-scratches and other leftovers from the polishing. As a result the widened structures on the surface obscure the etch pits so they are not visible in polished areas.

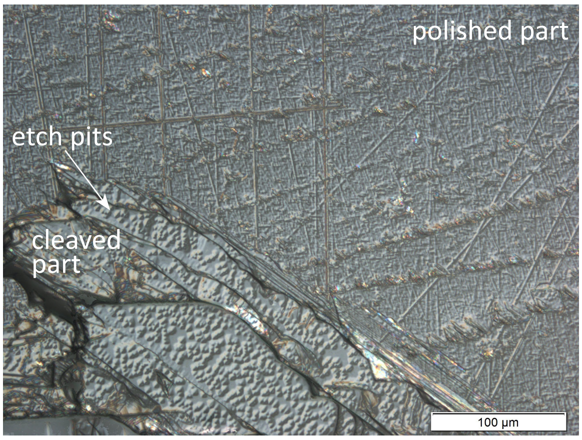

Fig. 4.2: The surface of a calcite crystal from the first preparation series. The difference between polished parts and cleaved parts on the outer areas of the crystal is obvious: On the polished part, the morphology has been etched strong enough to obscure the etch pits of induced ion tracks. The etch pits are visible on the cleaved areas only. 1×10^7 ions/cm^2 ^{197}Au, 11.1 MeV/u

The conclusion to be drawn from these results is that the surface of the calcite crystals is not smooth enough after polishing with 1 µm diamond paste, and that a new embedding and polishing technique needed to be developed, which is described in this chapter.

4.2.2 New preparation method

4.2.2.1 Embedding

To be able to work with the calcite samples satisfactorily, they were embedded in epoxy resin. The easiest way to embed the calcite is to put a stripe of double sided duct tape into a disposable plastic dish or a folded paper and glue the samples onto that duct tape. This procedure prevents the samples from floating in the liquid epoxy resin. After mounting the samples, put the epoxy forms over them and fill them with epoxy resin (Fig. 4.3). It is very important to mount the forms in a disposable plastic dish or box, because often the arrangement of tape and epoxy form is not perfectly leak-proof, so the dish prevents the epoxy from flooding all over the laboratory. It is no problem if some resin leaks as long as the samples in the form are still fully covered with resin. Then, the resin should be hardened according to the product manual. After hardening, the epoxy resin with the samples can be pressed out of the form. They are now ready for grinding.

Fig. 4.3: Dish with double sided duct tape. On the left are apatite crystals (for better contrast). To embed these crystals, the form on the right is glued to the duct tape over the crystals and filled with epoxy resin.

All grinding times correspond to a grinding pressure of 5 N.

Note: If the samples are to be irradiated with thermal neutrons, a few zircon grains should also be added to every sample, next to the calcite, because they are very helpful for the mount/mica alignment after irradiation. The resulting sample mounts have a diameter of about 21 mm, which is the standard sample size for neutron irradiation at the FRM II, Munich.

IMPORTANT: All polishing and grinding times mentioned are experimental data relating to the equipment used in the Heidelberg preparation lab, and are therefore only recommendations and not strict instructions!

4.2.2.2 Grinding

The first step after unmounting the samples is to establish a basic surface for all following proceedings. Therefore the sample must be ground with 1200 SiC-Paper until the surfaces of the embedded crystals are no longer covered with epoxy resin. The average time for this is about 5 min. Make sure the surface of the sample is planar. This makes the next steps a lot easier.

After finishing work on the surfaces it is important to round off the edge of the sample to minimize abrasion by the sample of the papers and cloths, and conserve the latter.

The next step is to fine grind the samples with 2400 SiC-Paper for about 6 min. The samples are then ready for polishing.

4.2.2.3 Polishing

Diamond polishing

The first step in polishing the ground samples is to use 1 µm DP-Paste with a MD-DAC polishing cloth. For this purpose the polishing cloth must be prepared by distributing DP-Lubricant Blue (***Struers***) and some 1 µm DP-Paste on the cloth. Then, the sample must be polished for about 8 min. After polishing, the sample should be cleaned with purified water and then dried with compressed air to avoid unnecessary mechanical contact with the polished surface. Then, a control of the surface under an optical microscope shows whether the sample is ready for the next steps, or if further polishing is necessary. If the polishing result is satisfactory, proceed to the next step, otherwise repeat this step.

OP-S polishing

Active Oxide Polishing is a polishing technique provided by ***Struers*** to polish materials which are very soft and ductile. The used OP-S polishing suspension is optimized for very ductile materials Before starting with OP-S polishing the OP-Chem polishing cloth must be prepared. The cloth must be very wet before polishing. The easiest way to achieve the correct amount of wetness is to mount the cloth and operate the plate with added water supply for about 10 min.

The second very important issue with OP-Chem cloth and OP-S Solution is to clean the cloth before and after the use of OP-S with a brush on the rotating cloth with the water running. OP-S dries out very fast and leaves a white powder behind. If the cloth is not cleaned carefully after use the residues from former usage will still be in the cloth and will damage your sample.

When the cloth is ready, put some OP-S on the cloth and start polishing. More OP-S should be added every 5 – 8 min. Polishing should be performed in stages of 15 min. After each stage, the sample should be cleaned with purified water and compressed air to check the surface and ascertain whether further polishing is necessary. The whole polishing procedure takes about 30 – 60 min depending on the samples being polished.

This last step must be performed very carefully; the resulting quality of the sample depends to a great extent on the chemical polishing. Even slight coarseness has a significant influence on the ability of the sample to display ion tracks on the surface. Figure 4.4 shows the surface of a calcite crystal prepared using the described method. The surface looks smooth, even when it is monitored with attached DIC. For comparison, Figure 4.5 shows an example of the surface of a cleaved crystal, which were used in most of the experiments. These surfaces vary in quality, but are usable in most cases.

4.2.2.4 Finishing

After the surface is in perfect condition, the sample itself has to be prepared for further use, for example in the neutron reactor or an acceleration facility like a swift heavy ion accelerator. For this purpose the thickness of the sample has to be reduced to about 500 - 800 µm to get a reasonable amount of samples in an irradiation batch of the neutron reactor which has a cylindrical form, where the single samples are stacked. In the case of calcite minerals, the samples have to be ground down because due to the thickness of the calcite minerals the use of a turning machine would destroy the sample if the tip came in con-

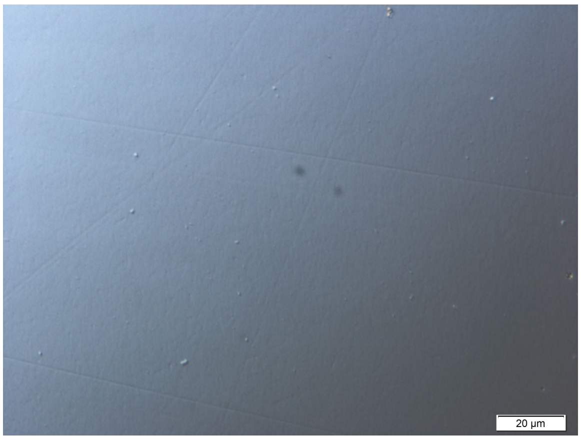

Fig. 4.4: The surface of a calcite crystal using the preparation method described

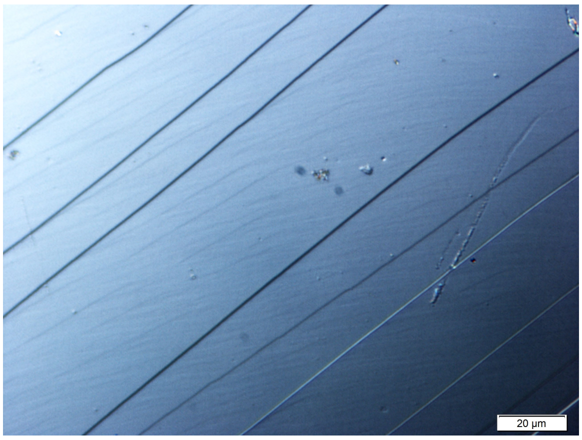

Fig. 4.5: The surface of a cleaved calcite crystal

tact with the crystal. To reduce sample thickness, the Special Sample Holder and 180 SiC-Paper should be used. These two tools and the grinding machine can be used down to a sample thickness of about 500 - 800 µm. To maximize light transfer through the sample it is then recommended first to grind the back of the sample with 2400 SiC-Paper and secondly to polish the back with 1 µm DP-Paste. Then the samples are ready for experiments.

4.2.2.5 Special sample holder

To reduce the thickness a special sample holder has been designed (Fig. 4.6 & Fig. 4.7). Its function is to secure the samples during the size reducing process without damaging the finalized surface of the sample. The holder can also be used in the polishing machine. It only touches the very outer areas of the sample and protects almost the whole surface of the already polished sample.

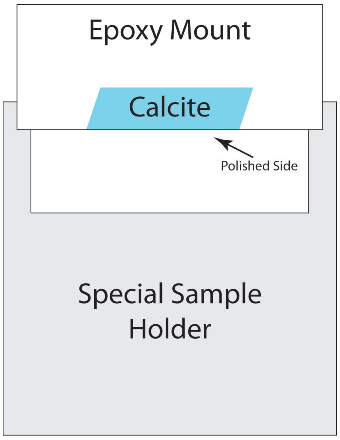

Fig. 4.6: Sketch of the special sample holder used for finishing the sample

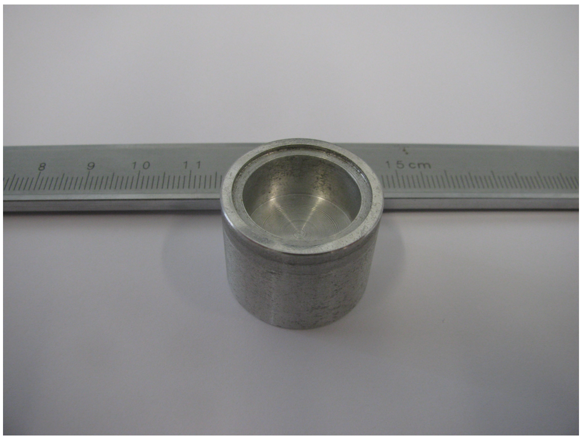

Fig. 4.7: The special sample holder

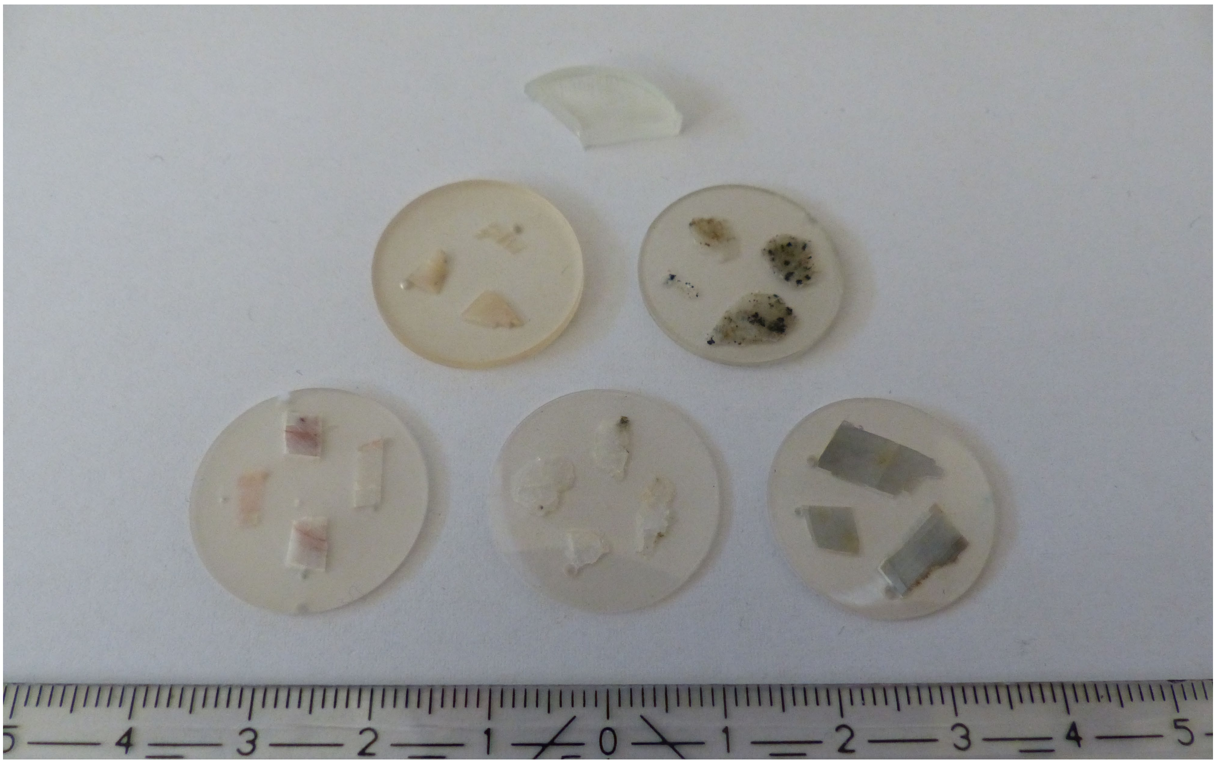

Fig. 4.8: Samples prepared using the preparation method described in this study.

4.2.2.6 Materials needed

Materials needed (All materials by ***Struers***, except special sample holder)

- EpoFix Cold Mounting Set with embedding forms
- Polishing and grinding machine, for example LaboPol with LaboForce Sample Holder
- SiC Paper for wet grinding with 180, 1200, and 2400 grain size
- MD-DAC polishing cloth
- DP-Paste diamond paste with 3 and 1 µm grain size
- DP-Lubricant Blue cooling and lubricating liquid
- OP-Chem polishing clothes
- OP-S Oxide Polishing Suspension
- Special Sample Holder for final shortening of the samples for better handling and compatibility

4.2.2.7 Irradiation

After completing the preparation process, the samples are ready for irradiation. Due to their thinness, the samples are suitable for many irradiation facilities, for example different beamlines at the GSI Darmstadt for irradiation with swift heavy ions, or the sample positioning system at the FRM II (Research Reactor Munich) for irradiation with thermal neutrons.

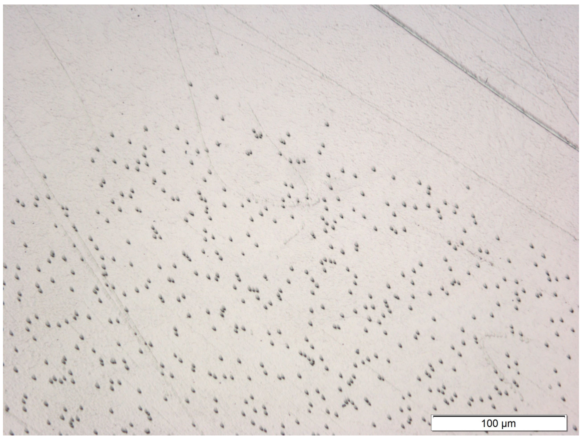

Fig. 4.9: Etch pits of etched ion tracks on a calcite crystal prepared using the method described. Irradiation parameters: (11.1 MeV/u, 1×10^6 ions/cm^2, Au-ions)

4.3 PREPARATION RESULTS

4.3.1 Samples

The results of the preparation procedure described are chips with a diameter of 21 mm and a height of 500 -800 µm depending on the construction of the special sample holder and the anticipated application of the samples. This method is not only suitable for soft calcite crystals but also for many other rocks, for example various kinds of carbonatites (Fig. 4.8).

4.3.2 Etching prepared samples

The main question after finishing the first samples using the method described above was whether the surface of the prepared samples was now smooth enough to see etched ion tracks. So, after irradiation with swift heavy ions (11.1 MeV/u, 1×10^6 Au-ions/cm^2) first etching attempts (0.91 % HNO_3, 1 s) were performed, and these experiments showed that the method works and the samples are able to display etch pits of etched ion tracks on the surface (Fig. 4.9).

Although the surface itself also gets etched a bit, the quality is good enough for the etched ion tracks not to be obscured by the generated morphology. The etch pits themselves do not differ from etch pits on cleaved calcite crystals. Details are included in the next chapter.

4.3.3 Comparison of samples prepared using the described method and samples from a cleaved crystal.

The figures shown in this paragraph are on one hand a crystal cleaved and irradiated with swift heavy ions at GSI, Darmstadt (11.1 MeV/u, 1×10^6 ions/cm^2, Au) (Fig. 4.10), and on the other hand a crystal prepared using the method described above and irradiated with uranium fission products, generated by uranium glass in the FRM II in Munich (Fig. 4.11). Both crystals have been etched with 0.091 % HNO_3 at 15 °C for 2 s.

In a comparison, the properties of the etch pits are very similar. The geometrical shape is the same, only the size of the etch pits on the

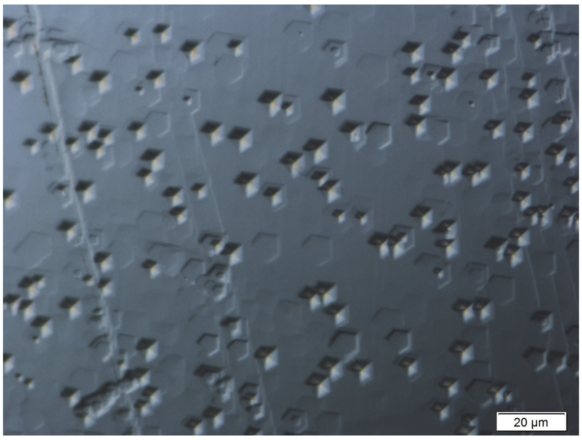

Fig. 4.10: Etch pits of etched ion tracks on a calcite crystal, cleaved and irradiated at the UNILAC with 11.1 MeV/u, 1×10^6 ions/cm^2, Au-ions

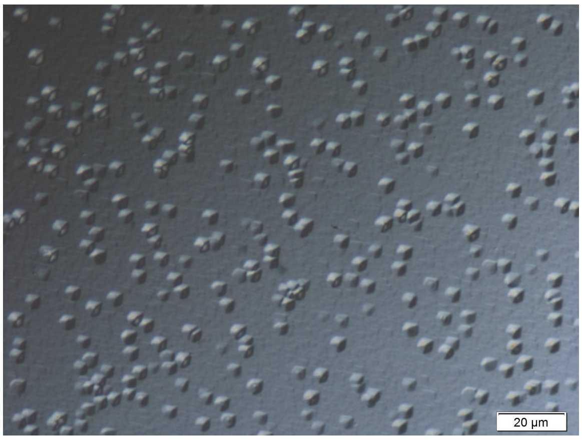

Fig. 4.11: Etch pits of etched ion tracks on a calcite crystal prepared using the method described and irradiated with uranium fission products of a CN-5 uranium glass

prepared sample is slightly smaller, but this can be easily compensated by longer etching times if necessary. This effect could also be induced by the low energy of the fission fragments. Additionally, the lower atomic mass and the resulting lower energy loss of the fission fragments, which also lead to smaller track diameters has to be considered, but the important part is the matching areal density of the fluence induced on both crystals. Differences which can be observed are a slightly rougher surface of the prepared sample in comparison with the cleaved crystal, which shows a perfectly smooth surface even after the etching process.

This comparison shows that calcite crystals prepared using the method described above are even usable to display the effects of irradiation by fission fragments with very low energies and a smaller energy loss.

4.4 DISCUSSION

The results achieved with the combination of the described sample preparation and the etching procedure reveal etch pits. This result proves that the preparation method developed covers all the requirements of the quality of the crystal surface. The comparison of etched samples produced with the preparation method and etched samples of cleaved calcite crystals revealed no major differences. The method can therefore be used for all irradiation experiments with subsequent etching.

5

Visualization of Heavy Ion Tracks by EDTA Etching Techniques

Contents

5.1 INTRODUCTION

After the evaluation of possible etching recipes through literature research (see Chapter 2), first experiments to identify a suitable etching solution were performed. For this, cleaved calcite crystals were irradiated with swift heavy ions with an energy of 11.1 MeV/u ^{197}Au ions at the X0 beamline of the UNILAC, applying fluences between of 1×10^6 and 1×10^8 ions/cm^2, with a penetration depth of about 90 µm (Tab. 5-1). These crystals then were etched with a total of 4 etching agents.

5.1.1 Etching solvents and conditions

5.1.1.1 Hydrochloric acid (HCl)

As a geologist, the first approach to etching calcite crystals had to be the usage of hydrochloric acid because the use of hydrochloric acid is a standard method to identify calcite crystals and rocks in fieldwork. In the field, a 10 % HCl is used but this was thought to be too strong so for this first test a 1 % HCl solution was used. The calcite crystal (1×10^6 Au ions/cm^2, 11.1 MeV/u) was etched for 30 s. The result shows a completely destroyed surface of the crystal (Fig. 5.1). Thus even a 1 % HCl solution is far too strong for the visualization of ion tracks in calcite.

5.1.1.2 Formic acid (CH_2O_2)

SIPPEL & GLOVER (1964) used concentrated formic acid to generate etch pits in Iceland Spar calcites. Formic acid is a very strong etchant which produces deep etch pits and etch mounds on the calcite surface which represent the crystal structure of the calcite. Based on this knowledge, first experiments were made with 10 % CH_2O_2. Even this highly-diluted etching solution produces major changes on the material surface and therefore this solvent is too strong to visualize the ion tracks, because too much of the calcite surface is etched away. However, after 30 seconds of etching the etch pits are shaped in a hexagonal pattern (Fig. 5.2). This shape does not change as the etching process progresses, the etch pits just grow larger with time. They reach a length of about 100 µm and a width of about 40 µm after 60 seconds of etching.

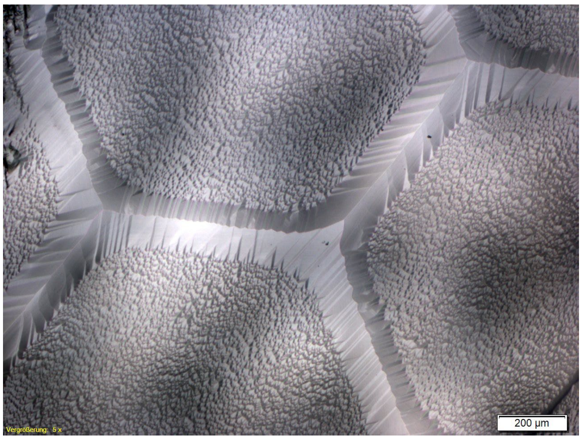

Fig. 5.1: Calcite crystal etched with 1 % HCl for 30 s. Irradiation parameters: 1×10^6 ions/cm^2 ^{197}Au, 11.1 MeV/u

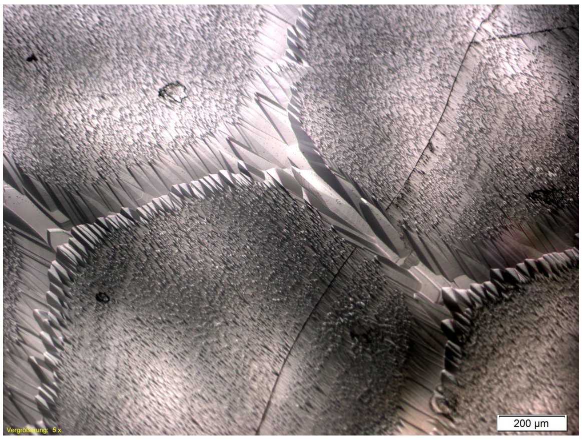

Fig. 5.2: Calcite crystal etched with CH_2O_2 for 30 s. Irradiation parameters: 1×10^6 ions/cm^2 ^{197}Au, 11.1 MeV/u

Tab. 5-1: Calculation of the penetration parameters of a calcite crystal at the irradiation with Au-ions with an energy of 11.1 MeV/u. Calculation made with SRIM.

```
Ion            dE/dx              dE/dx                  Projected
Energy [GeV]   Elec.[keV/µm]      Nuclear [keV/µm]       Range [µm]
----------     ----------         ----------             ----------
2,19           2,442E+04          2,267E+01              94,39
```

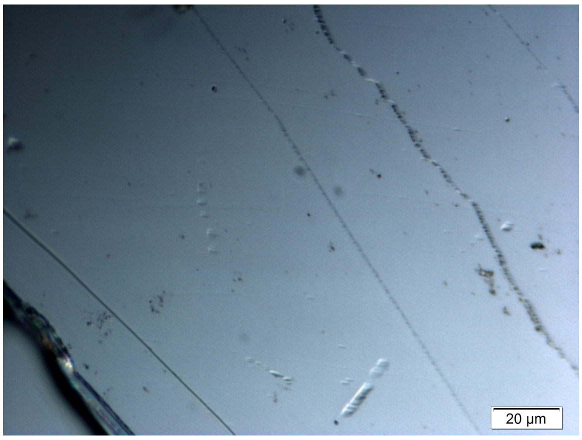

Fig. 5.3: Calcite crystal etched with 12 M NaOH for 20 min. Irradiation parameters: 1×10^6 ions/cm^2 ^{197}Au, 11.1 MeV/u

5.1.1.3 Sodium hydroxide (NaOH)

Two approaches could be found for etching calcite with NaOH: Macdougall & Price (1974) suggest using 2 M NaOH, and Afarideh et al. (1993) used 6 M NaOH at a temperature of 70 °C. Etching of irradiated calcite crystals with 2 M NaOH produced only minor changes on the crystal surface. Even after 20 minutes of etching no etch pits were formed, only a slight change in morphology was visible. Natural cracks and defects were accentuated, but no ion tracks were made visible. Increasing the concentration to 10 M did not show any difference and even increasing the etching agent to a 12 M NaOH solution did not show any improvement (Fig. 5.3). Thus although many different approaches were tried in order to reproduce the etching success of Macdougall & Price (1974) and Afarideh et al. (1993), no satisfying results have as yet been obtained.

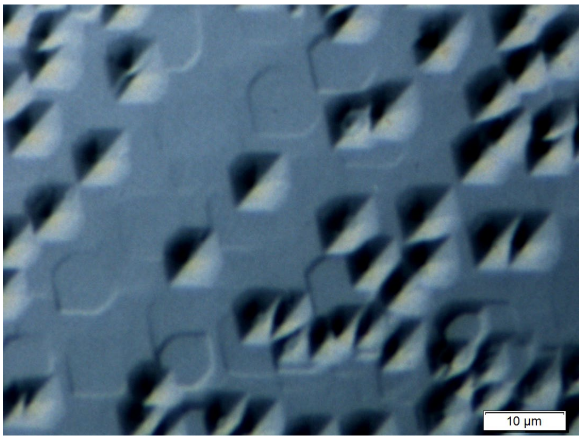

Fig. 5.4: Etch pits in the middle of the picture. Calcite after 20s in EDTA + 5% acetic acid. Designated as Type I

5.1.1.4 EDTA + 5 % Acetic acid ($C_2H_4O_2$)

The next test, etching with a satisfied solution of disodium - ethylenediaminetetraacetic acid (EDTA) + 5 % acetic acid in a ratio of 1:1 showed that this etchant is useful and reliable. The etching procedure is based on Macdougall & Price (1974) who were etching calcites of the Olduvai Gorge, South Africa. The etchant is prepared from a satisfied solution of disodium – ethylenediaminetetraacetic – salt mixed with purified water (pH 5) at 21 (±0.5) °C and 5 % acetic acid made with 100 % acetic acid mixed with purified water, in the ratio of 1:1. The solvent has a pH level of 3.8 (±0.1). After 5 s of etching etch pits can be seen under the microscope and after 20 s the hexagonal pattern on the crystal is visible with the naked eye. The overlapping of etch pits after about 30 s of etching time limits further etch pit size evaluation. In general, the etch pits have a pseudohexagonal shape and are geometrically well defined. The etching solvent will be called “EDTA + X % acetic acid” throughout this doctoral thesis.

5.2 RESULTS FOR CALCITE

5.2.1 Optical description

The etch pits appearing most frequently after etching with EDTA + 5 % acetic acid are defined as Type I. Type I etch pits have a pseudohexagonal shape with a tiny hole in the middle, which is supposed to be the ion track, and they occur on irradiated surfaces (Fig. 5.4 + Fig. 5.5). Width and

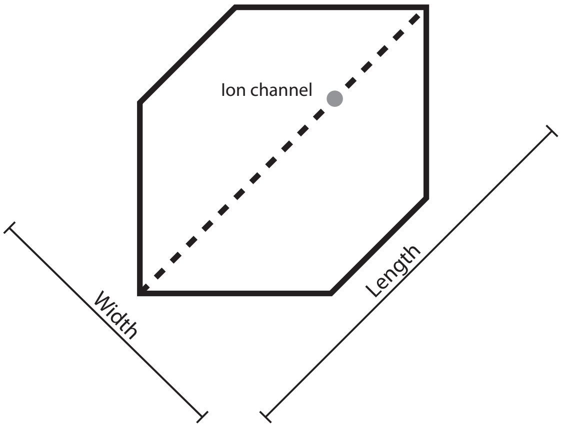

Fig. 5.5: Sketch of an etch pit

length of the etch pits show a linear increase as a function of the etching time. Their areal density matches the ion fluence applied. Therefore Type I etch pits are designated as etch pits of etched ion tracks.

The etch pits themselves are in the best case geometrically well defined. Especially in transmission light the ion track is apparent. Related to the fluence of 1×10^6 ions/cm^2, the best visibility (well developed, no overlap) of the etch tracks is provided after 20 s etching for a fluence of 1×10^6 ions/cm^2 (Fig. 5.8).

The average size of etched ion tracks after 20 s of etching is up to 10 (± 1) µm long and up to 8 (± 1) µm wide. They show a linear growth up to 20 s (Fig. 5.6). The etch pits are presumably less than 1 µm deep. It is not possible to focus just on the bottom of the etch pit or just the crystal surface. Besides the almost perfectly shaped hexagonal etch pits there are also etch pits with differing shapes. These etch pits show no clear geometrical shapes, their margins are ragged. Only some regions of some crystals show this behavior. Possible reasons for this effect may be alterations in the crystal surface, like twinning or scratches, or dirt.

In summary, all quality levels from well to poorly shaped etch pits are present on the etched calcite crystals, but the majority of the etched ion tracks are rather well formed.

5.2.2 Concentration of acetic acid

After this success a series of experiments was started in order to find out whether the concentration of acetic acid influences the etching speed and the shape of the etch pits. For this purpose two series of experiments were performed.

Crystals of Etching-Series I were etched with 0,5, 1, 2, 3, 4 & 5 % of acetic acid, crystals of Etching-Series II were etched with 0, 0.5, 1, 2, 2.5, 3, 3.5, 4 & 5 % of acetic acid. In Series I the six crystals were fragments of one larger crystal, so all crystal properties are the same.

Etching experiments revealed that concentration of acetic acid in the etching solvent plays a minor role. An analysis of the size of the etch pits in the two series shows that crystals etched with 1% acetic acid can have almost the same size of etch pits as crystals etched with 5 % acetic acid for the same time. In addition, two crystals etched with 2 % and two crystals etched with 3 % acetic acid have significantly different results concerning the size of the etch pits. Therefore it is a likely assumption that the quality of the crystal surface (including twinning, crystal defects, inclusions, evenness of the surface etc.) and its cleanliness play a much larger role for the generation of etch pits than the concentration of acetic acid in the etching solvent. This result is discussed in detail in Chapter 5.2.10.

As result, EDTA + 5 % acetic acid in 1:1 proportion was defined as the standard etching solution for etching with EDTA + acetic acid.

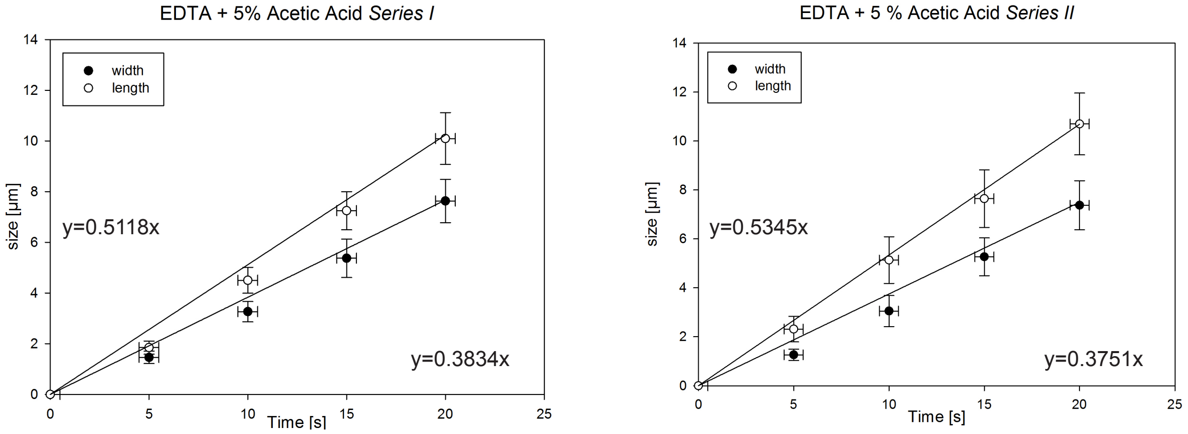

Fig. 5.6: Growth diagram of the crystals etched with EDTA + 5 % of acetic acid. Parameters: 1×10^6 ions/cm^2 ^{197}Au, 11.1 MeV/u

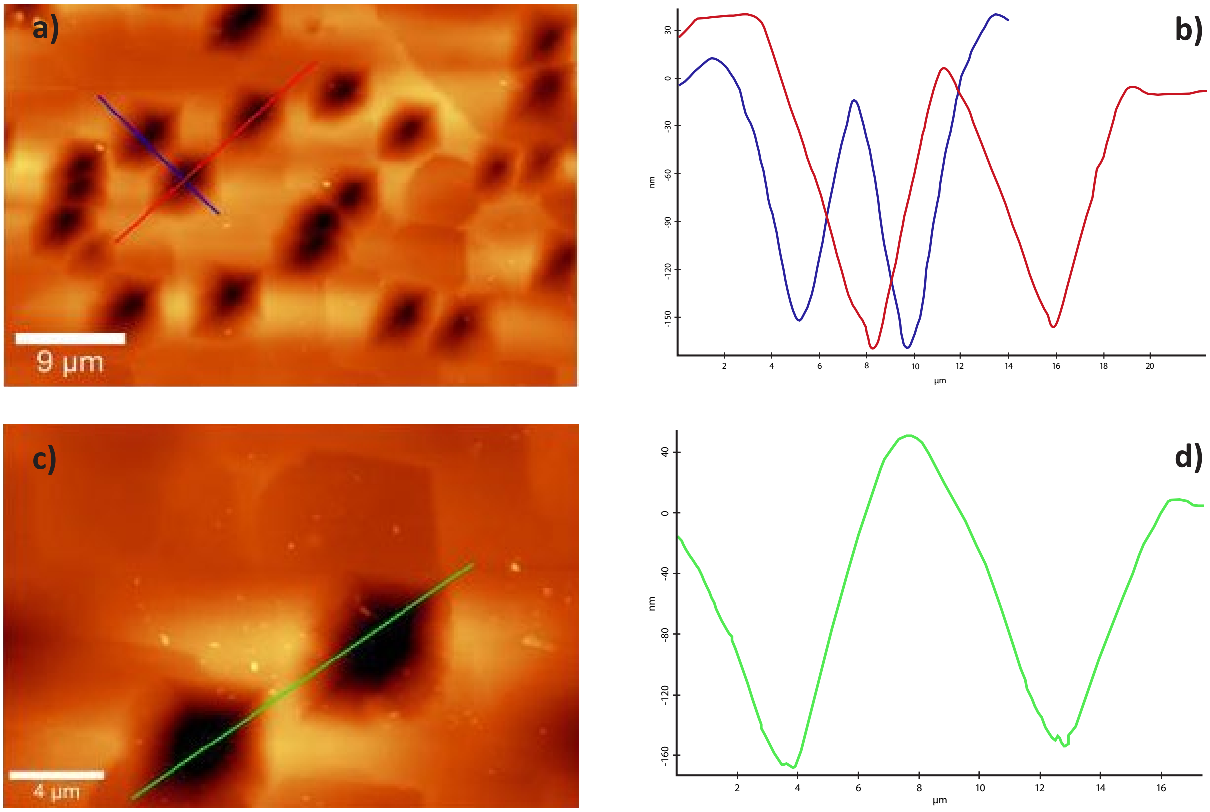

Fig. 5.7: AFM Images of an irradiated crystal. The shape determined by optical microscopy could be confirmed by AFM images. Additionally a first idea of the depth of the etch pits could be determined. Irradiation parameters: 1×10^{6} ions/cm^{2} ^{197}Au, 11.1 MeV/u

5.2.3 AFM images

During a visit to the ***WITec*** company in Ulm, Germany we had the chance to investigate calcite samples with a state-of-the-art AFM device (Fig. 5.7). These images clearly confirm the observations made with the optical microscope with attached DIC: the etch pits have a pseudo-hexagonal shape with relatively sharp edges. Additionally, the AFM technique makes it possible to measure the depth of the etch pits to some extent. The measurements show a depth of approximately 200 nm for an etch pit (Fig. 5.7 b + d). Due to the technical limitations of the AFM device used, the 200 nm are the maximum depth the device is capable of showing. This means that the etch pits are at least 200 nm deep, but most likely have a depth of about 200- 300 nm. The upper boundary is given by the lack of focus differences between the edge and the bottom of the etch pit in optical microscopy. Nevertheless, this satisfactorily explains the difficulties in seeing the etch pits without DIC: they are just too shallow and the contrast to the bulk calcite surface is not high enough. The AFM diagrams also show a very linear slope of the etch pits, showing that the etching process must have taken place in a very constant way. The length and width of the etch pits could also be confirmed.

5.2.4 Statistics of etch pit length and width

In order to study the growth development of the etched ion tracks through time, size measurements were performed. After every stage of etching (5, 10, 15, 20 (±0.25) s) 100 values for width and length has been determined to achieve a statistically significant result. All results have been plotted in size over time diagrams (Fig. 5.6). Figure 5.8 a-e show a typical etching progress on a calcite crystal.

5.2.5 Areal density

For fluences of 1×10^{6} ions/cm^{2} the areal density of the etch pits on the crystals corresponds to the ion fluence the crystals were exposed to,

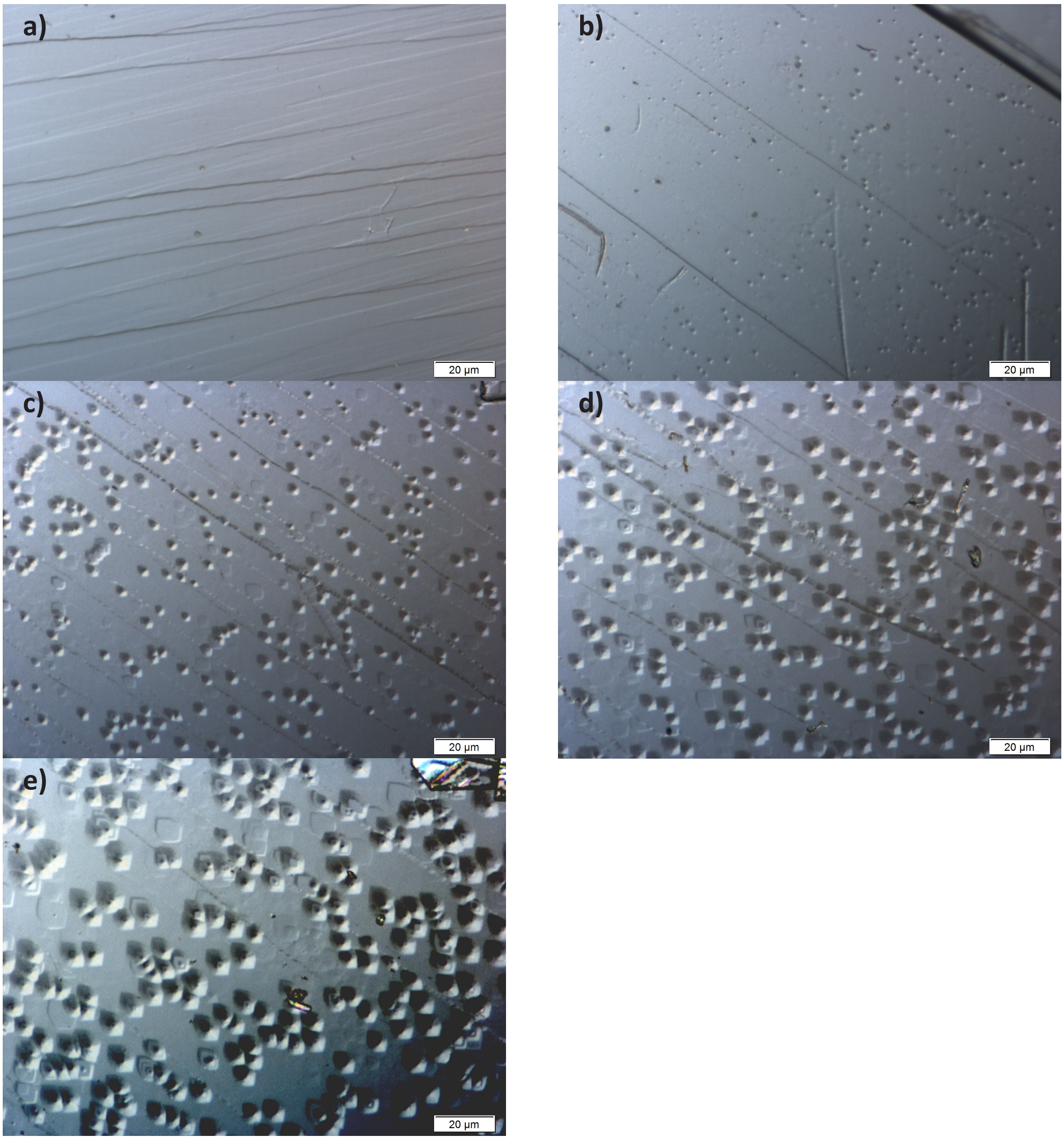

Fig. 5.8: A typical etching progress for a single calcite crystal (11.1 MeV/u, ^{197}Au, 1×10^{6} ions/cm^{2}) etched with EDTA + 5% acetic acid with the following etching times: a) 0 s, b) 5 s, c) 10 s, d) 15 s, e) 20 s.

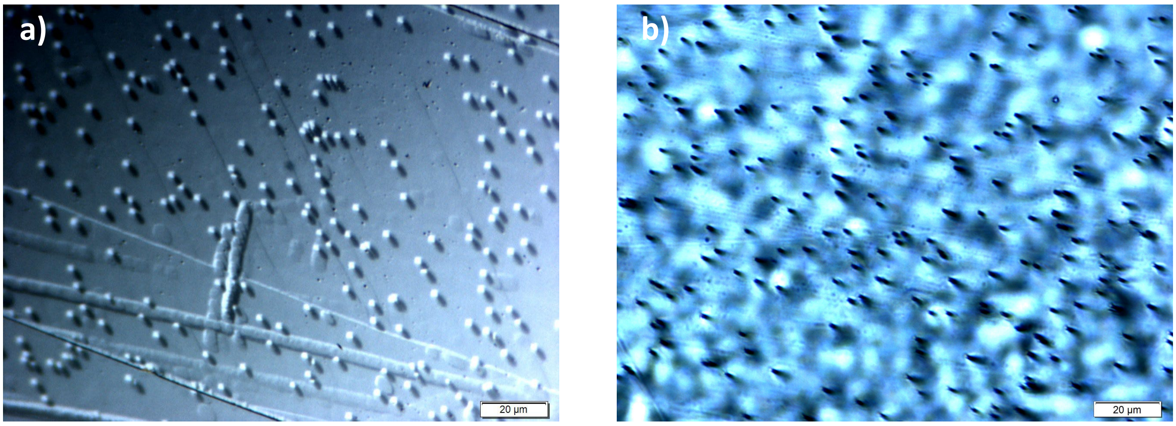

Fig. 5.9: An etched calcite crystal (a) with the corresponding PC-Foil (b). The counted areal density matches the fluence applied. (1×10^{6} ions/cm^{2}, 11.1 MeV/u, ^{197}Au)

within σ1. A very important point here is that the areal density of crystals showing well-formed etch pits and the areal density of crystals showing poorly formed etch pits does not differ outside error. This means that the geometrical quality of the etch pits does not play an important role for the analysis of areal density of tracks. All ion tracks will be etched, whether the resulting etch pits are well or poorly formed and therefore are available for interpretation and measurements.

To verify the amount of ions penetrating the crystals, polycarbonate foil was added on top of the crystals for the irradiation process. This foil is very sensitive to ion penetration and functions as a detector and reference for the amount of ions penetrating the sample. The foil was etched with 6N NaOH at 50°C for 50 min (1×10^6 ions/cm^2) to convert the track into an open pore of about 1.5 µm in diameter (Fig. 5.9, Picht et al.). The etch pits were counted. Results show that the areal density of the PC Foil (1.01×10^6 ions/cm^2 ±0.06) matches the areal density of the corresponding crystal (0.95×10^6 ions/cm^2 ±0.05) within error. These values also match the fluence induced. So it is reasonable to assume that all ions hitting the crystal leave etchable ion tracks which can be visualized.

5.2.6 EDTA + 5 % acetic acid ($C_2H_4O_2$) in 1:10 dilution with purified water

In order to find a way to gain better control of the etching speed, an etching solvent of EDTA + 5% acetic acid was diluted with purified water (1:10) to radically decrease the etching potential of the solvent. In anticipation of a slow etching speed etching times of up to 60 min were applied. As expected, the etchant works much more slowly than the undiluted etchant. Results of the procedure are etch pits which reach a higher ratio of the track etching rate (v_t) to the bulk etching rate (v_b) which is a highly desirable effect. The optical comparison of etch pits from non-diluted etchant with etch pits etched using diluted etchant show that after 60 min of etching the latter are much smaller, width: < 1 µm; length ~ 2 µm. They have a triangular shape instead of the hexagonal shape of common etch pits (Fig. 5.10). This observation matches the information found in literature (Chapter 2), that even different concentrations of etching solution influence the shape of the etch pits.

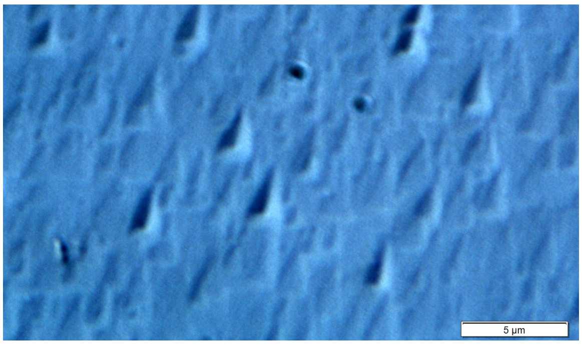

Fig. 5.10: Etch pits obtained with a diluted etchant. EDTA + 5% acetic acid in 1:10 dilution with purified water

5.2.7 Comparison of Ions used with regard to the size of the etch pits

Despite minor differences, etch pits resulting from irradiation with U-ions have the same properties as etch pits caused by irradiation with Au-ions when irradiated with the same energy and fluence. The shape of the etch pits is comparable, though a difference at the ion track in the middle of the etch pit is visible.

The overall size of the etch pits is slightly larger (Fig. 5.11). It is supposed that these effects are caused by the much larger energy deposition of the uranium ion in comparison to an Au-ion; higher energy loss (dE/dx) causes bigger ion tracks. Additionally, the etched ion track within

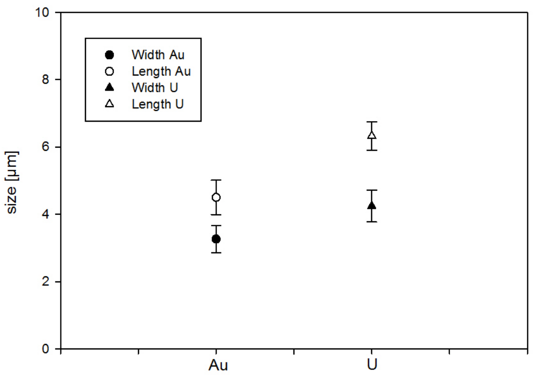

Fig. 5.11: Comparison of the size of etch pits on calcite crystals caused by gold and uranium irradiation. Both crystals have been etched with EDTA + 5 % of acetic acid for 10 s.

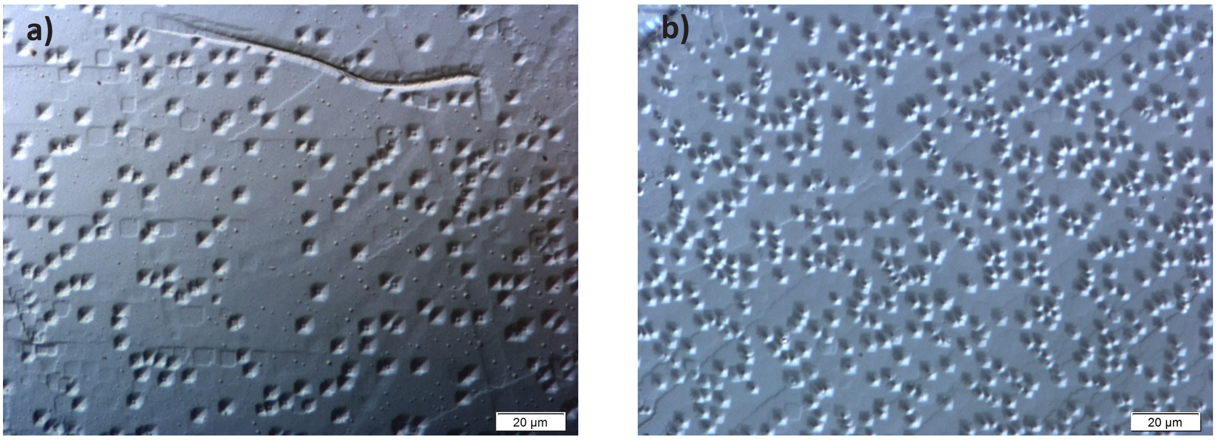

Fig. 5.12: Image of a calcite crystals etched with EDTA + 5% acetic acid for 10 s. The calcite on the left (a) is irradiated with 1×10^6 ions/cm^2 ^{197}Au, 11.1 MeV/u, the calcite on the right (b) is irradiated with 1×10^7 ions/cm^2 ^{238}U, 11.1 MeV/u. The shape of the etch pits is the same, the only difference is that crystals irradiated with ^{238}U show minimally larger etch pits and a larger ion track.

the etch pits, caused by the irradiation with U-ions is larger than the gold equivalent, which can be seen in Figure 5.12, where the ion tracks of uranium within the etch pit are better visible.

5.2.8 Further results

An interesting effect can be seen on the opposite side of the crystal where no direct ion beam had struck the surface. Due to the trigonal crystal system of calcite with a cleavage angle of 75° (Fig. 5.13) the ions hit the crystal on a tilted plane. On regions where the crystal is thin enough, the ions break through the crystal and exit on the opposite side, where the ion tracks can be etched, just as they are on the side where the ions hit the surface of the crystal directly. Geometrical analysis yielded a penetration depth of 80 µm ± 5 µm. SRIM calculated a projected range of 94 µm for ^{197}Au with an energy of 11.1 MeV. Thus the observed stopping depth matches the calculated SRIM projected range, within the known uncertainty of about 10 % (Fig. 5.14).

5.2.9 First experiment with carbonate rocks

After these first successes, experiments with carbonate rocks from the ***Wismut*** uranium mine were performed. 4 samples were etched, documented and then covered with mica, to detect fission products of uranium stimulated by irradiation with thermal neutrons. Etching of the samples had revealed numerous etch pits (Fig. 5.15), but none of these etch pits could be correlated with the traces of fission products on the mica. Therefore it is not finally clarified whether those etch pits are etch pits from induced fission tracks, or just etched dislocations. Figure 5.15 shows many cracks and scratches which indicate a strong mechanical stress to the sample. This

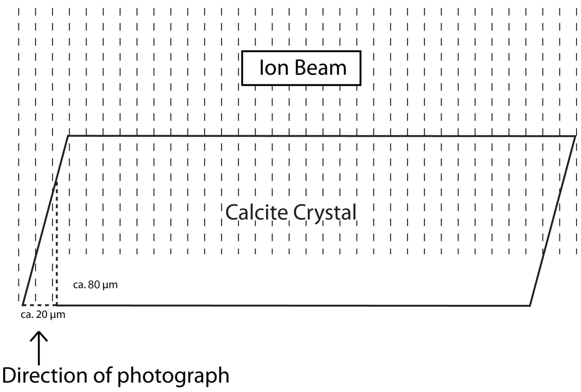

Fig. 5.13: Sketch of the irradiation geometry

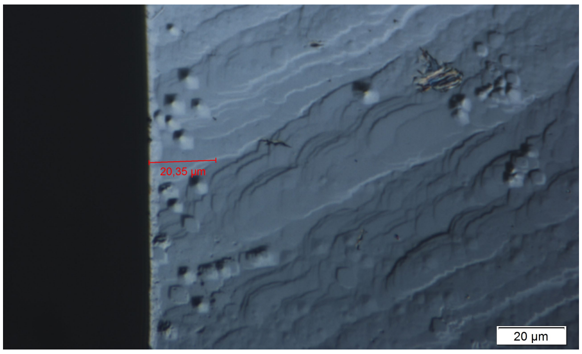

Fig. 5.14: Bottom of the crystal which was not exposed to the ion beam. Etch pits from ions passing through the crystal can be seen on the left side of the calcite

mechanical stress is often responsible for the formation of dislocations, so all the etch pits are very probably etched dislocations without any connection to the uranium content of the sample.

Following this result, a decision was made to postpone the investigation of defects resulting from natural fission fragments until a later time.

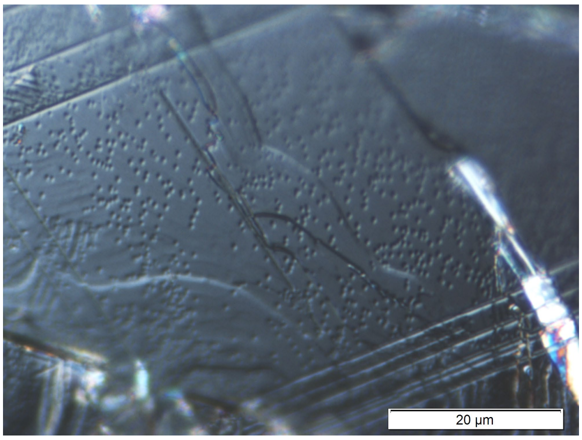

Fig. 5.15: Etch pits or etched dislocations of a carbonate rock from the Wismut uranium mine. The rock was etched with EDTA + 5 % acetic acid for 180 s

5.2.10 Cleanliness of the Samples before Etching

5.2.10.1 Introduction

After getting good etching results with EDTA + 5 % acetic acid on cleaved crystals, the idea came up to control the etching speed via the concentration of acetic acid in the etching solution (see Chapter 5.2.2). Two etching series have been performed and the results showed highly scattered etch pits length after 20 s of etching. To this moment of the doctoral thesis, the significant effect of dirt on the samples was not recognized yet, thus the Raman measurements were made, to rule out differences in the crystal lattice as reasons for the different etch pit length. When dirt was identified as possible reason, correlations between the growth rate of the etch pits have been performed and confirmed dirt as cause for the different etch pit length after 20 s of etching. The following chapter shows the gained results in detail.

5.2.10.2 Comparison of the etch pit size and quality in relation to cleanliness

Optical comparison

It is quite easy to recognize dirty samples under the microscope, although no difference between dirty and clean samples is visible with the naked eye.

On the samples, dirt appears as white to grey bubbles on the surface of the crystal (Fig. 5.16). These bubbles are unevenly distributed and the sizes range from < 1 µm up to 4 µm in the examples shown but it is a likely assumption that even bigger structures are possible. The bubbles are rounded in most cases, but elongated forms are possible as well. In some cases bubbles of roughly the same size are grouped in certain areas of the crystal. This dirt is thought to consist of dust and various greasy substances. The dust may come from the storage of the samples; the greasy substances originate in handling the samples. Some other reasons may be residues from felt tip pens used for example to mark the irradiated side of the sample (Fig. 5.19). The bubbles result from the cleaning process before the etching of the samples. It has been observed with the microscope that the cleaning liquid (pure water, ethanol) encloses the dust particles and then sediments onto the surface of the sample.

Clean samples, by contrast, have a mostly smooth surface with only a very few small particles similar to the bubbles on the dirty samples. Of course, there are some scratches and break-ups on the clean samples but these structures do not affect the etching speed of the etch pits.

The coverage of the sample with dirt has a significant effect on the etching process and therefore on the size and quality of the etch pits. A first effect is a reduced etching speed. The dirt, especially greasy residues act as a coating and protect the surface from being etched.

A second significant effect is the reduced quality of the etch pits. Etch pits on clean samples have a very clear, sharp geometrical form, depending on the etchant. Lines are straight and angles are

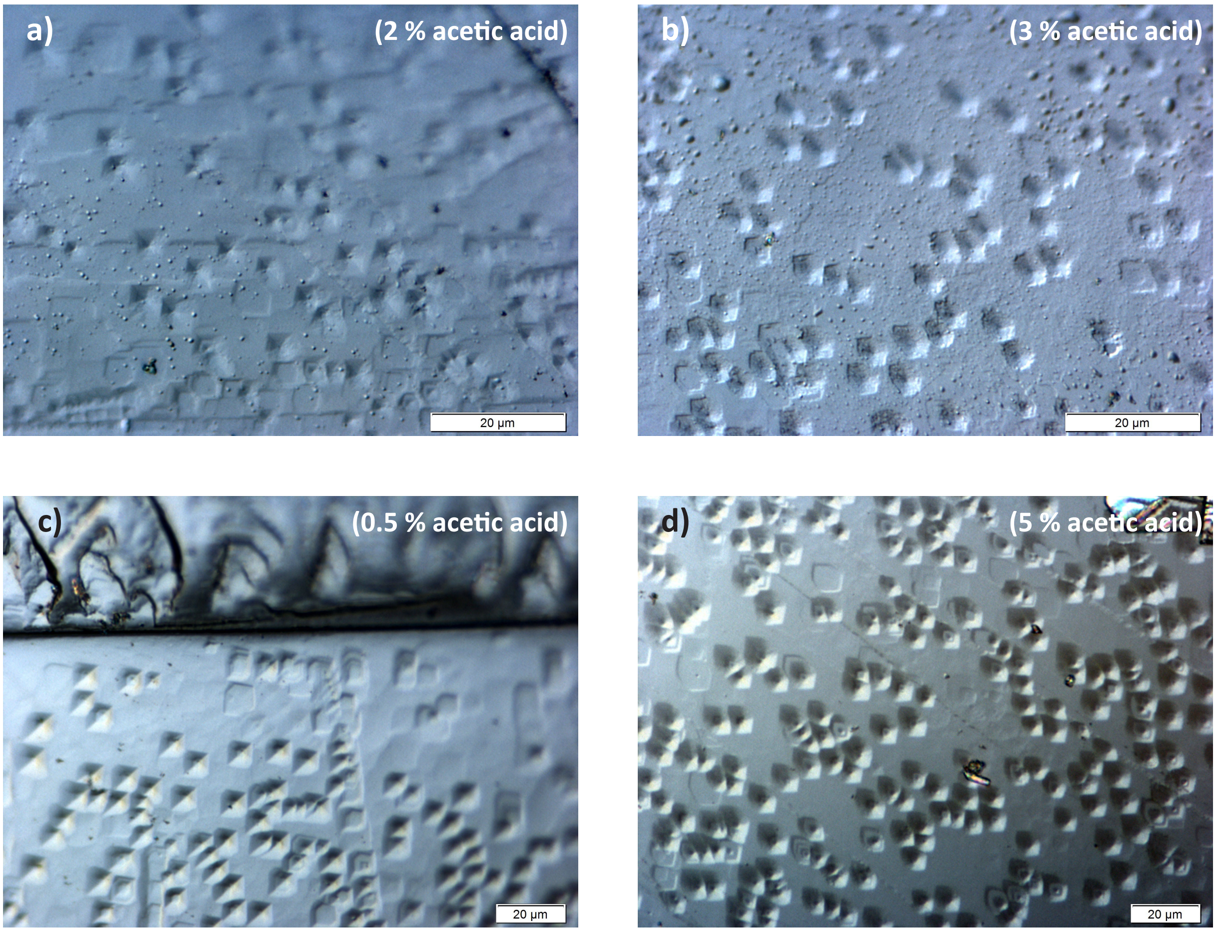

Fig. 5.16: Figure 5.16 a)-d) shows a comparison between dirty and clean samples from etching Series I and II respectively. All samples shown have been irradiated with 11.1 MeV/u, 1×10^{6} ions/cm^{2}, Au-ions and etched with EDTA + 5 % acetic acid at a temperature of 21 °C for 20 seconds. The figures 5.16 a) and 5.16 c) show crystals from Series I. The sample in image a) (2 % acetic acid) is dirty, with bubbles on the surface and poorly shaped etch pits, c) (0.5 % acetic acid) with a smooth surface and well shaped etch pits. The figures 5.16 b) and 5.16 d) show crystals from Series II. Image b) (3 % acetic acid), dirty, with bubbles on the surface and poorly shaped etch pits. The bubbles are partly grouped cluster of roughly the same size. Image d) (5 % acetic acid) shows a smooth surface and well shaped etch pits. Please note that images a) and b) are taken with a 100x objective and images c) and d) are acquired with a 50x objective.

clear. On dirty samples the etch pits are kind of frazzled with no definite shape. One theory is that the coverage with dirt prevents the etch pits from being etched consistently and therefore the edges of the etch pits are not straight.

5.2.10.3 Statistics

In order to study the growth development of the etched ion tracks through time, size measurements were performed. After every stage of etching (5, 10, 15, 20 (±0.25) s) 100 values for width and length were determined to achieve a statistically significant result.

Figure 5.17 show the length of all etch pits from the two series made after an etching time of 20 s with the respective etching solution. The etching with 0.5 % acetic acid from Series I and the etching with 5 % of acetic acid from Series II were taken as a reference, based on their clean surface and the resulting perfectly shaped etch pits with a length of about 10 µm. The use of 0.5 and 5 % as reference values with more or less the same properties from both ends of the scale show that the concentration of acetic acid in the etching solution does not play a major role for the size and etching speed of the etch pits.

As an example of the effect of dirt on the growth speed and size of the etch pits, the results of 0.5 and 2 % from Series I and 5 and 3 % from Series II were compared.

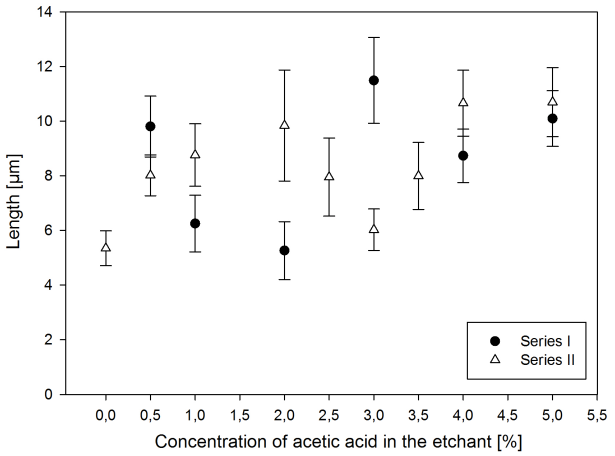

Fig. 5.17: This figure shows the length of etch pits of both series after 20 s of etching with the corresponding concentration of acetic acid in the etchants. It can be seen, that the amount of acetic acid in the etchants is not related to the length of the etch pit.

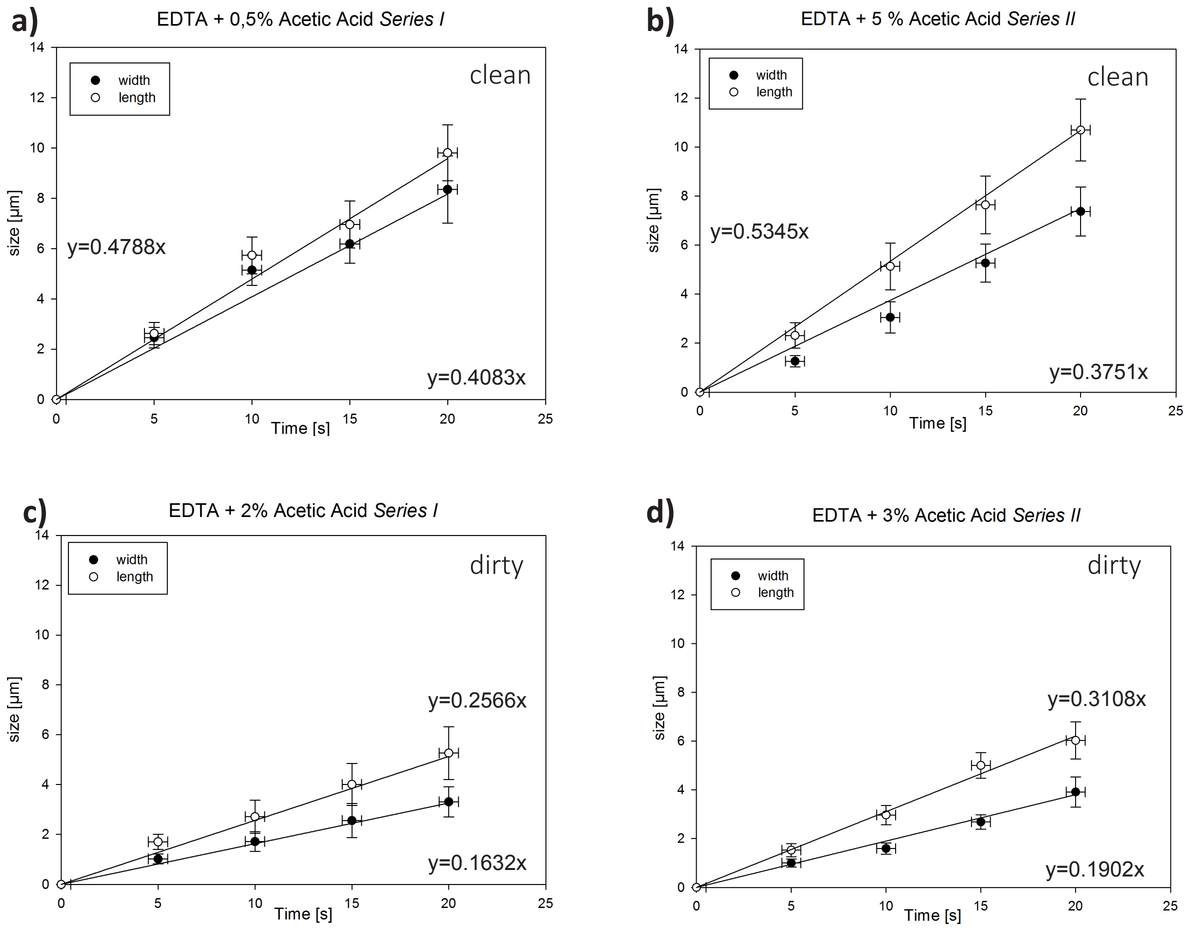

Fig. 5.18: This figure shows the statistical analysis of the dirt-effect while etching irradiated calcite crystals with EDTA + the specific percentage of acetic acid. The corresponding etching procedures (a & c, and b & d) show very clearly that the dirt reduces the etching speed to half the speed of clean calcites.

In Series I the etch pits of etched ion tracks etched with EDTA + 0.5 % acetic acid and 2 % acetic acid are taken as an example. In comparison the etching speed of the 2 % etching is within error half the speed of the 0.5 % etching. The etch pits of the 2 % etching reach only about 5 µm after 20 s whereas the etch pits of the 0.5 % etching reach the same value after just 10 s of etching (Fig. 5.18 a + c). The gradient of the etch pit growth confirms this observation. The gradient for EDTA + 0.5 % acetic acid is 0.48, whereas the gradient of EDTA + 2 % acetic acid is only 0.26. Additionally, an optical comparison of the two crystals (Fig. 5.16) confirms this statement.

The same observation could be made in Series II. The etch pits of etched ion tracks etched with EDTA + 5 % acetic acid and 3 % acetic acid are taken as an example. In comparison the etching speed of the 3 % etching is within error nearly half the speed of the 5 % etching (Fig. 5.18 b + d). The gradient of the etch pit growth confirms this observation. The gradient for EDTA + 5 % acetic acid is $y=0.53x$, whereas the gradient of EDTA + 3 % acetic acid is only $y=0.31x$ An optical comparison of the two crystals (Fig. 5.16 b + d) confirms this statement.

Checking the pictures from the other etchings of the two series confirm the theory of dirt and/or grease slowing down the etching speed. All etchings with a small value after 20 s proved to be dirty. Thus all results with etch pits of relatively small length can be explained by a dirty surface, compared to a reference length of about 10 µm for clean ones.

Additionally, other quality factors like twinning, crystal defects, inclusions, evenness of the surface etc. also play a role for the etching process but it is hard to quantify their influence on the etching result.

5.2.10.4 The effect of dirt on Raman measurements

In Fig. 5.20 a + b the same image of a calcite crystal can be seen. The etch pits left and right of the black line are significantly different. On the left hand side the etch pits are smaller and have an indistinct geometry due to dirt on the surface. On the right hand side, the clean one, the etch pits are larger with a clean geometry. The differences in size are also observable in the corresponding histograms (Fig. 5.20 c + d). To rule out differences in the crystal lattice as cause for the differences in the etch pit appearance, Raman spectra were made of both sides of the crystal. The spectra in the corresponding areas showed no difference between these two areas (Fig. 5.20 e). This shows that the two sides have the same crystal property and that dirt on the surface has no major effect on the Raman signal of the calcite crystals.

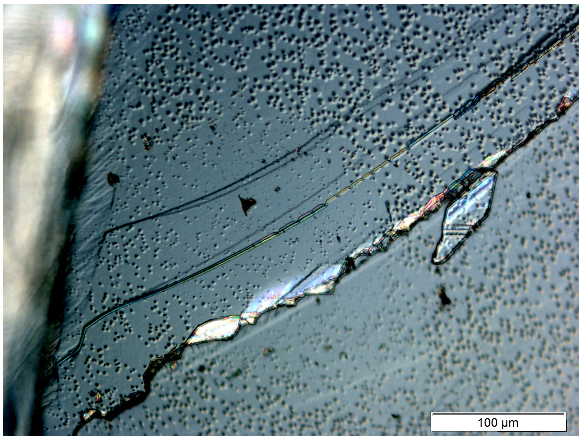

Fig. 5.19: Calcite after 10 s in EDTA + 5% acetic acid. The blank spot on the left of the crystal is the area where the marking dot was. This dot marked the irradiated side of the crystal and prevented instant etching of the underlaying ion tracks

5.3 RESULTS FOR DOLOMITE AND ARAGONITE

After the successful etching experiments with EDTA + acetic acid and calcite, an approach was made to transferring the experience gathered to other minerals: dolomite and aragonite. Experiments showed that this etching solution is not transferable to dolomite and aragonite. The dolomite showed no reaction at all to EDTA + acetic acid, even after 180 s of etching (Fig. 5.21). The surface looked just as it had looked before the etching process. Aragonite showed only a limited changes on the surface for the same etching time,

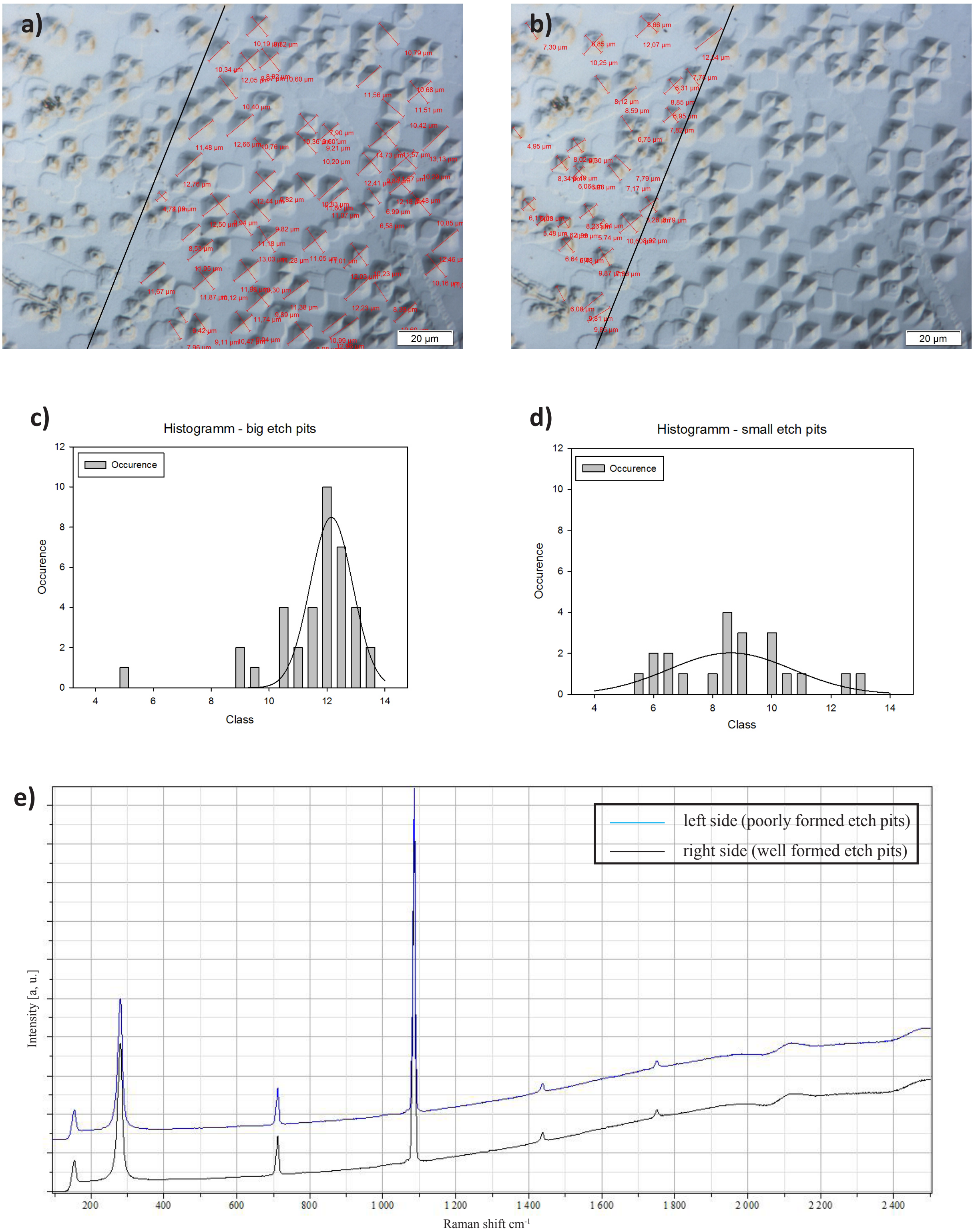

Fig. 5.20: Figure 7.13a + b show a crystal with well and poorly (caused by dirt) formed etch pits. Measurements of the length of the etch pits and an analysis in a histogram (Figure 7.13c + d) emphasize the impression of a difference in size: the poorly formed etch pits on the left are smaller than the well shaped etch pits to the right of the black line. An investigation with Raman spectroscopy (Figure 7.13e) showed no differences between left side and the right side. So Raman is not affected by dirt-effects.

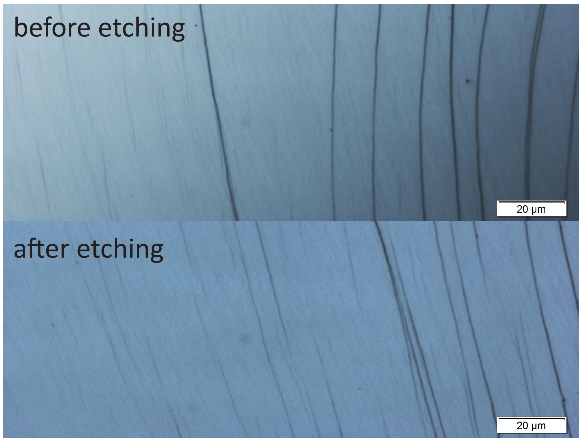

Fig. 5.21: Irradiated dolomite (1×10^6 ions/cm^2, 11.1 MeV/u, ^{197}Au) before and after etching with EDTA + 5 % acetic acid for 180 s. No difference is visible

but here no clear hexagonal pattern from the overlaying mask could be found, thus the etching of tracks could not be confirmed. After these results, all further experiments on dolomite and aragonite were stopped and postponed to a later point in time. The decision was made to concentrate on calcite first, and then continue with experiments on dolomite and aragonite.

5.4 Discussion

Etching experiments on swift heavy ion irradiated calcite single crystals reveal etch pits. These etch pits can be analyzed for size, shape, growth and areal density. The most reliable etching solvent of the four solvents tested is Na-EDTA + 5 % acetic acid in a proportion of 1:1 (Macdougall & Price, 1974), if the etching procedure is performed very carefully. This etching agent reveals etch pits with a length of about 10 µm and a width of about 8 µm. All other etching procedures preserved from former attempts to etch calcite to visualize fission tracks are less advantageous. All attempts to etch with NaOH were unsuccessful; formic acid turned out to be too strong in the original concentrations. First experiments with diluted etching solvents turned out to be very promising, because a slow, soft etching process is more controllable than a fast one. The etch pits themselves show predictable behavior: the growth is linear; the shape consistent in all etchings with the same etchant. The areal density of the etch pits matches the fluence of ions induced. As long as the etching time for the corresponding agent is adapted carefully, all induced ions can be made visible through etch pits.

6

VISUALIZATION OF HEAVY ION TRACKS BY HNO_3 ETCHING TECHNIQUES

CONTENTS

6.1 INTRODUCTION

After the initial success of establishing a working etching procedure with EDTA + acetic acid (see Chapter 5), all requirements for an optimum etching result were reconsidered, in order to check whether the procedure determined fulfils these requirements, or if there is space for a further optimization of the etching process. For optimal etching several conditions need to be fulfilled:

- Each ion track should lead to a single etch pit, i.e. the etching efficiency should be 100 %.
- The etching solution should be selective i.e. the track etch rate (v_t) should be larger than the bulk etch rate (v_b).
- The overall etching process should be slow enough to handle the samples in a controllable way.
- The etch pits should be as homogeneous as possible, allowing automated analysis by optical microscopy (standard method in geology).
- The etchant should be easy to prepare and should be as safe as possible while handling (not toxic).

A careful analysis showed that the established method does not fulfil all requirements completely satisfactorily, so ways to optimize the etching process were researched.

6.1.1 Problems with sawed and polished samples.

Additionally, an unexpected problem gave extra motivation to search for an alternative etching method: while etching an in epoxy-embedded and polished sample (see Chapter 4) with EDTA + acetic acid, a coating of some kind formed on the surface of the samples (Fig. 6.1). This coating turned out to be very persistent and it resisted all cleaning attempts with ethanol, no matter how harsh they become after a while. The result of the cleaning attempts was a scratched sample surface which was considered as damaged. The reason for this coating could never finally be determined. Possible causes for the coating could be impure chemicals used for the etching and cleaning procedure, although such problems never occurred before or after this etching.

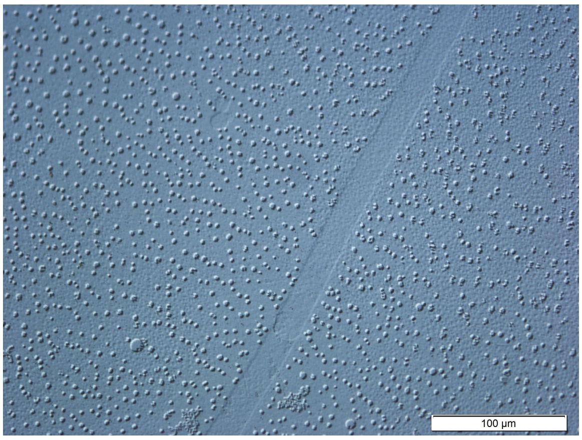

Fig. 6.1: Coating on the epoxy embedded calcite. The little objects on the surface represent dirt of some kind which resisted every cleaning attempt.

Research suggests that a possible explanation is a vulnerability of epoxy resin to acetic acid, at least acetic acid is used to clean spoiled epoxy resin in facility management and is described as non-resistant to acetic acid according to a product data sheet of the manufacturer. Although additional tests could not replicate the results of the previous experiment regarding the coating, to avoid unnecessary problems an alternative etching solution had to be found.

6.1.2 Alternative etching solutions described in literature

After testing many non-suitable etching solutions at the beginning of this study (see Chapter 5.2), the literature was scanned once again for alternative etching solutions.

A promising approach was found in KEITH & GILMAN (1960), who used among other things highly diluted nitric acid (HNO_3) to etch calcite crystals for the investigation of the twinning of calcite. Besides the good results of KEITH & GILMAN with HNO_3, nitric acid is established in thermochronological laboratories for the etching of apatite and is therefore an accepted chemical which people in laboratories are used to. KEITH & GILMAN used 0.7 % HNO_3 for 90 s at room temperature to etch their calcite samples.

6.2 RESULTS

Experiences with the etching recipes of older publications showed, that their etching procedures are often too strong for the application of etching tracks induced by swift heavy ion irradiation. The reason for this is the much smaller size of the tracks in this study in comparison with the crystal lattice etching performed by scientists in the past. Therefore, for a first approach, the original recipe of KEITH & GILMANN of 0.7 % HNO_3 for 90 s at room temperature was modified to 0.91 % HNO_3 for 15 s at room temperature (Fig. 6.2). Results show that even the reduction of the etching time to ⅙ of the original value is not sufficient. The etch pits become too large (about 100 µm) and overlap each other (Fig. 6.3). On the other hand, all etch pits have a very distinct black dot in the middle of the etch pit, which is interpreted as the actual etched ion track.

After this first result, the etching time was reduced twice, to 5 and to 3 seconds, but even these very short etching times were still too strong and the etch pits were still overlapping.

The breakthrough for HNO_3 was rather an unplanned experiment. Using the embedded sample described in Chapter 6.1.1, which by now was suffering from many cleaning attempts, the intention was to test what influence the rather strong HNO_3 etching solution would have on the coating of the sample, which was ruined anyway. For this purpose the sample was immersed for 1 s in the 0.91 % HNO_3 solution, and the result was highly pleasing: good shaped, small sized etch pits were visible on the surface of the embedded calcite, which was much scratched from the previous

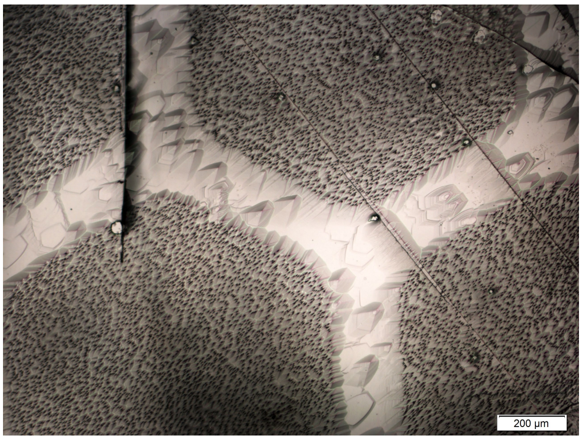

Fig. 6.2: Etch pits revealed with 0.91 % HNO_3 for 15 s at room temperature. (1×10^6 ions/cm^2, 11.1 MeV/u, ^{197}Au)

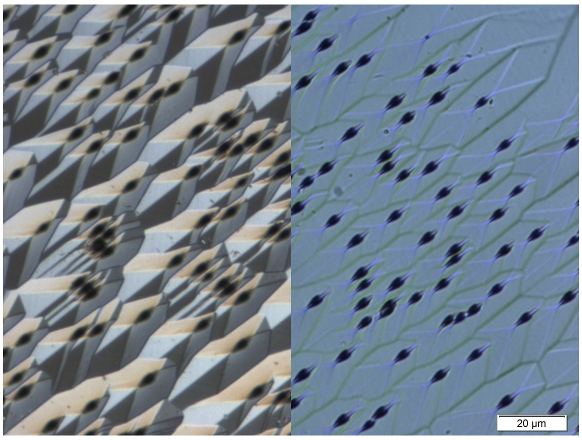

Fig. 6.3: Etch pits revealed with 0.91 % HNO_3 for 15 s at room temperature. (1×10^6 ions/cm^2, 11.1 MeV/u, ^{197}Au)

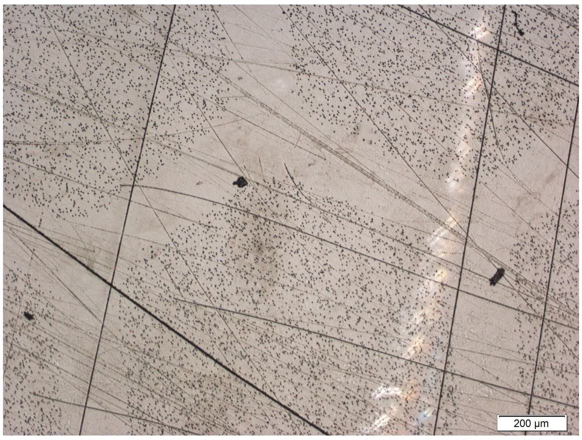

Fig. 6.4: Etch pits on the formerly coated sample at 5 x magnification. 0.91 % HNO_3 was able to display the etch pits. (1×10^6 ions/cm^2, 11.1 MeV/u, ^{197}Au)

Fig. 6.5: Etch pits on the formerly coated sample. 0.91 % HNO_3 for 1 s was able to display the etch pits. (1×10^6 ions/cm^2, 11.1 MeV/u, ^{197}Au)

cleaning attempts (Fig. 6.4). The coating of the sample must somehow have protected the ion tracks from being etched with EDTA + 5 % acetic acid, so HNO_3 had accomplished three things: it had dealt with the coating of the sample, it had etched the ion tracks in the required way (Fig. 6.5) and it had not affected the epoxy resin.

With these experiences the parameters for the subsequent systematic etching series took shape: even lower concentrations, at lower temperatures, for short times.

6.2.1 Optimizing the Etching Solvent

After these first experiments, it becomes clear that calcite is very sensitive to nitric acid and that one has to be very careful not to overetch and therefore destroy the calcite sample. On the other hand, the results showed that nitric acid is highly suitable to display the ion tracks induced in the samples, if the concentration of the acid and the etching time are chosen right. Therefore a series of experiments were performed to fine tune the concentration, temperature and etching time and to match them with one another.

Two etching series were performed at two temperatures (15 and 21 °C ± 0.5 °C) in highly diluted HNO_3 with concentrations of 0.91, 0.091, and 0.0091 %. After the experiences of the first experiments, rather short etching times of 2, 4, 6 and 8 (± 0.25) s were scheduled. The samples used for this study were once again cleaved calcite crystals which were irradiated at UNILAC, GSI with Au - ions at an energy of 11.1 MeV/u and a fluence of $1{\times}10^6$ ions/cm^2. The experiments showed that 0.091 % HNO_3, at a temperature of 15 °C with a pH level of 2.05 (± 0.1) provides the best result regarding shape and size of the etch pits. This etching solution etches the tracks caused by swift heavy ions to a max. length of the etch pit of about 15 µm and a width of about 14 µm after 8 s. After 4 s of etching, the length of the etch pit reaches a length of about 9 µm, which roughly matches the size of the etch pits etched for 20 s in EDTA + acetic acid. This concentration has been identified as the most useful and will be used in further experiments. For a fluence of $1{\times}10^6$ ions/cm^2 etching times over 8 s are not recommended, because the etch pits get too big and therefore overlap. This effect is already visible after 8 s of etching, so that no further etching is necessary.

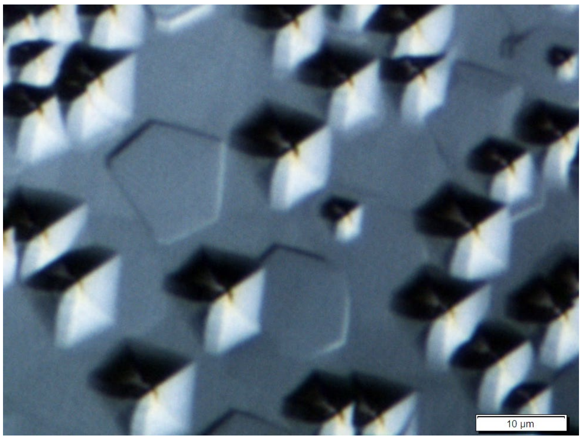

Fig. 6.6: Etch pits of HNO_3 etched ion tracks. Etching parameters: 0.091 % HNO_3, 2 s, 15 °C.

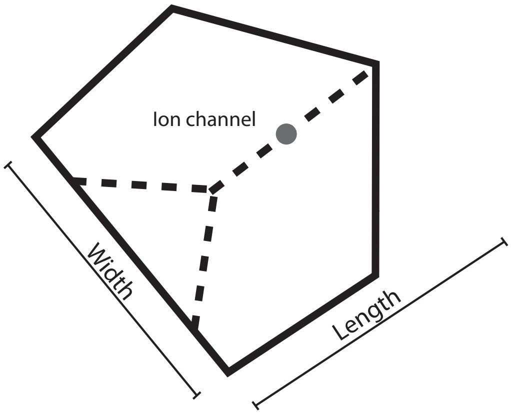

Fig. 6.7: Sketch of an HNO_3 etched ion track. It has a pseudo pentagonal shape with the ion track in the middle of the etch pit.

6.2.2 Description of the Etch Pits

6.2.2.1 Shape

The etch pits revealed have a pseudopentagonal shape with a flat end which is designated as the lower end of the etch pit (Fig. 6.6). The two sides starting from this lower end are almost at right angles. At the other end of these lines the etch pit tapers to a tip at what is designated as the top of the etch pit. From the tip to about ⅔ of the length of the etch pit, a line runs down the

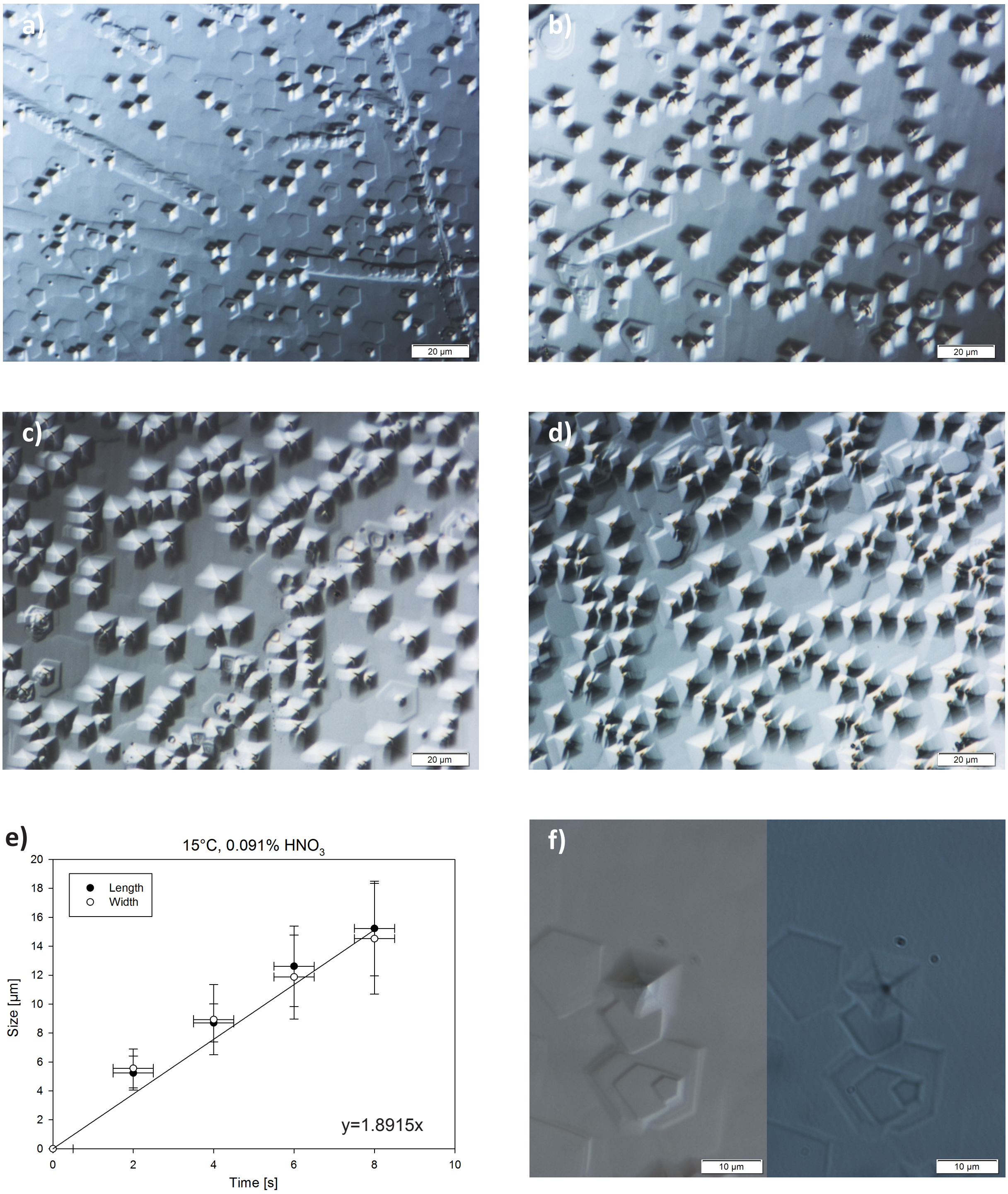

Fig. 6.8: A typical etching progress for a calcite crystal etched with 0.091 % HNO_3 at 15 °C. The images show the etching progress at a) 2 s, b) 4 s, c) 6 s and d) 8 s. Image e) shows the associated growth diagram. Image f) shows a single etch pit after 4 s in reflected light on the left and in transmitted light on the right. The transmitted light image clearly shows the ion track as a black dot in the middle of the etch pit. (1×10^6 ions/cm^2, 11.1 MeV/u, ^{197}Au)

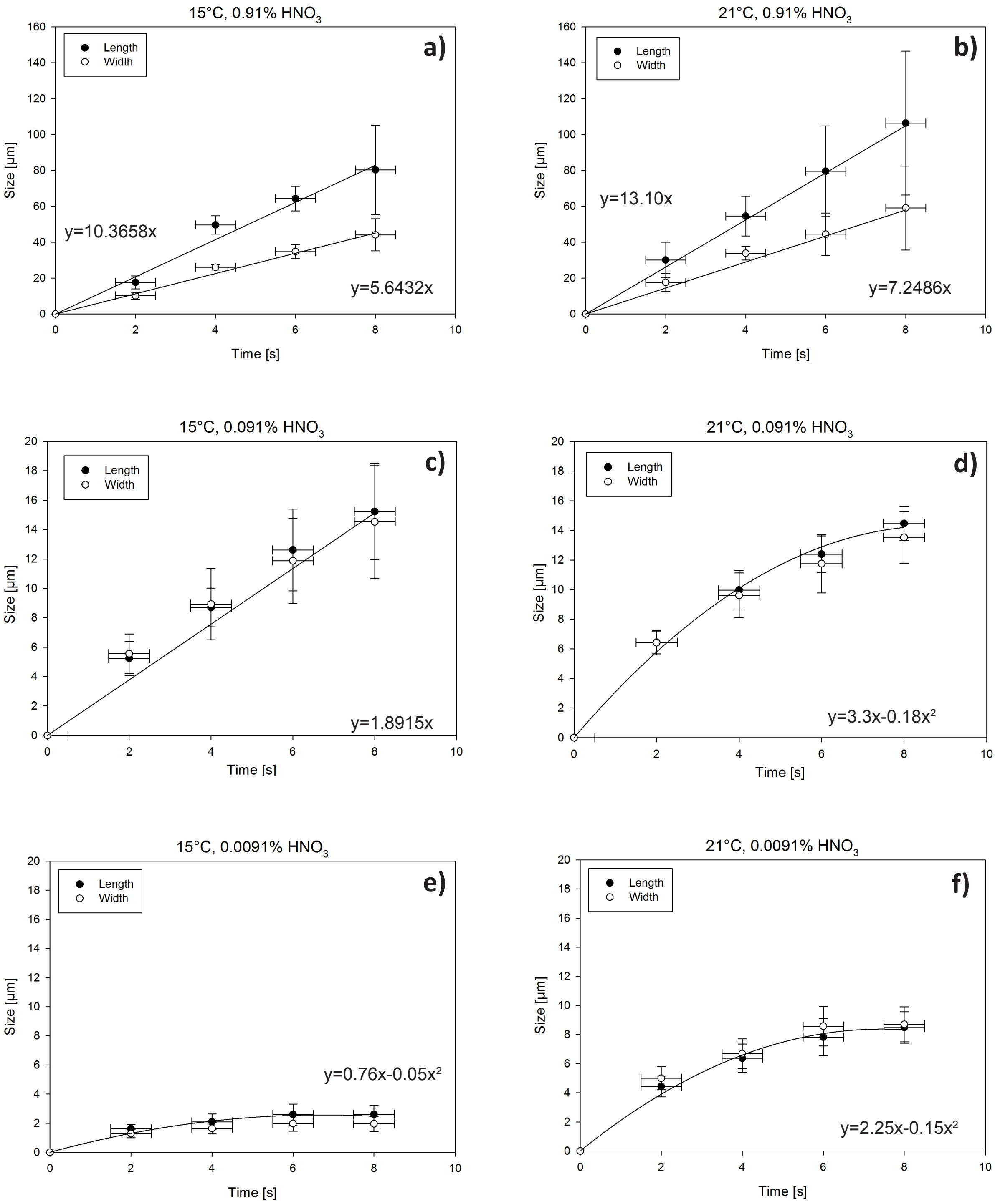

Fig. 6.9: Growth diagrams for the different concentrations and temperatures of the etching series performed. a) 15 °C, 0.91 % HNO_3, b) 21 °C, 0.91 % HNO_3, c) 15 °C, 0.091 % HNO_3, d) 21 °C, 0.091 % HNO_3, e) 15 °C, 0.0091 % HNO_3, f) 21 °C, 0.0091 % HNO_3. At concentrations of 0.91 % and 0.0091 % the etch pits obtained using an etching solution at a temperature of 21 °C are bigger than those obtained with a solution at 15 °C. At a concentration of 0.091 % the sizes of the etch pits obtained at different temperatures are approximately the same. This concentration is determined as the most useful and will be used in further experiments.

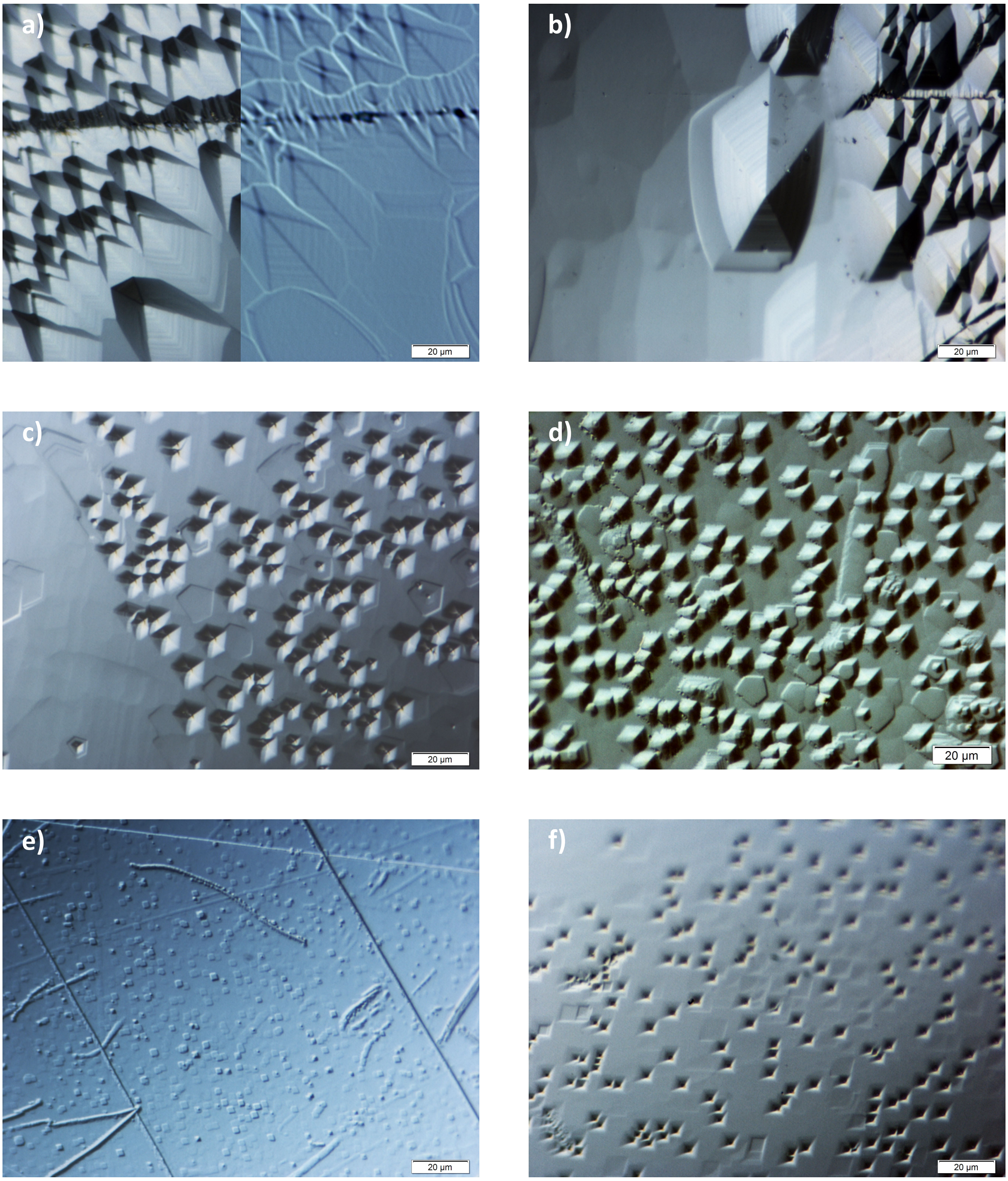

Fig. 6.10: Images of the different concentrations and temperatures of the etching series performed. The images have been taken after 4 s of etching. a) 15 °C, 0.91 % HNO$_3$ (image of etch pits, reflected light and transmitted light next to each other), b) 21 °C, 0.91 % HNO$_3$(image of etch pits at the border to a non-irrradiated area), c) 15 °C, 0.091 % HNO$_3$, d) 21 °C, 0.091 % HNO$_3$, e) 15 °C, 0.0091 % HNO$_3$, f) 21 °C, 0.0091 % HNO$_3$. It is easy to see that the shape of the etch pits differs with the different concentrations. At 0.91 % HNO$_3$ the shape of the etch pits is elongated with length > width, whereas the etch pits obtained with concentrations of 0.091 % and 0.0091 % have a more rectangular shape with length = width. The etch pits obtained with a concentration of 0.091 % at 15 °C etching temperature have the best shape and the right size to determine the areal density and therefore this etching recipe is used for all further etching procedures.

middle of the etch pit. From the end of this bar, another two lines branch at an angle of about 45° (Fig. 6.7). The long line in the middle of the etch pit led to the definition of its direction as being the length of the etch pit. To summarize, the whole etch pit looks like a rectangle with a superimposed tip.

Overall the etch pit is build up very symmetrically. An important observation is that the shape of the etch pit changes with decreasing concentration of HNO_3. With highly concentrated HNO_3 the etch pit is far longer than it is wide, with a length/width ratio of about 2. With decreasing concentration, the length/width ratio becomes smaller and reaches almost 1 at 0.091 % HNO_3 (Fig. 6.9). The depth of the etch pits is hard to determine. But due to the fact that it is not possible to focus either the edge of the etch pit or the bottom of the etch pit, and that the etch pits are barely visible without DIC, it is likely to assume that - for the as standard defined concentration of 0.091 % HNO_3 - they are as shallow as the etch pits etched with EDTA + acetic acid with their 200 - 300 µm depth. The very shallow structures with the same shape as the etch pits are etched dislocations like the Type B dislocations of the EDTA + acetic acid etching method (Fig. 6.8 a+f) described in Chapter 9.1.

6.2.2.2 Statistics

The growth diagrams show that for the etching parameters 15 °C, 0.91 % HNO_3, 21 °C, 0.91 % HNO_3 and 15 °C, 0.091 % HNO_3, the size of the etch pits increases linearly within error. For 21 °C, 0.091 % HNO_3, 15 °C, 0.0091 % HNO_3 and 21 °C, 0.0091 % HNO_3, the growth curve is not linear. The growth rate of the etch pit size decreases during the etching process. The size of the etch pits increases fast at the beginning and with increasing time merges into a plateau.

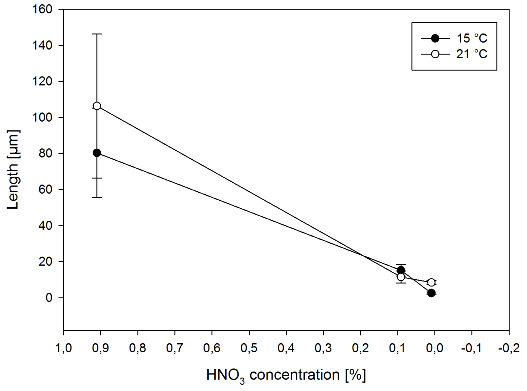

Fig. 6.11: HNO_3 concentration versus the etch pit length. A reduction of the concentration by a factor of 10 leads to a reduction in the length of the etch pits by a factor of 5.

It is also visible that a reduction of the concentration of HNO_3 by a factor of 10 leads to a reduction of the size of the etch pits by a factor of 5 (Fig. 6.11). For 0.91 % and 0.0091 % HNO_3 the etch pits etched at a temperature of 21 °C are bigger than the etch pits etched at 15 °C, which was to be expected. For 0.091 % of HNO_3 the etch pits at 15 °C and 21 °C have the same size within error (Fig. 6.9 + Fig. 6.10). This shows that at this concentration the temperature is not so important for the resulting etch pit size. Due to the fact that this concentration shows the best etching results, this behavior is preferable, because it means that the most used etching solution is not very temperature-sensitive and is therefore easy to handle. Figure 6.8 shows a typical etching progress of one calcite crystal, etched with 0.091 % HNO_3 at 15 °C.

Besides all results, it must not be forgotten that all sizes of the etch pits are highly dependent on the cleanliness of the samples. This variable has a very big effect on the etching result.

6.2.2.3 Areal density

Results show that the areal density of the PC Foil (1.01×10^6 ions/cm² ±0.06) matches the areal density of the crystal (0.98×10^6 ions/cm² ±0.07) within error. Thus it is a reasonable assumption that all ions hitting the crystal leave etchable ion tracks which can be visualized.

6.3 DISCUSSION

After modifying the etching recipe of KEITH & GILMAN, HNO_3 works very well as an etching solution for calcite. The best result is achieved with a concentration of 0.091 % at a temperature of

15 ° C with an etching time of 4 s. The etch pits revealed have a pseudopentagonal shape with clear edges, if the crystal was clean during the etching process.

The etch pits show two different growth models. Whereas the etch pits with the etching parameters 15 °C, 0.91 % HNO_3, 21 °C, 0.91 % HNO_3 and 15 °C, 0.091 % HNO_3, grow linearly, the etch pits etched with 21 °C, 0.091 % HNO_3, 15 °C, 0.0091 % HNO_3 and 21 °C, 0.0091 % HNO_3 show a non-linear growth. A possible reasons for the different growth models might be the variation in sensitivity of calcite for different etching parameters, such as etching temperature and concentrations of HNO_3 of the etching solution.

When etching with 0.091 % HNO_3 at 15 °C, the etch pits show a linear growth and reach a size of about 15 µm after 8 s of etching. After 4 s, which is the recommended etching time for a fluence of 1×10^6 ions/cm^2, they reach a size of about 9 µm, which is ideal for further investigations. Therefore, these etching parameters are used as standard etching parameters for etching with HNO_3.

7

COMPARISON OF EDTA + ACETIC ACID AND HNO_3 AS ETCHING AGENTS

CONTENTS

7.1 Shape and Size

For the comparison of the etch pits, the concentrations of EDTA + acetic acid and HNO_3 are used, which were determined during the experiments as the most useful. These are: 0.091 % HNO_3 and EDTA + 5 % acetic acid.

In comparison, the ion tracks induced in calcite crystals behave very different when etched with HNO_3 or with EDTA + acetic acid. As expected from the literature at hand (see Chapter 2), the etch pit geometry depends on the solution: tracks etched in EDTA + 5 % acetic acid have an elongated pseudohexagonal shape, while 0.091 % HNO_3 produces pseudopentagonal-shaped etch pits (Fig. 7.2 - Fig. 7.5). Another difference is the size of the etched ion track, which is significantly bigger on the HNO_3 etched calcite crystal. The ion track is particularly clearly visible in transmitted light, which also has further advantages, see Chapter 9.4. The general etching speed of HNO_3 is faster than the etching speed of EDTA + acetic acid. With 0.091 % HNO_3, the etch pits reach a length of about 9 µm after 4 seconds. EDTA + ace-

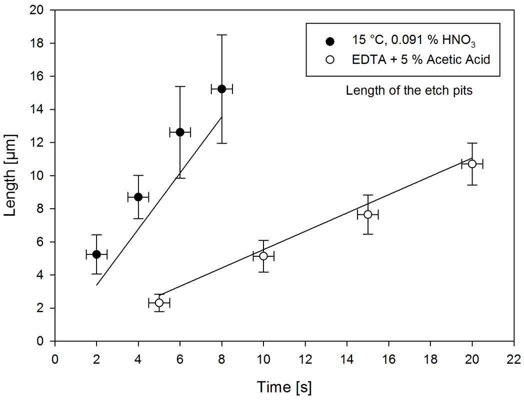

Fig. 7.1: Comparison of the length of the etch pits etched with 0.091 % HNO_3 or EDTA + acetic acid. 4 s in HNO_3 provides the same result as 20 s in EDTA + acetic acid

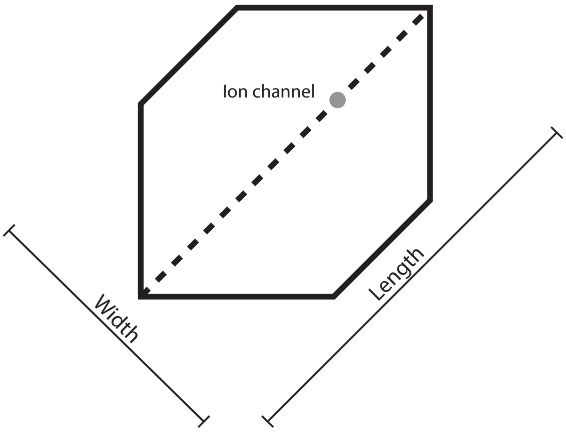

Fig. 7.2: Sketch of an EDTA - acetic acid etched ion track. It has a pseudohexagonal shape with the ion track in the middle of the etch pit.

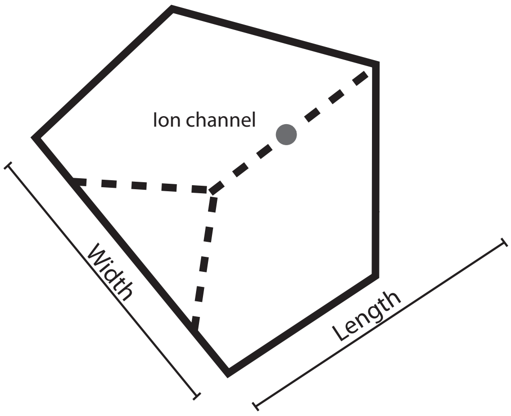

Fig. 7.4: Sketch of an HNO_3 etched ion track. It has a pseudo pentagonal shape with the ion track in the middle of the etch pit.

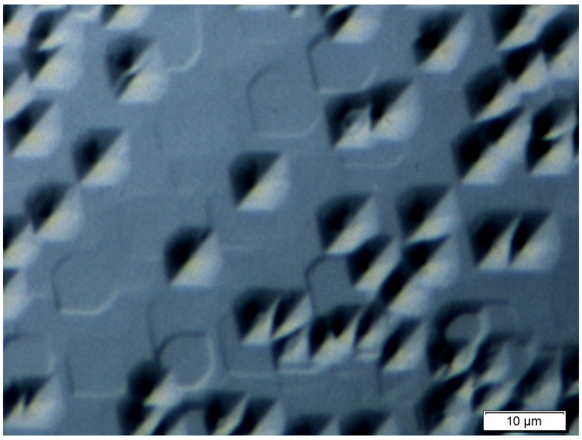

Fig. 7.3: Etch pits in the middle of the picture. 20 s, EDTA + 5 % acetic acid (1×10^6 ions/cm^2, 11.1 MeV/u, ^{197}Au)

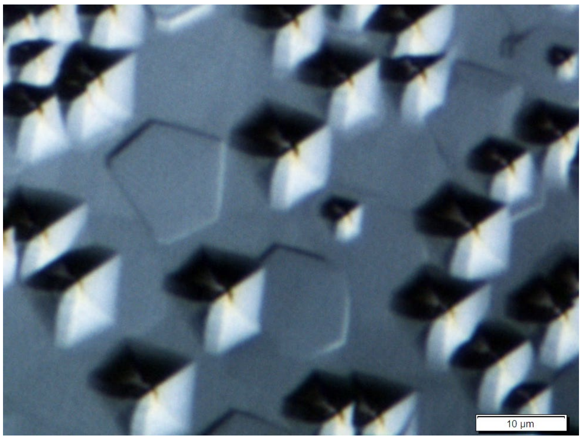

Fig. 7.5: Etch pits of HNO_3 etched ion tracks. : 0.091 % HNO_3, 2 s, 15 °C, (1×10^6 ions/cm^2, 11.1 MeV/u, ^{197}Au)

tic acid needs about 20 s to produce etch pits of the same size (Fig. 7.1).

Concerning the areal density, there are no differences between the two etching solutions. Both etching solutions are able to etch all tracks induced by irradiation with swift heavy ions (Fig. 7.6). The maximum etching time is limited to 6 - 8 s for HNO_3 and to 20 s for EDTA + acetic acid. Exceeding these times lead to overlapping etch pits which cannot be analyzed in a satisfactory manner.

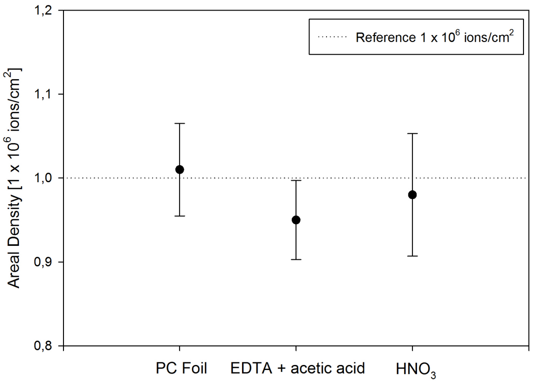

Fig. 7.6: Comparison of the areal density of the etch pits. Both HNO_3 and EDTA + acetic acid show within error the same areal density as the reference PC foil.

7.2 ADVANTAGES OF THE ETCHING SOLUTIONS

7.2.1 HNO_3

- HNO_3 is well known in thermochronologic laboratories all around the world and therefore accepted as an etchant, and the users are experienced in handling the acid
- The required concentration of 0.091 % HNO_3 is very easy to produce from standard products, for example 65 % HNO_3
- No special etching tool is required
- HNO_3 works very reliably on cleaved and embedded calcite crystals
- Short etching times
- Bigger etched ion tracks leading to further applications (see Chapter 9.4)
- The etching solution is very safe to handle due to minimal concentrations

7.2.2 EDTA + acetic acid

- Due to the slower etching speed of EDTA + acetic acid and a resulting etching time of 20 s no special etching tools are required and the timing error is not very big.
- For some applications the pseudohexagonal shape might be of advantage

In conclusion, HNO_3 is a very interesting etching option for etching heavy ion tracks in calcite crystals, because more of the specified requirements are met than with EDTA + 5 % acetic acid and the solution is easier to produce.

7.3 COMPARISON WITH LITERATURE

7.3.1 VIKTOR VON EBNER (1885)

Of all of the literature found, some of it very old, the work of Viktor von Ebner from 1885 is the most impressive, and will be described in detail as an example. He wanted to find out whether the “etch figures” revealed by etching calcite are related to the crystal structure, and if the etch figures are a function of the crystal planes.

He exhaustively described the effect of eight different etching solutions (formic acid, acetic acid, picric acid, nitric acid, hydrochloric acid, phosphoric acid, sulphuric acid and chromic acid), different concentrations, different temperatures, and even different etching techniques on the shape of the etch pits he revealed by etching calcite and aragonite. He made several drawings of every kind of etch pit he observed.

Despite the different aims of von Ebner and this work, when comparing the drawings of von Ebner with the result of this study, many similarities can be found, although he used different concentrations and times. Figure 7.7 shows 4 examples of drawings by von Ebner which match etch figures observed during the etching experiments of Chapters 5 and 6. Unfortunately, von Ebner did not put a scale to his drawings. He only gives information about the magnification he used when observing the etch pits. Therefore it is not possible to compare the size of the etch pits, but only their shape. The size of von Ebner's etch pits is highly speculative, but due to the concentrations and times he used, it must be assumed that his etch pits were many times bigger than the etch pits observed in this study. Nevertheless, they look very similar. Presumably, von Ebner etched natural dislocations existing in the calcite, and not ion tracks as in this study, but these dislocations basically show the same etching behavior and shapes as the ion tracks (see Chapter 9.1).

The table of drawings in Figure 7.7 shows etching experiments with acetic acid in the first row (Figs. 16-20), picric acid (Fig. 29) and nitric acid in the lower row (Fig. 30- 36).

Image a) shows etched ion tracks etched with EDTA + 5 % acetic acid. The pseudohexagonal shape is very similar to the etch figures von Ebner revealed with chilled acetic acid. Image b), in combination with Figure 26a and Figure 27 is very interesting. During the etching process of image b) with EDTA + 5 % acetic acid some dirt remained on the crystal due to an incomplete cleaning. This dirt causes the “frayed” geometry of the etch pits. Von Ebner saw similar structures on his samples and drew the structures resulting from the used etching solution, but it is very likely that he had the same dirt issues, without realizing the real reason for the shape of his etch figures. Image c) shows etch pits from induced fission tracks on a sawed and polished sample. Image d) shows etch pits from induced swift heavy ion tracks on a cleaved sample. The etch pits on c) are more rounded than the etch pits on d); this is due to the lower energy and worse quality of the surface. The etch pits on d) show a clear pseudopentagonal geometry. Von Ebner observed both types: the rounded etch figure in Figure 32 etched with 10 % HNO_3 and the type with the sharp geometry in Figure 33, etched with 5 % HNO_3. It is not known whether he realized how great the influence of the sample surface quality is on the etch result, because he explains every different etch figure in terms of the concentration used, but basically his observations and conclusions are correct: different etching solutions reveal different shapes. It was very interesting to compare the results of this study with results obtained 130 years ago, because they are so similar. Beyond this few examples, a matching drawing by von Ebner could be found for almost every etch figure found among my samples.

7.3.2 Sippel & Glover (1964)

The results of Sippel & Glover were partly confirmed and partly not reproducible. Confirmed statements are: Different etching solutions produce different shapes of etch pits, the annealing behavior of induced ion tracks and dislocations is very similar, and fission damage induced by an external uranium source can be visualized. One result of Sippel & Glover that could not be reproduced is their etching solution. The etch pits they revealed in Fig. 2.2 are not realistic. In all etching experiments with their etching solution, the etch pits became much bigger than the etch pits they observed. The reasons for this are not known. All in all, the work of Sippel & Glover provides a good feasibility analysis for the use of calcite for fission-track dating.

7.3.3 Macdougall & Price (1974)

The publication by Macdougall & Price, on the other hand, presents more questionable results. A first wrong statement is that calcite they used, does not accumulate a sufficient amount of uranium. Various studies have disproved this statement. Additionally, they state, that tracks in calcite anneal at ambient temperatures. This statement could not be confirmed. Another questionable result in Macdougall & Price concerns the images they present in their publication. An image showing “etch pits in calcite” clearly shows etched fission tracks in apatite or mica, and not in calcite (Figure 2.3). Over the whole of this study, nothing similar to the image published could be produced. Nevertheless, the etching recipes by Macdougall & Price are reasonable, hence one of their etching solutions is one of the two standard etching recipes used in this study.

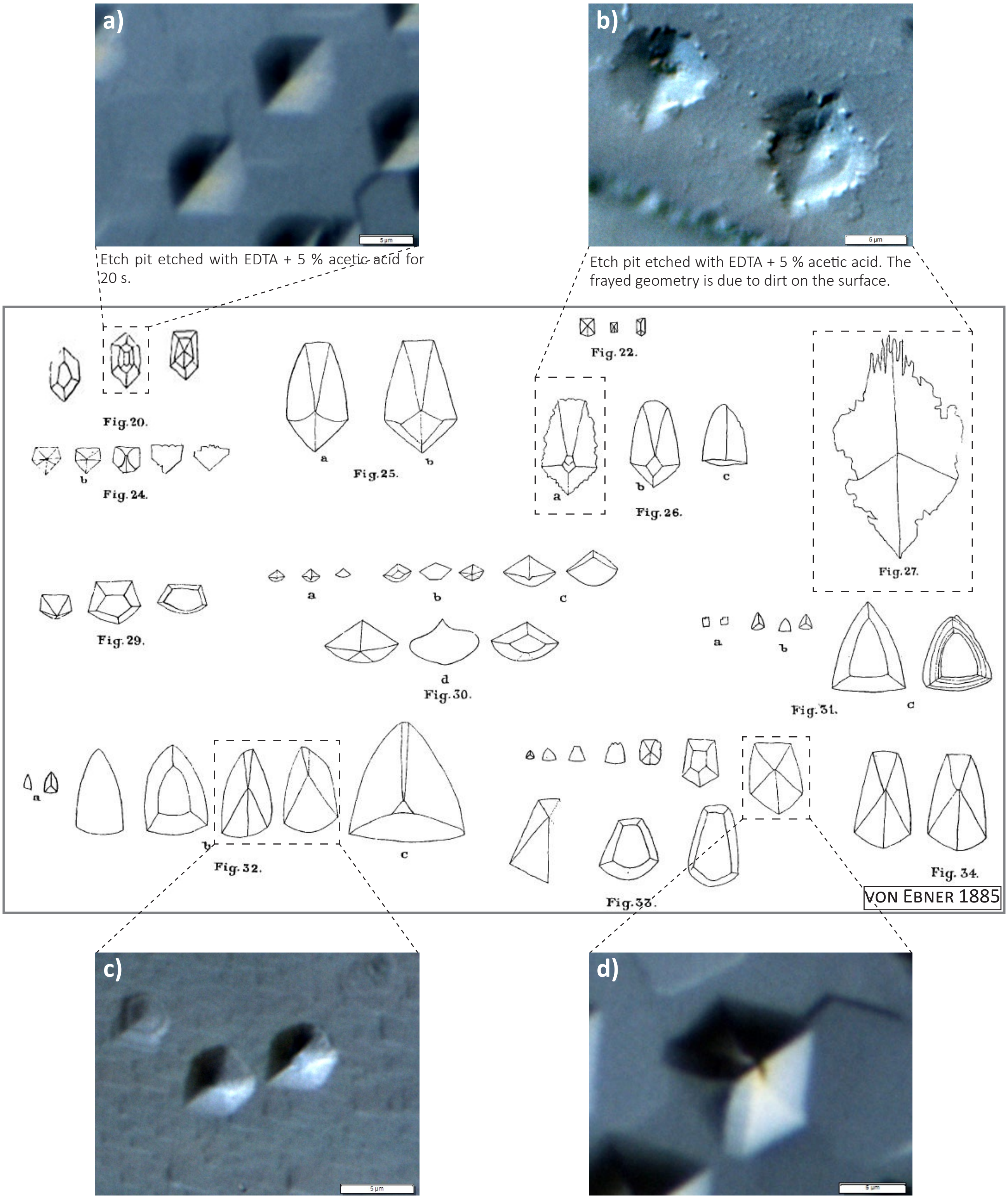

Etch pit etched with EDTA + 5 % acetic acid for 20 s.

Etch pit etched with EDTA + 5 % acetic acid. The frayed geometry is due to dirt on the surface.

Etch pits from induced fission tracks of Chapter 8. The etch pits are rounded

Etch pit etched with 0.091 % HNO_3

Fig. 7.7: This figure shows a comparison of the etch figures of calcite described and drawn by von Ebner 1885 (in the middle of the figure) with images of etch pits acquired during this study. Generally, the similarity is astonishing. A) shows etch pits revealed with EDTA + 5 % acetic acid whereas von Ebner etched with iced acetic acid. B) shows etch pits of EDTA + 5 % acetic acid. The frayed geometry of the etch pits develops due to dirt on the surface of the crystal during the etching process. It can be assumed that von Ebner, who etched with 9 % iced vinegar (Fig. 26) and 50 % acetic acid (Fig. 27) had the same problems without realising the reasons for this effect. The images c) and d) show etch pits revealed with 0.91 % HNO_3, of which the etch pits in c) are a bit more rounded. Von Ebner described the same geometries during his experiments with HNO_3, 10 % for Figure 32 and 5 % for Figure 33. (All irradiations: 1×10^6 ions/cm^2, 11.1 MeV/u, ^{197}Au)

8

VISUALIZATION OF NEUTRON INDUCED FISSION TRACKS

CONTENTS

8.1 INTRODUCTION

After establishing two new methods of visualizing high energy swift heavy ion tracks in calcite crystals with etching techniques (Chapters 5 + 6) this chapter is about the applicability of these methods to visualize induced fission tracks in calcite crystals. As source of the fission fragments a CN-5 uranium glass and zircon grains were used.

8.2 METHODOLOGY

8.2.1 Materials used

For Experiment 1, a CN-5 glass was used as a uranium source. CN-5 glasses are the standard material used in fission-track laboratories to check the amount of neutrons applied to samples during irradiation. The CN-5 glasses used have a uranium content of 12.17 (± 0.62) ppm (BELLEMANS et. al. 1995)

For Experiment 2 with a natural uranium source, zircon crystals from a titanium mine in Paraíba, Brazil were used.

8.2.2 Irradiation

All samples were irradiated with thermal neutrons at the FRM II research reactor in Munich. The sample of Experiment 1 (8.3.1) was irradiated with a fluence of 1×10^{16} neutrons/cm^2 which is standard fluence for apatite irradiation, whereas the sample of Experiment 2 was irradiated with a fluence of 1×10^{15} neutrons/cm^2; the standard zircon irradiation.

8.2.3 Etching procedure

To visualize the induced fission tracks, all irradiated calcite crystals in this study were etched with a 0.091 % HNO_3 etching solution at a temperature of 15 °C for 2 (± 0.25) s. The short etching time of only 2 s was chosen to ensure that the sample would not get damaged by strong etching. After the etching process, the samples were cleaned with ethanol and purified water.

8.2.4 Visualization

The etched specimens were carefully analyzed to describe changes in surface morphology, optical & geometrical characteristics and material properties. For this purpose, a reflected light Olympus BX-50 microscope with attached Nomarski Differential Interference Contrast (DIC) and high resolution camera combined with Stream™ image analyzing software were used for optical analysis and statistical examination.

8.2.5 First experiences

As a first test, several carbonate rocks were prepared for irradiation. These rocks were:

- Calcite with Lepidocrocite from the uranium ore deposit Schlema-Alberoda, Germany
- Red carbonatite from Fuerteventura
- Black carbonatite from Fuerteventura
- Sovite (grained carbonatite) from the “Ohrberg” at Schelingen, Kaiserstuhl, Germany
- Carbonatite from Jacupiranga, Brazil

Fig. 8.1: Sovite rock from the “Ohrberg”, Kaiserstuhl, Germany used for the test experiment.

Tab. 8-1: SRIM calculation of an uranium ion in $CaCO_3$ at energies of 80 and 90 MeV. The calculation was made to estimate the projected range of the uranium daughter ions, using uranium as best case scenario.

Ion Energy [GeV]	dE/dx Elec.[keV/µm]	dE/dx Nuclear [keV/µm]	Projected Range [µm]
80,00	1,355E+04	5,194E+02	9,62
90,00	1,484E+04	4,758E+02	10,30

The prepared carbonatites were combined with mica into batches (Fig. 8.2) which were irradiated with thermal neutrons at the FRM II, Munich with a fluence of 1×10^{15} neutrons/cm^2.

The experiment of irradiating carbonatite revealed - especially for the Kaiserstuhl Sovite (Fig. 8.1) - interesting, but disappointing results. Embedded zircon grains in the carbonatite matrix caused massive fission-track accumulations on the muscovite. So the conclusion was that around the zircons, some natural fission tracks should be apparent in the surrounding calcite. But additional etching did not provide sufficient results. Recalculation of the projected range of the fission tracks explained why: fission fragments of ^{235}U caused by thermal neutron irradiation have an energy of about 80, respectively about 90 MeV and therefore a projected range of only 10 µm max. (Tab. 8-1). This explains the lack of fission tracks in the calcite: they do not have a sufficient range to penetrate the surrounding calcite far enough to be visualized on the surface (Fig. 8.2, green circle). Only few fission fragments might have reached the mica through the calcite, but these tracks were very short and most likely these tracks have been etched away through the bulk etching. Despite an intensive search, no etch pits were found on the calcite on the border to the zircon grain.

The energy of the fission fragments is also the reason for the sharp display of the zircon's shape on the mica (Fig. 8.3). Only tracks which are generated directly below the polished surface of the zircon were able to reach the mica. Everything deeper got stuck in the calcite.

A new experimental setup had to be applied to penetrate the calcite directly in such a way that there would be etchable tracks, and also to check the ability of calcite to function as a detector for induced fission tracks.

8.3 RESULTS

8.3.1 Experiment 1: Calcite with CN-5 uranium glass

As a first experiment, the mica as detector for the fission tracks was eliminated and CN-5 uranium glass was mounted directly on the polished calcite crystal to provide a direct penetration of the calcite crystal by fission fragments out of the

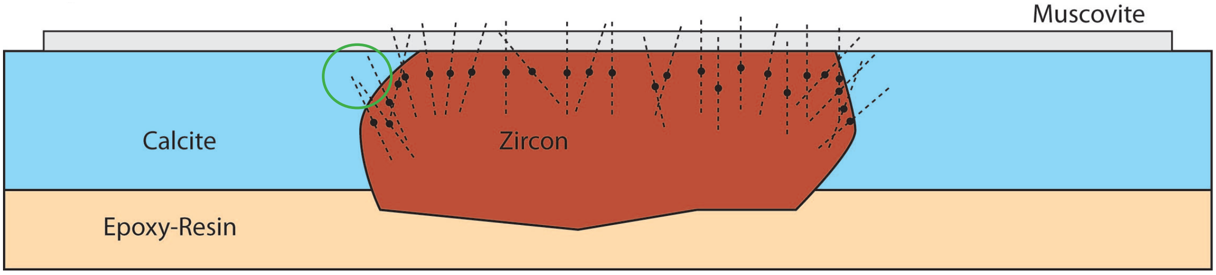

Fig. 8.2: Setup of the first, unsuccessful experiments

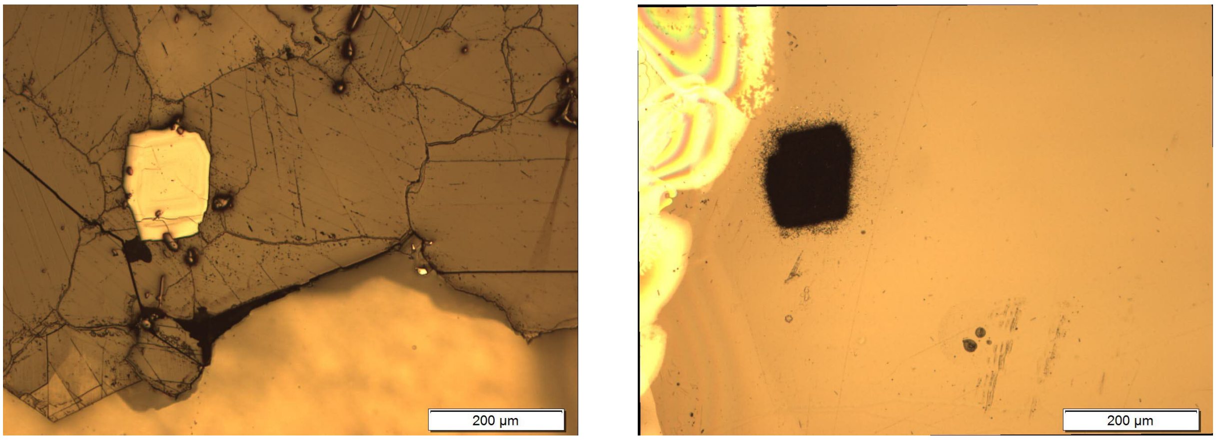

Fig. 8.3: Image of the zircon grain in the carbonatite on the left, and the related position on the mica (right)

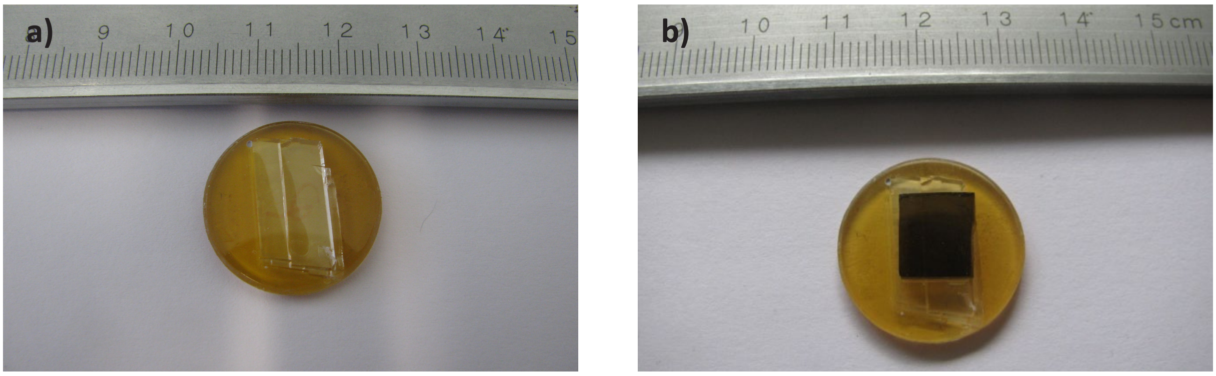

Fig. 8.4: The irradiated batch without uranium glass (a) and with the attached uranium glass (b)

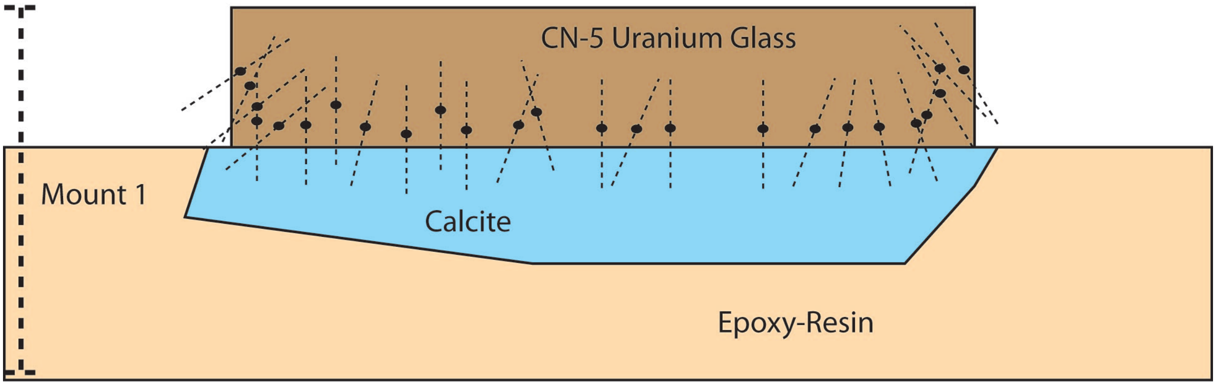

Fig. 8.5: Experimental setup of Experiment 1: A calcite crystal as detector for fission fragments from a CN-5 uranium glass.

uranium glass (Fig. 8.4 + Fig. 8.5). This setup allows testing of the detector abilities of calcite with a definite amount of uranium and therefore a predictable areal density of induced fission tracks in the calcite. A comparison of the areal density of induced fission tracks on the surfaces gives an indication of whether all fission tracks are displayed on the calcite, provided that single tracks can be visualized. In their publication Sippel & Glover used a similar method to produce artificial tracks on their calcite crystal. Instead of uranium glass, they placed a U_2O_8 film on top of the crystal to produce fission tracks.

After the irradiation with thermal neutrons and the etching (HNO_3) procedure, etch pits were revealed on the calcite surface. These etch pits have a pseudopentagonal shape like the etch pits of swift heavy ion irradiated crystals, etched using the same procedure. The etch pits from induced fission tracks are a bit more rounded than the swift heavy ion irradiated etch pits, but the general appearance is very similar (Fig. 8.7). Surprisingly, the etch pits all are orientated in the same direction. One would expect a randomized orientation of the etch pits due to the randomized irradiation angle and irradiation direction caused by the fission fragments of the CN-5 glass. This aspect will be discussed in Chapter 8.3.4 in detail.

Comparing the size of the etch pits, the ion irradiated etch pits have a mean length of 5.2 µm (± 1.7), after 2 s of etching, the etch pits of the CN-5 glass induced tracks, at 4.7 µm (± 0.3). are a bit smaller after two seconds of etching than the swift heavy ion-induced etch pits

The fission fragments formed the most etch pits on the calcite where the glass was lying directly on the calcite crystal. The border of the areas with direct contact to the uranium glass on the crystal is clearly visible (Fig. 8.6).

The areal density of the etch pits beyond the uranium glass - border decreases continuously, but even on the outermost parts of the crystal are some etch pits. This means that the fission products are able to travel quite long distances through the air before their impact on the surface of the calcite crystal. Counting the areal

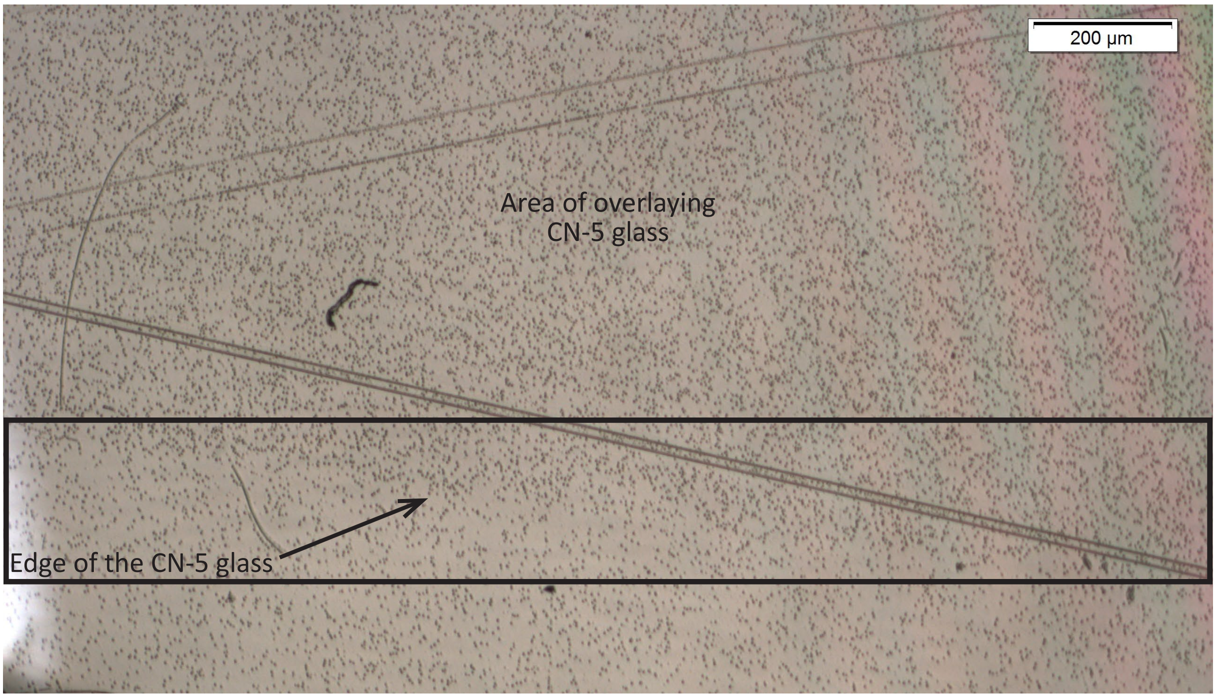

Fig. 8.6: The border of the uranium glass on the calcite crystal. Visible from the top left to the bottom right of the black box.

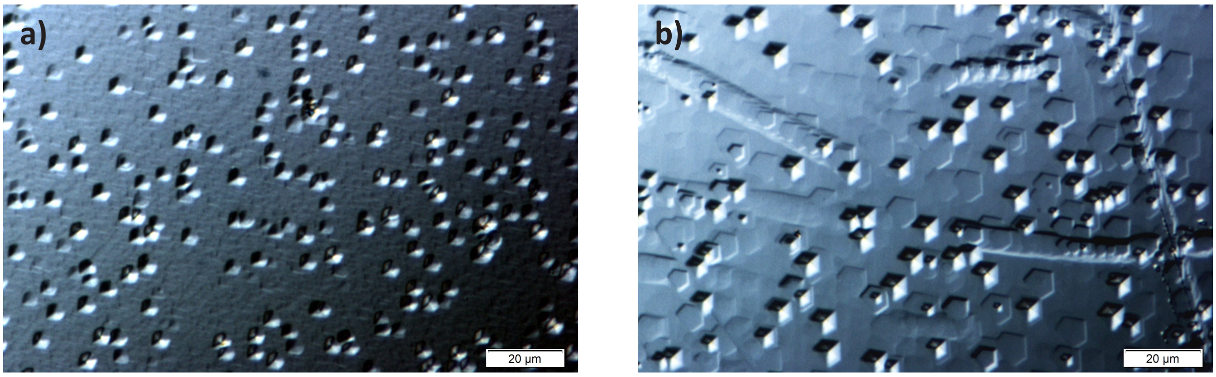

Fig. 8.7: Etch pits after 2 s of etching with 0.091 % HNO_3. The image on the left (a) shows etch pits from fission fragments of Experiment 1, the image on the right (b) shows etch pits of a crystal irradiated with swift heavy ions. The etch pits on the left are slightly smaller and geometrically not so well defined as the etch pits on the right

density of the etch pits in the calcite under the uranium glass gives a value of 1.36 x 10^6 etch pits/cm^2 (± 0.1). The counted value matches the average areal density of mica on CN-5 glass irradiated at FRM II with a fluence of 1×10^{16} neutrons/cm^2 within error. This means that calcite as detector is sensitive enough to display all fission tracks induced by the CN-5 glass during irradiation.

8.3.2 Experiment 2: Calcite with Zircon

For the second experiment calcite and zircon mounts were prepared in the same way as for the previous experiment (Fig. 8.8) and the calcite mount was placed in direct contact with the zircon mount on top of the latter, so that the polished surfaces were facing each other (Fig. 8.9). These packages were irradiated with thermal neutrons like the packages from Experiment 1.

This setup was intended to test the ability of calcite to display fission tracks on a completely natural basis with no artificial components like the uranium glass used. All zircon grains used had a different amount of uranium, so many different areal densities were expected for the single grains (Fig. 8.8).

The results show that calcite is a very sensitive material for detecting induced fission tracks. The zircon grains can be identified very easily even

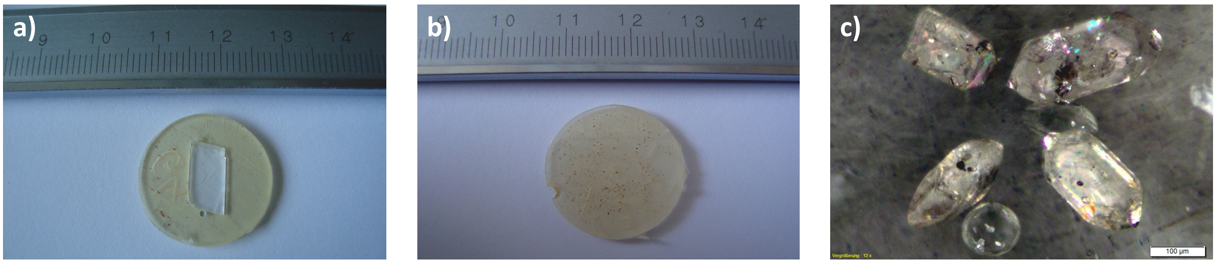

Fig. 8.8: a) Mount with embedded calcite. b) Mount with embedded zircon grains. c) Zircon grains

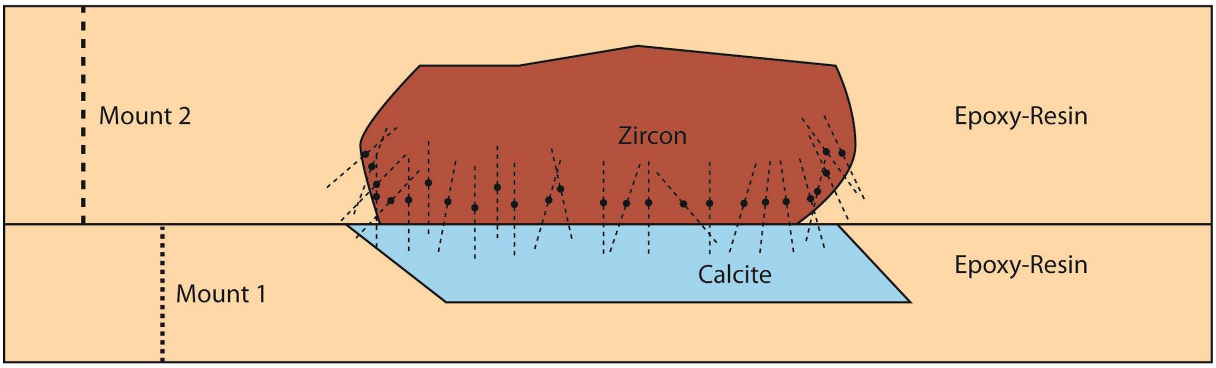

Fig. 8.9: Experimental setup of Experiment 2: A mount with zircon grains function as source for fission fragments.

the different areal density of the zircon grains can be seen at first sight. Some grains have a zonal structure with different amounts of uranium in the different zones. Even this zonal structure is visible on the calcite. Figure 8.11 shows some examples of etch pits from induced fission tracks on the calcite. The etch pits themselves look very similar to the etch pits in Experiment 1, but with a length of 2.06 µm (± 0.18) and a width of 1.77 µm (± 0.16) they are even a bit smaller than the etch pits from Experiment 1 (Fig. 8.12).

8.3.3 Comparison between ion irradiation, Experiment 1 and Experiment 2

The biggest difference between the etch pits obtained in the three experiments performed is the size of the etch pits after two seconds of etching with HNO_3 (Fig. 8.10). The biggest etch pits are caused by ion implantation, the next smaller ones are from implantation with an artificial source of fission fragments, the uranium bearing CN-5 glass. The smallest etch pits are caused by fission tracks originating from fission fragments from the zircon grains placed on top of the calcite. The shape of the etch pits is more or less the same for all three irradiation methods.

8.3.4 Irradiation with angle

8.3.4.1 Introduction

From the very beginning of the etching experiments, the question of the influence of the penetration angle of the ions on the appearance and properties of the etch pits was raised. It is a very likely assumption that the etch pits show some reaction to a different angle, because calcite reacts very strongly to different etching solutions. All irradiations of the calcite crystals with swift heavy ions at the UNILAC so far were perpendicular to the crystal's surface, so no effects (if they

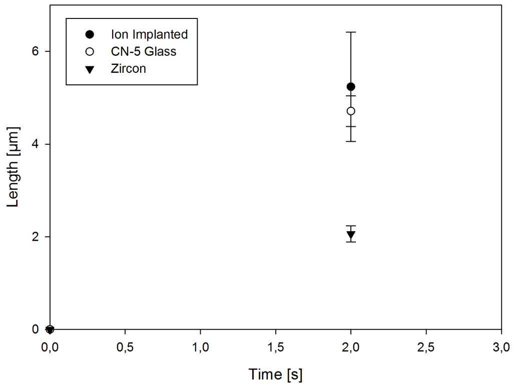

Fig. 8.10: Comparison of the length of the etch pits (ion-induced, CN-5 glass, zircon grain) after 2 s of etching with 0.091 % HNO_3.

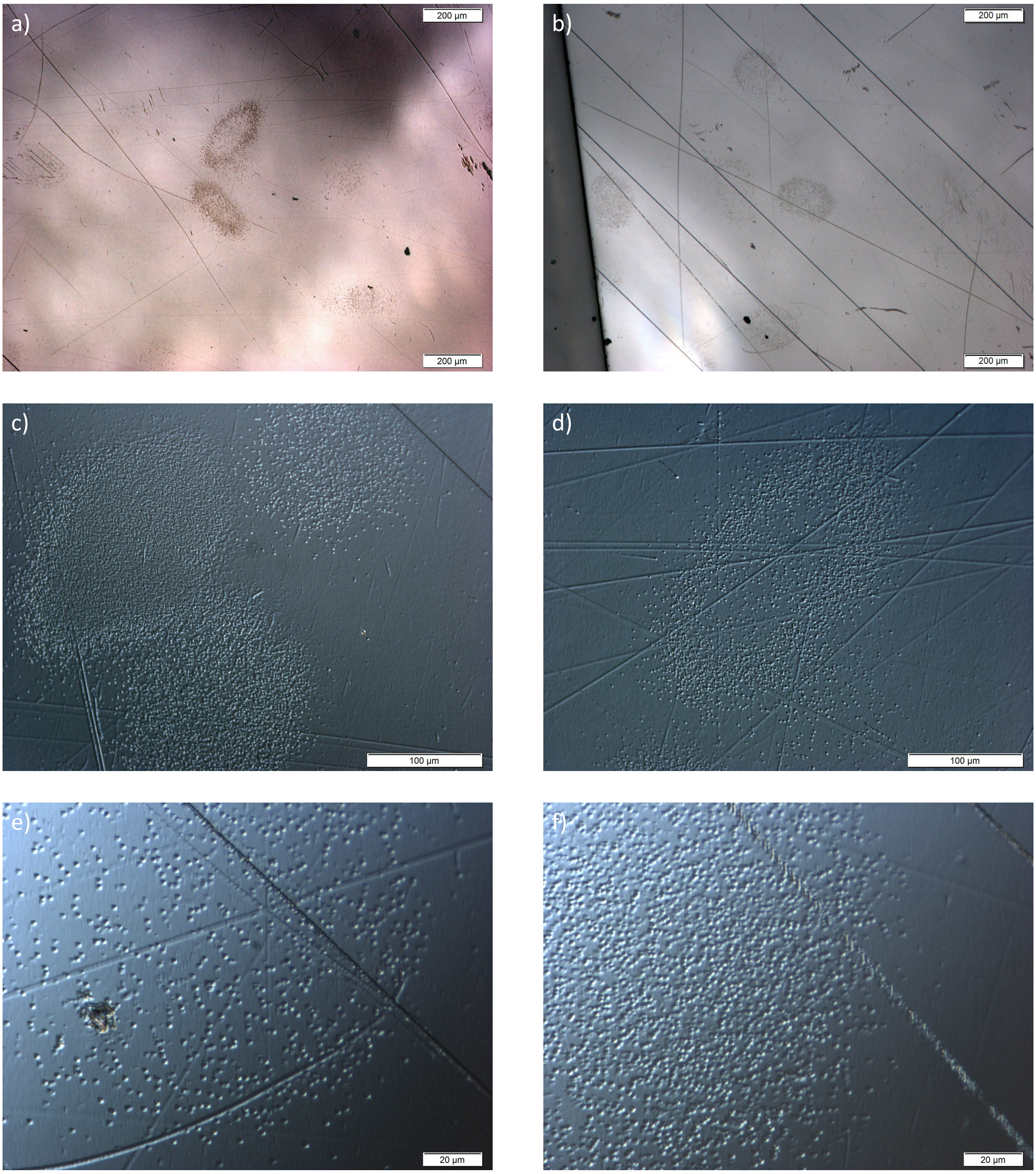

Fig. 8.11: Etch pits of fission tracks induced by excitation of uranium bearing zircon grains with thermal neutrons after 2 s of etching with 0.091 % HNO_3. a) + b) show images with 5x magnifications where the fission tracks of the individual zircon grains are clearly visible. c) + d) show images with 20x magnifications. c) shows the fission tracks of three grains with different areal density, d) shows the fission tracks of one zircon crystal. The areal density within the fission tracks of this crystal is distributed unevenly. e) + f) show images with 50x magnifications where the different areal density of the fission tracks of the zircon grains is visible.

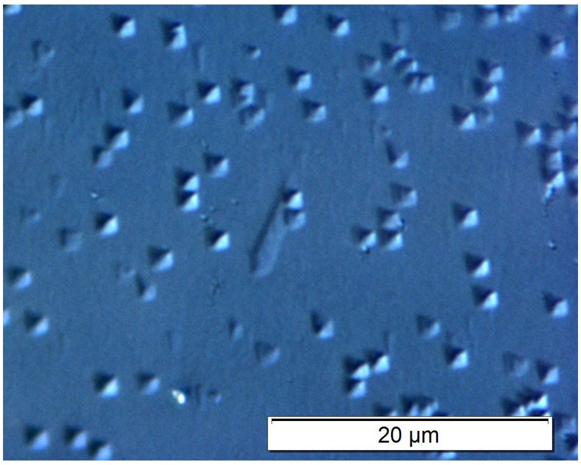

Fig. 8.12: Etch pits induced by zircon after 2 s of etching. The etch pits have a pentagonal shape.

exist) could be detected. Thus new ways to determine possible effects were researched.

8.3.4.2 Natural, not definable angles

The Uranium Glass Experiment provided a first opportunity to investigate the influence of the penetration angle. Etch pits on the calcite crystal which are situated outside the area of the overlying uranium glass proved that the products of natural fissioning, stimulated by irradiation with thermal neutrons, travel distances of up to 1 cm through the air before they strike the crystal's surface and form an ion track. This leads to the following conclusion: the stimulated fission products emitted from the outer region of the uranium glass must strike the surface of the calcite crystal at a sharp angle, otherwise they would not be able to hit the calcite crystal at all.

To analyze the shape and size of the etch pits, three areas have been defined: Area 1 includes the sector of the calcite crystal underneath the uranium glass, Area 2 includes the sector between the edge of the uranium glass and the edge of the calcite crystal and Area 3 is located at the edge of the crystal. Images were taken in all three areas and the etch pits located in the different areas have been analyzed carefully. The model in Figure 8.13 illustrates 4 possible scenarios:

a) The stimulated fission products leaving the uranium glass strike the calcite crystal more or less perpendicularly. This should be the case for the most of the fission products out of the uranium glass in the overlaying area. Figure 8.14 shows etch pits of Area 1 of the calcite crystal.

b) But it is not excluded, that some fission products out of the uranium glass hit the calcite at a sharp angle.

c) Area 2 etch pits, beyond the borders of the uranium glass, originate from fission products which were travelling through the air for a certain distance and then hit the crystal surface at a sharp angle (Fig. 8.15).

d) Area 3 etch pits develop under the same conditions as the etch pits from c). However, the fission products forming these etch pits travelled an even longer distance through the air and the resulting angle at which they hit the surface is even more oblique (Fig. 8.16).

Evaluation of the images and measurements of the etch pits revealed a pattern in the changing of the size of the etch pits: the length of the

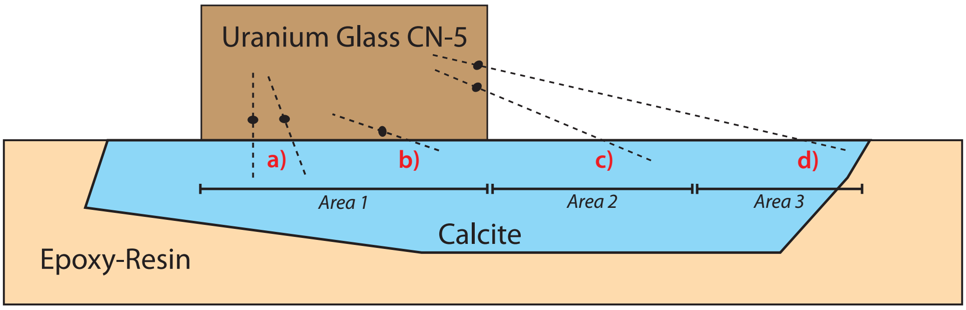

Fig. 8.13: Sketch to illustrate the theory of the different impact angles of the fission products. Area 1 (with cases a and b) provides perpendicular and sharp angles, Area 2 sharp angles and Area 3 even sharper angles. This leads to the simultaneous formation of etch pits with different irradiation angles.

etch pits does not change significantly, but the width of the etch pits gets slightly bigger until the etch pits are wider than they are long in area 3 (Fig. 8.14- Fig. 8.16). To quantify this observation, a length / width ratio without dimensions has been set up. Fig. 8.17 shows a plot of the length / width ratio which decreases almost linearly from 1.1 to 0.88.

This result may represent the desired difference in the shape of the etch pits through irradiation at an angle, but because the angles of the irradiation are only good guesses, this experiment is not completely valid and reproducible and has to be confirmed with etch pits from irradiation with a defined angle.

Furthermore, it is surprising that all etch pits are geometrically orientated in the same direction. Apperantly, the direction and the angle of the penetration does not play a role in the etching direction of the etch pit, dictated by the crystal lattice. Another observation supports the theory of fission products travelling through the air before they hit the surface: the areal density of etch pits constantly decreases from area 1 to area 3, which was expected. To estimate the distance fission fragments can cover, a SRIM calculation for Xenon-ions in air has been performed. According to SRIM, Xe-ins with an energy of 100 MeV have a projected range of 17.35 mm in air. Only a few fission products have the appropriate angle and enough energy to travel the long distance from the uranium glass all the way to the edge of the crystal.

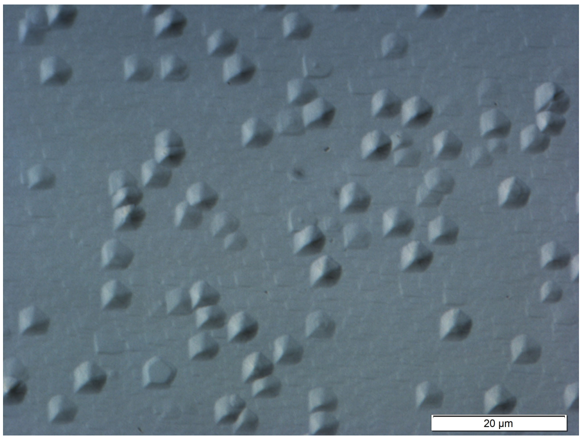

Fig. 8.14: Etch pits formed directly under the uranium glass (Area 1). Different angles are possible.

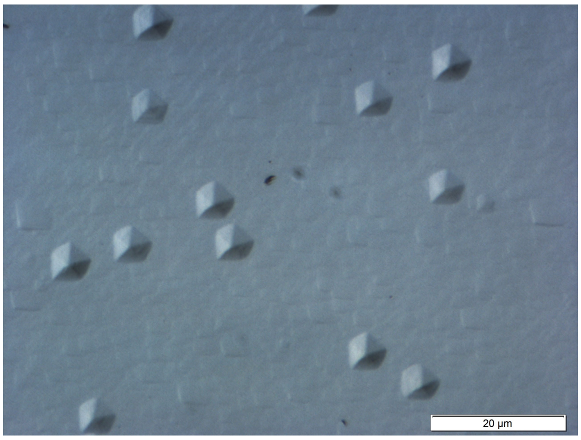

Fig. 8.15: Etch pits formed between the uranium glass and the edge of the crystal (Area 2). Sharp irradiation angles of 20°-30° can be assumed

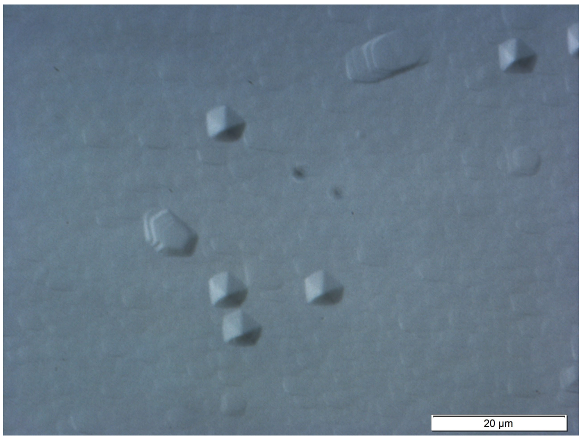

Fig. 8.16: Etch pits formed at the edge of the crystal (Area 3). Sharp irradiation angles can be assumed.

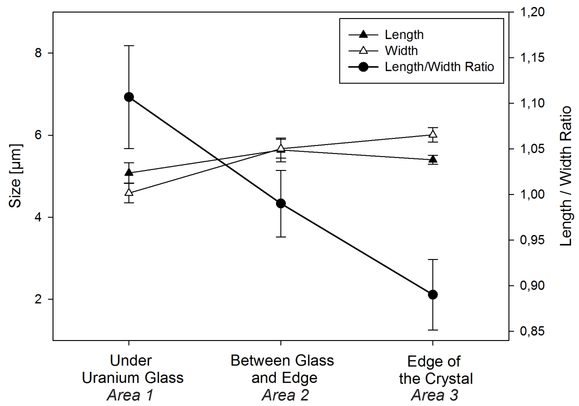

Fig. 8.17: Length / width ratio of the etch pits from Area 1 to Area 3. The ratio gets smaller with increasing distance from the uranium glass.

8.3.4.3 Defined angles through swift heavy ion irradiation at an angle

To get etch pits from swift heavy ions irradiated at a defined angle, two sample holders were prepared with cleaved calcite crystals and then irradiated (1×10^6 ions/cm^2, Au) at the UNILAC, GSI with 15° and 45° out of the vertical line, giving angles of 90°, 75° and 45° relative to the crystal surface (Fig. 8.18). After irradiation, the crystals were etched with 0.091 % HNO_3 for 4 (± 0.25) seconds, and then compared with a crystal which had been irradiated perpendicularly to the surface and etched under the same conditions.

The results from this experiment are clear: there is no difference at all between the etch pits formed by irradiation at 90°, 75° and 45°. The images Fig. 8.19 - Fig. 8.21 clearly show that there is no difference in the length / width ratio which was discovered at the crystal from the uranium glass experiment. The etch pits from the different angles may have some slight differences, but these are due to dirt on the surface or minimally different etching conditions. These influences, dirt on the surface in particular, have a much greater influence on the shape of the etch pits than the irradiation angle. Why the etch pits in the first experiments showed some even measurable differences and why the etch pits have different shapes is not known. Maybe the fact that the irradiation and the etching took place at the same time for all angles plays a role. In contrast the UNILAC samples, although all parameters were the same, were prepared in three different irradiations and three different etching processes. This may account for one experiment having shown differences and the other not.

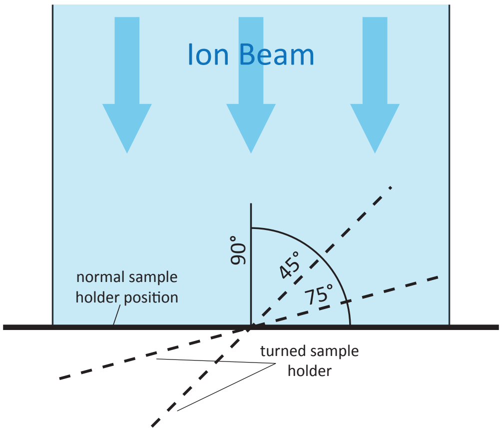

Fig. 8.18: Etch pits formed at the edge of the crystal (Area 3). Sharp irradiation angles can be assumed.

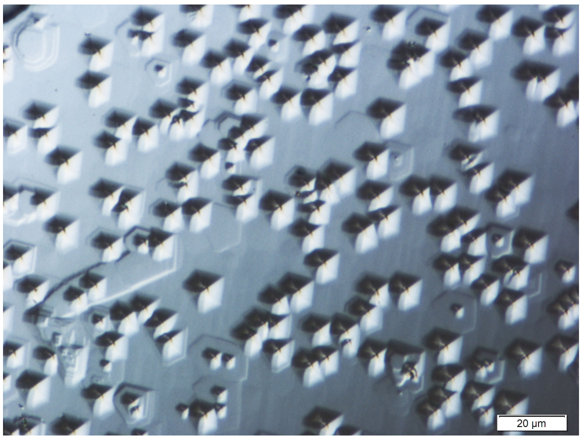

Fig. 8.19: Calcite crystal, irradiated perpendicularly to the surface

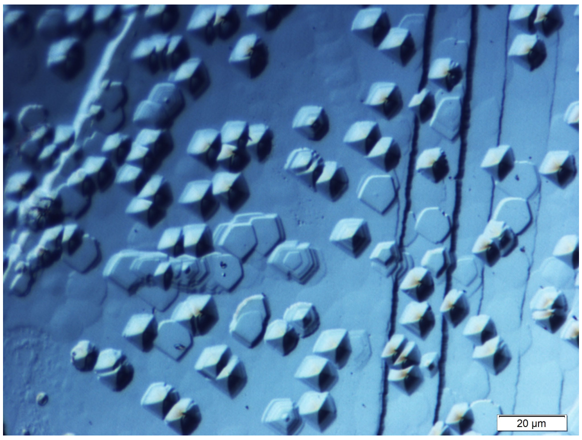

Fig. 8.20: Calcite crystal, irradiated at an angle of 75° to the surface.

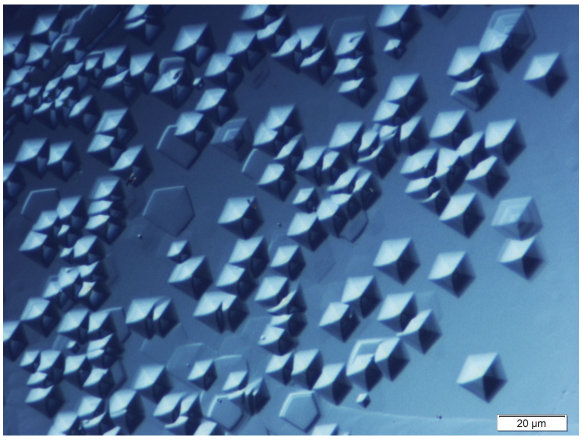

Fig. 8.21: Calcite crystal, irradiated at an angle of 45° to the surface.

8.4 DISCUSSION

The collected data from these two experiments, associated with the results of the experiments with ion implantation, allow several conclusions:

1. The sample preparation process for calcite crystals developed as part of this doctoral thesis works, and is suitable for experiments both with ion-induced etch pits on calcite crystals and etch pits caused by induced fission tracks.
2. It is possible to visualize tracks of fission fragments with energies around 100 MeV on calcite as a detector.
3. The shape of the etch pits of the uranium glass- calcite experiment does not differ from the shape of the etch pits revealed through etching after irradiation with swift heavy ions when etched with the same etching agent.
4. The etching agent plays the major role in questions regarding the shape of the etch pits. The energy of the fission products or ions is not so important.
5. Calcite is a very sensitive detector for ions or fission products which shows all induced fission tracks, if prepared properly.
6. The kind of track-implantation determines the growing speed and therefore the overall size of the etch pits.

Furthermore, it can be stated that the irradiation angle at which fission products or swift heavy ions strike the surface of the crystal does not really affect the shape or other properties of the etch pits. If there are differences, they cannot be quantified. Results from the uranium glass experiment may suggest a quantifiable difference, in a single experiment on the same crystal with the same etchant, but the angles applied to the fission products were not known. Therefore this experiment and measurements are not reproducible and resilient. Attempts to apply the results from the uranium glass experiment to etch pits irradiated at an angle (75° and 45°) failed. The etch pits showed no differences. Recapitulation of the experiment shows that the irradiation angles of the uranium glass experiment are quite sharp, presumably between 25° and 10°. Maybe the angles of 75° and 45° are not sharp enough to achieve the same effect. Another possible explanation is the big difference between the irradiation energies of the samples. Maybe only etch pits originating from irradiation with low energies, like fission products, show the angle effects, and the high energies applied at GSI overlie those differences between the etch pits

8.5 OUTLOOK

As an outlook, many different calcite crystals have to be tested for their uranium content and for their usability for fission-track dating.

9

MISCELLANEOUS RESULTS

CONTENTS

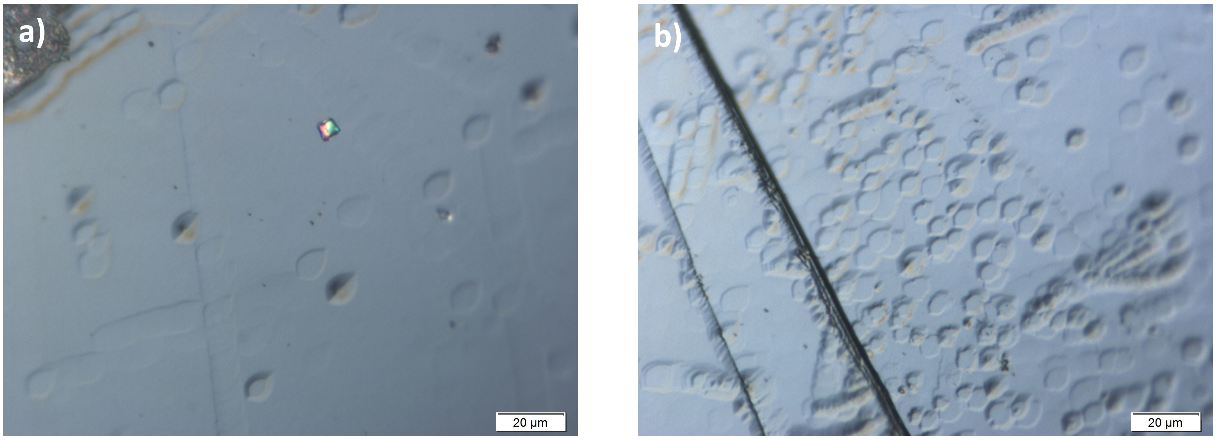

Fig. 9.1: a) Plane crystal lattice, with almost no dislocations. b) Dislocations gather around cracks or scratches on the crystal surface.

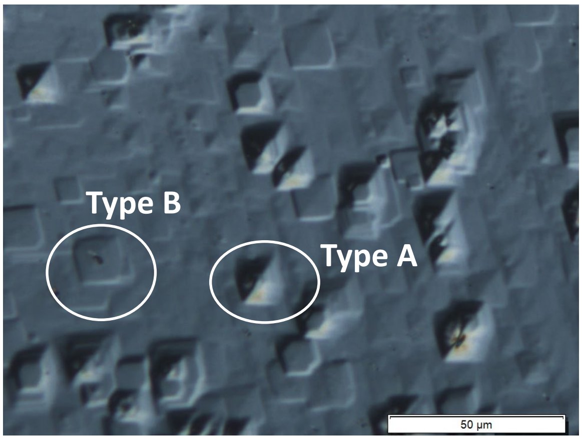

Fig. 9.2: Two types of dislocations.

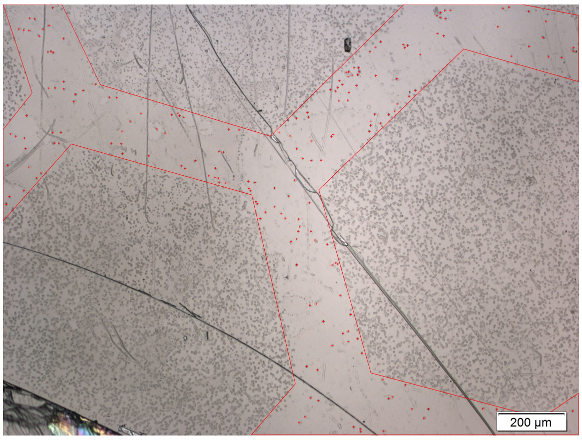

Fig. 9.3: Etched crystal, image with a 5x objective. The red crosses mark Type A dislocations. (1×10^6 ions/cm^2, ^{197}Au)

9.1 Etching Results for non-irradiated Crystals - Dislocations

In order to investigate the behavior of non-irradiated calcites, non-irradiated crystals were etched using standard etching procedures (EDTA + 5 % acetic acid for 20 s). Two different types of etch pits caused by natural defects (designated as Type A and Type B) could be identified: the dislocations.

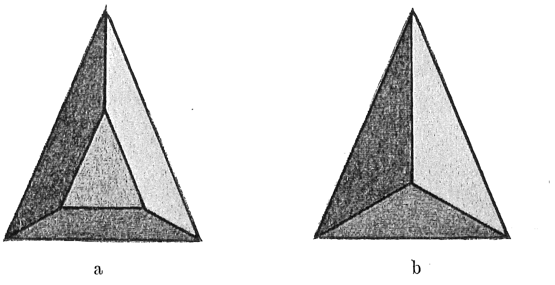

Abb. 2. Ätzgrubentypen (schematisch). a Tafeltyp, b Pyramidentyp.

Fig. 9.4: Two types of dislocations: Table-type (a) and pyramide-type (b)

Dislocations are erratically distributed on the calcite crystals. On plane lattice, dislocations occur in relatively small numbers. Basically they gather around cracks, scratches and other inconstant areas of the calcite surface, where the crystal lattice is deranged (Fig. 9.1). Near scratches, for example, they follow the alignment of the scratch and occur in great numbers. In general, non-irradiated calcite crystals form two different types of etched dislocations (Fig. 9.2). Type A has a very similar shape to etched ion tracks (Type I). They form pseudohexagonal etch pits which are roughly the same size (Fig. 9.5) as ion-induced etch pits, and therefore it is hard to distinguish between etched ion tracks and Type A dislocations.

Type B etch pits differ significantly from Type I, they are shallower and look like flat depressions

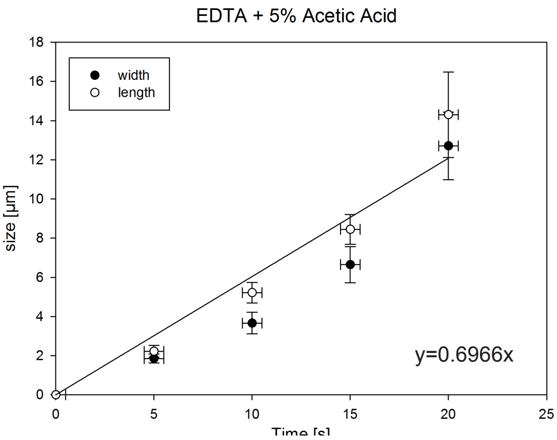

Fig. 9.5: Growth diagram of Type A dislocation size of a non-irradiated crystal

on the crystal surface. This type of dislocations is more common on the calcite surface, they are practically everywhere in different sizes and qualities.

Boos already described these structures in his paper of 1942. He characterized them as "table-type" for the Type B dislocations and as "pyramid-type" for the Type A dislocations (Fig. 9.4).

The next objective for this part of this study was to distinguish between etched ion tracks and dislocations. There are several approaches to solving this problem. One approach uses transmitted light microscopy as a tool. In most cases, Type I etch pits have a tiny hole in the center of the etch pit when viewed with transmitted light, which represents the ion track. The Type A dislocations are sometimes missing the hole of the ion track in the middle of the etch pit, but this observation is not conclusive and does not provide a definite standard to distinguish between these two types,.

Another possible method to distinguish etch pits from dislocations is to observe the arrangement of the etch pits on the crystal. Etched ion tracks are arranged evenly on the surface whereas dislocations are mostly gathered around cracks or scratches or any other deformation of the crystal. Typically, they are lined up along the scratch or crack. Due to the fact that all crystals with etch pits from ion irradiation were covered with a hexagonal mask, identification of etched ion tracks is ensured. This mask helped to get a feeling for "real" etch pits and dislocation.

In summary, the density of Type A and B etch pits increases close to cracks, scratches or any other deformation of the crystal, whereas etch pits from ion tracks are evenly distributed over the entire crystal surface and have a tiny hole in the center.

To recapitulate, at this moment no "fail-safe" method is available to distinguish between Type I etch pits and Type A dislocations. The best method so far is to investigate the distribution and areal density on the sample in order to exclude characteristic patterns and identify them as dislocations.

To determine the areal density of dislocations several kinds of magnification were used. Figure 9.3 shows an image taken with a 5x objective where the hexagonal mask can be seen. The size of the non-irradiated area was measured, and the count of Type A dislocations was interpolated to an area of 1 cm^2. The average areal density of non-irradiated crystals is 0.044 ± 0.02 x 10^6 dislocation/cm^2. For counting, only Type A dislocations were used because these dislocations have the greatest potential for miscounting through confusion with etched ion tracks. This result leads to the conclusion that dislocation does not play a major role in areal density measurements. The amount of dislocation is too small to affect measurements of areal densities.

9.2 Images of the Etch Pits with an Laser Scanning Microscope (LSM)

At the beginning of the etching experiments, attempts to display the etch pits in the best possible way were undertaken. Therefore images with a Laser Scanning Microscope were acquired with the help of Dr. Steffen Greilich from the Center for Cancer Research (DKFZ) in Heidelberg (Fig. 9.6). The images turned out to be quite clear and the etch pits (20 s in EDTA + acetic acid, 1×10^6 ions/cm^2) are clearly visible, but the effort involved in obtaining such pictures is enormous: only specially trained personnel from the DKFZ is allowed to operate the microscope, so it is hard

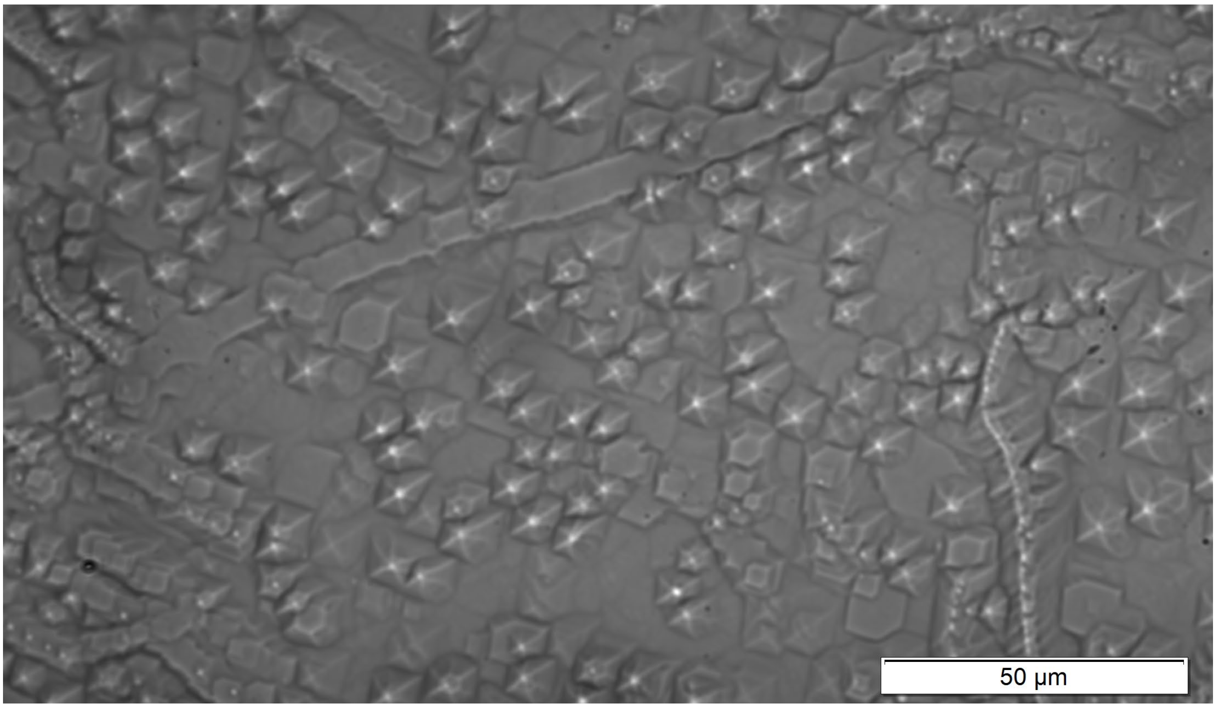

Fig. 9.6: Laser scanning microscope image of etch pits in calcite crystal.

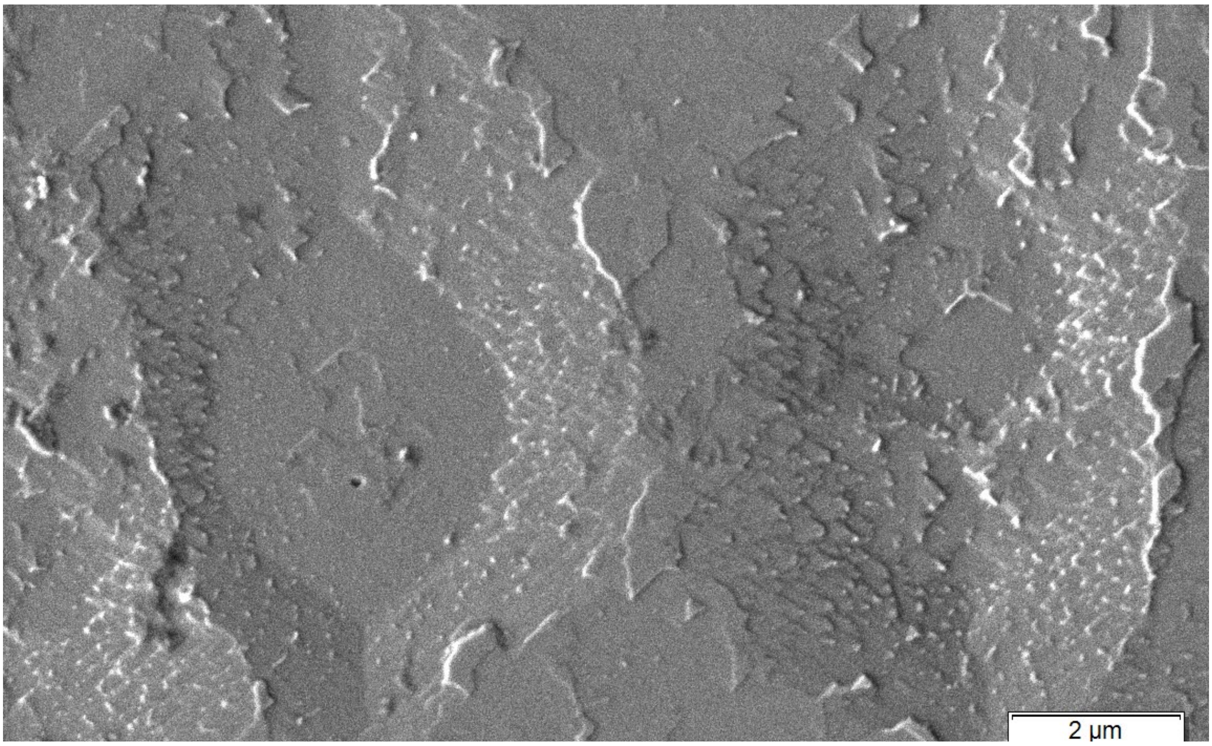

Fig. 9.7: SEM image of etch pits in a calcite crystal. The hole in the middle of the left etch pit is interpreted as the ion track.

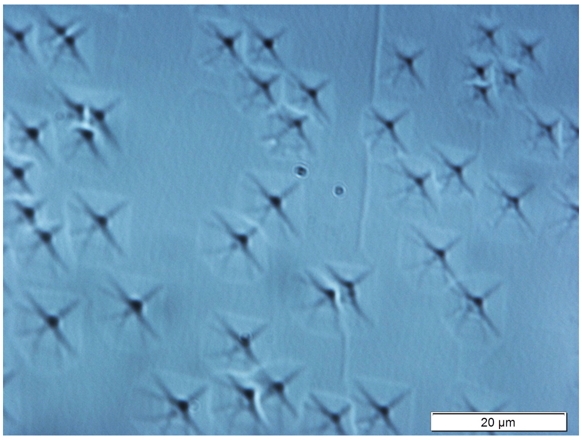

Fig. 9.8: Etch pits of HNO_3 etched ion tracks. Etching Parameters: 0.091 % HNO_3, 2 s, 15 °C.

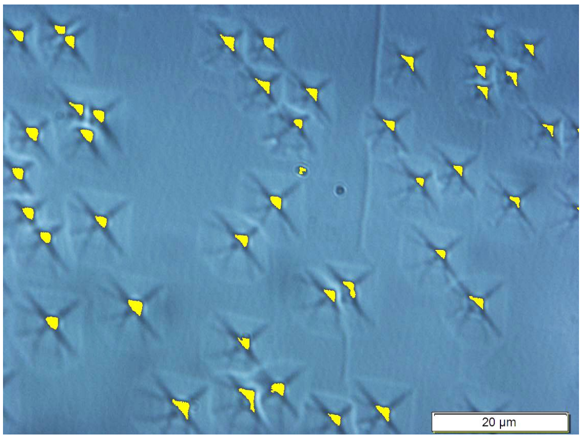

Fig. 9.9: Optical image of HNO_3-etched tracks recorded in transmission mode. The excellent contrast allows automated counting, indicated by the yellow detection marks produced by the analysing software.

to get some working time, and even when on-site it takes a lot of time until first images can be acquired. All in all, the advantage compared to images taken with a standard optical microscope is too small to justify this effort.

9.3 IMAGES OF THE ETCH PITS WITH AN SECONDARY ELECTRON MICROSCOPE (SEM)

Another advanced imaging method applied to the etch pits is secondary electron microscopy. For this, the LEO 440 electron microscope of the Institute for Geoscience was used. A crystal was coated with carbon and then investigated. The image (Fig. 9.7) shows two etch pits (20 s in EDTA + acetic acid, 1×10^6 ions/cm^2) next to each other, of which the left one is better shaped. It has a tiny hole in middle of the pit. This hole is interpreted as the ion track.

9.4 AUTOMATED COUNTING OF THE ETCH PITS WITH STREAM

After the irradiation and etching of samples, the determination of the areal density of the etch pits is of great importance for the further assessment of the results received. For samples etched with EDTA + acetic acid, this meant manually counting all the etch pits in a certain area, which was very time-consuming. As seen in Chapter 6, etching with HNO_3 reveals distinct black dots in the middle of an etch pit in transmitted light (Fig. 9.8). This dot is interpreted as the ion track, but even more important, it gives a clear contrast to the surrounding calcite lattice and therefore the black dots can be counted automatically using an image editing software, for example Stream (Fig. 9.9). This greatly simplifies the working process, once the parameters for an automated counting process have been set.

10

ANNEALING EXPERIMENTS

CONTENTS

10.1 INTRODUCTION

After developing basic etching procedures for irradiated calcite crystals (see Chapters 5 & 6), the objective of this chapter is to test the behavior of irradiated calcite crystals after being heated for a specific time at certain temperatures. The main topic is an understanding of the annealing speed and the annealing behavior of swift heavy ion-induced etch pits, and determining a closing temperature for ion tracks in calcite. In addition, testing was carried out to ascertain whether the annealing behavior could be used as a tool to distinguish between etched ion tracks and etched natural defects. Therefore the behavior of etched natural defects was investigated as well.

After irradiation, the calcite crystals were heated in ***Heraeus*** laboratory ovens for 100 h at temperatures between 200°C and 500°C (± 5 °C). Results are established on the basis of areal density of the etch pits and optical description. Samples used are listed in Table 15-2 in the appendix.

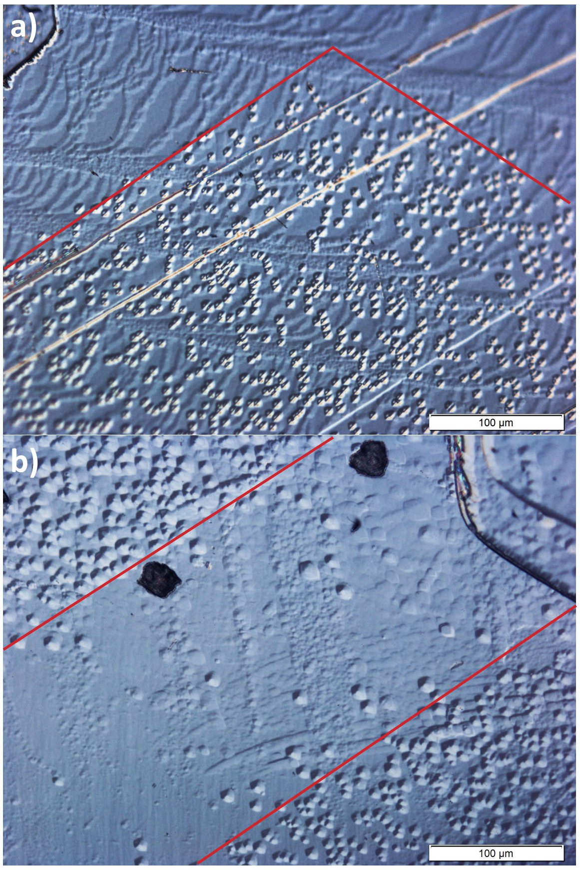

Fig. 10.1: Comparison of two samples: a) irradiated (1×10^6 ions/cm^2, 11.1 MeV/u, ^{197}Au), not annealed. The pattern of the hexagonal mask are clearly visible. b) irradiated and annealed at 200 C for 100 h. The pattern of the mask, marked in red, is still clearly visible.

10.2 ANNEALING EXPERIMENTS

10.2.1 First approaches between 100 °C and 500 °C

The first approach to determine the closing temperatures of ion tracks in calcite was to narrow down the closing temperature by heating-up irradiated calcite crystals at 200, 300, 400 and 500 °C for 100 h prior to the etching procedure.

At 200°C the areal density of the heated crystals matches the areal density of a non-heated crystal, so no significant annealing has taken place (Fig. 10.1). But already the next step with heating at 300°C showed no etched ion tracks and therefore the closing temperature had been exceeded (Fig. 10.2). This result was confirmed by the 400°C and 500°C crystals, where no etched ion tracks were visible either. For the 500°C experiment one bigger crystal was cracked into two pieces, one of which was heated, and the other not. The non-heated half clearly showed etched ion tracks, thus the crystal had been irradiated properly (Fig. 10.3). The areal density of etch pits of the heated crystals corresponds approximately to 1x10^4 etch pits/cm^2, which matches the areal density of Type A dislocations (Fig. 10.4).

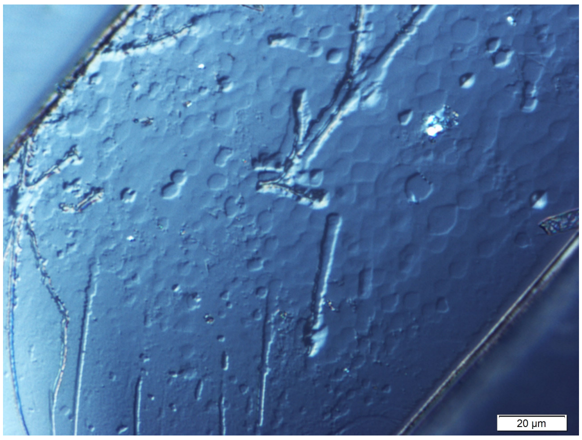

Fig. 10.2: Calcite crystal irradiated with 1×10^6 ^{197}Au ions and then annealed at 300 °C for 100 h. No etch pits of irradiated ion tracks are visible.

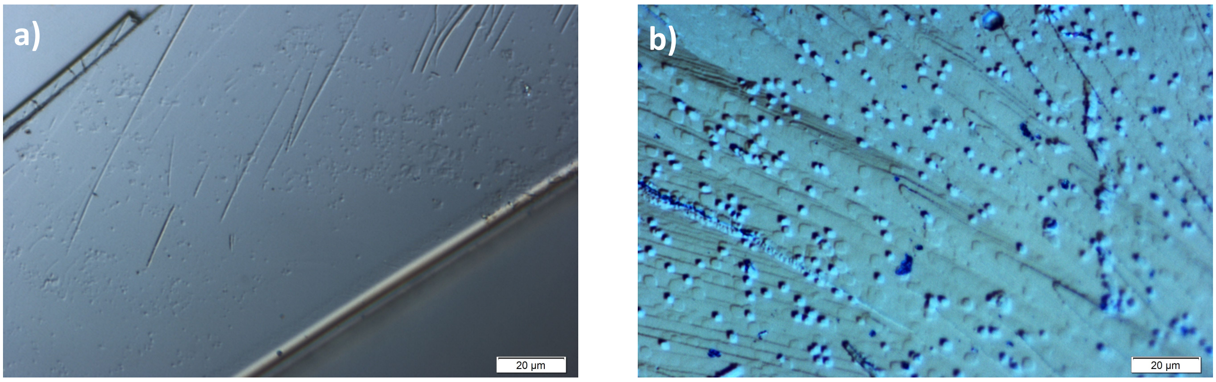

Fig. 10.3: Calcite crystal divided into two pieces. One piece (a) reheated at 500°C. No etched ion tracks are visible. The other piece (b) was not reheated and therefore the ion tracks are still intact and etchable. Image after 5 s of etching.

10.2.2 Annealing behavior between 200 °C and 300°C

To isolate the temperature at which ion tracks anneal, samples (irradiated with 1×10^6 Au ions/cm^2) were left in the furnace for 100 h at temperatures of 220, 240, 260 and 280 °C. Analysis of the samples showed that the ion-induced etch pits disappear between 240 and 260 °C (Fig. 10.5). The etch pits on the 240 °C sample are obviously beginning to anneal. They are fainter than the etch pits on the sample annealed at 220 °C. The hexagonal mask was first seen after 15 s of etching, instead of instant visibility after 5 s of etching as was observed on the samples annealed below 240 °C. Even after 20 s of etching the hexagonal mask was barely visible (Fig. 10.6). At 240°C the shape of the etch pits starts to become more undefined. In addition, the contrast of the etch pits to the crystal surface, which provided a reliable tool to identify etch pits, has become very low and therefore the etch pits are more difficult to identify (Fig. 10.7). This is also the reason for the 2 data points in Figure 10.5. For the higher value, everything looking like an etch pit has been counted; for the lower value more stringent criteria concerning the etch pits were applied and therefore fewer etch pits were counted. An interesting fact is that the etch pits are not smaller than non-heated etch pits. They are roughly the same size. The reason for this is that the ion tracks are starting to anneal, producing shorter, narrower ion tracks which are more difficult to etch. Most likely, the etch pits are more shallow than non-annealed etch pits, but this feature could not be verified.

10.3 Discussion

Annealing experiments with calcite crystals showed that the etchability of ion tracks disappear between 240 °C and 260 °C. Due to the fact that dislocations do not anneal at that temperatures, a reliable tool to distinguish between etched ion tracks and dislocations is at hand.

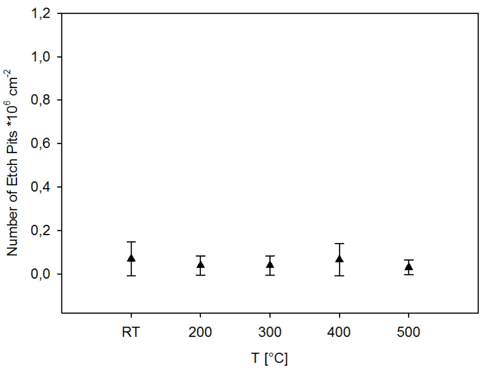

Fig. 10.4: Areal density of Type A dislocation on non-irradiated calcites after 20s of etching with EDTA + acetic acid.

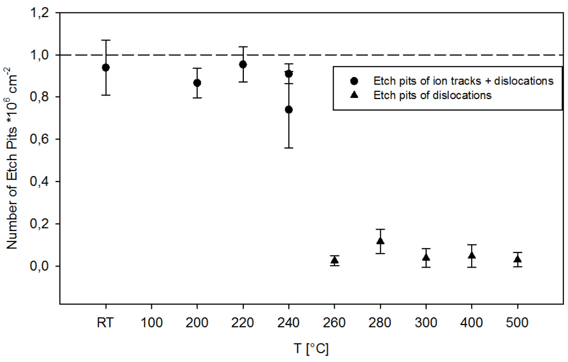

Fig. 10.5: Areal density of etch pits on reheated calcite crystals after 20 s of etching. Dashed line indicates used fluence. The areal density drops between 240 and 260°C to Type A dislocation level.

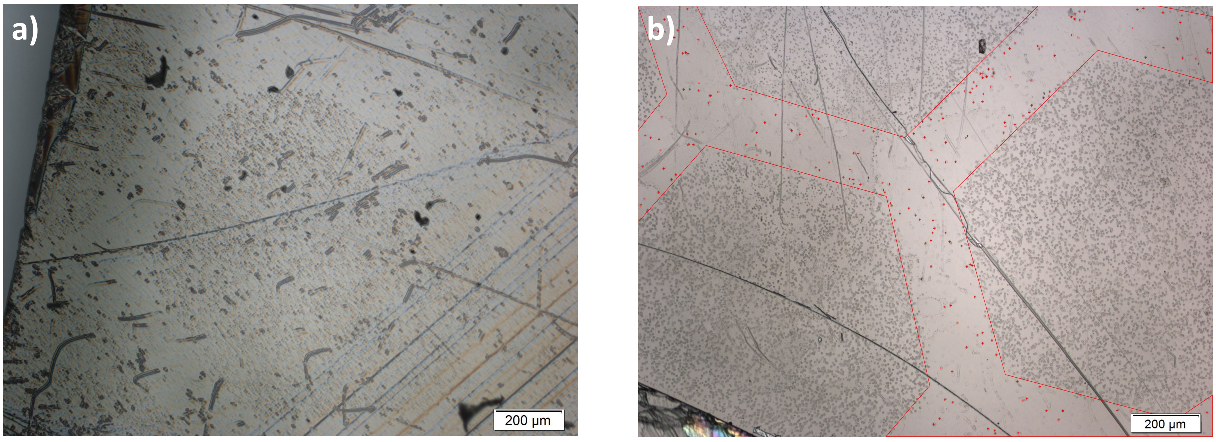

Fig. 10.6: Comparison of a calcite annealed at 240°C, 100h (a) and a calcite without annealing (b) after 20 s of etching. The hexagonal mask on the left side is barely visible whereas the hexagonal mask on the non-reheated crystal on the right is clearly visible.

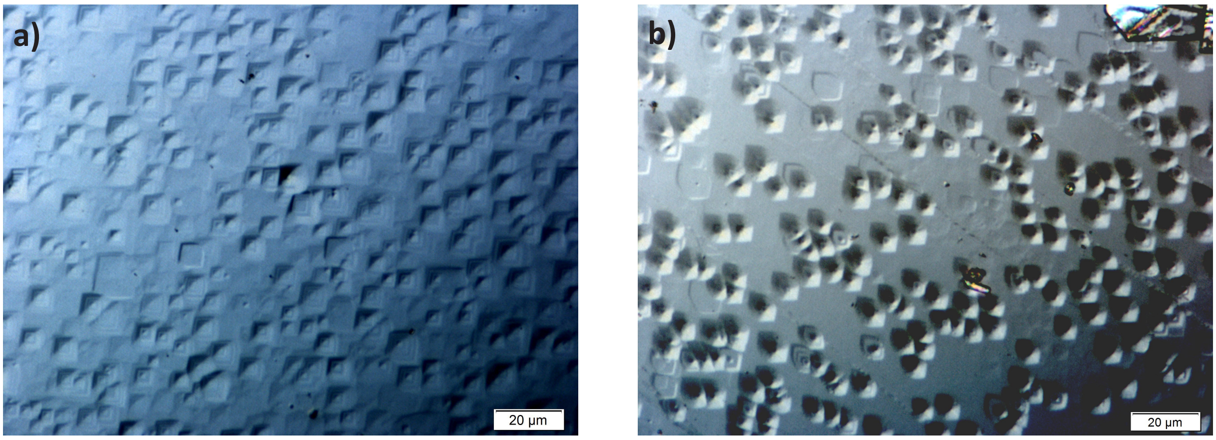

Fig. 10.7: Difference between etched ion tracks on a reheated crystal (240 °C, 20 s, a) and an non-reheated crystal (20 s, b). The contrast between the crystal surface and the etch pits on the reheated crystal is significantly lower than on an non-reheated crystal

Admittedly it is not guaranteed that fission fragments behaves in the same way, because maybe the size of fission tracks has changed over a million years and therefore react more like a Type A defects to etching. Completely annealed irradiated calcite crystals have a similar areal density to non-irradiated calcite crystals, due to the fact that dislocations cannot be annealed at temperatures up to 500 °C.

In their publication, SIPPEL & GLOVER suggested using annealing to determine the areal density of induced fission tracks. Their method is based on the fact that dislocations do not anneal at lower temperatures, like ion-induced tracks. This observation could be confirmed in this study. A possible procedure could be:

1. Divide a calcite crystal into two pieces.
2. One piece is annealed, the other piece not.
3. Both pieces are etched with the same etching solution.
4. The etch pits are counted.
5. Subtract the areal density of etch pits of the annealed piece from the areal density of etch pits from the non-annealed sample.
6. The result is the areal density of fission tracks.

Tests are necessary to ensure that such a procedure works properly, because there are some sources of error: dislocations are not necessarily evenly distributed on the calcite surface, and to some extent the counting itself is a potential source of error. But this method could provide an approach to establishing the actual fission-track density, and due to the lack of alternatives, it should be considered.

11

ONLINE RAMAN SPECTROSCOPY

CONTENTS

11.1 INTRODUCTION

During this doctoral thesis, the possibility came up of designing and testing an online Raman system at the UNILAC, GSI Darmstadt. Raman spectroscopy has been widely used in geoscience and materials research to determine material changes caused by accelerated ions or natural radioactive fission products. Radiation-induced modifications are typically analyzed ex-situ and long after the irradiation has taken place. For a better understanding of dose dependent effects, in many cases a series of samples is exposed to different ion fluences. If, however, the material to be studied is anisotropic or inhomogeneous, it is almost impossible to analyze similar or identical crystallographic locations for the different fluence measurements. To avoid these difficulties, the system was designed to perform Raman spectroscopy online in the irradiation chamber prior to, during, and shortly after irradiation, in order to analyze how a given sample spot changes as a function of ion fluence. The advantages of in-situ measurements are a flexible fluence management and above all a guarantee that the same spot of the sample is being measured at all fluences and all measurements. This prevents influences of crystal properties like anisotropy from affecting the Raman measurements. The requirements for the online Raman system were:

A mobile system, to save storage space in the experimental hall and make it possible to use it at various facilities.

- Compact design, to fit into the spectroscopy chamber at the M3-branch.
- Stable installation of the components, to avoid misalignments through unintentional physical contact.
- Easy to install and use.
- Easy sample exchange to save valuable beamtime
- Remotely controllable

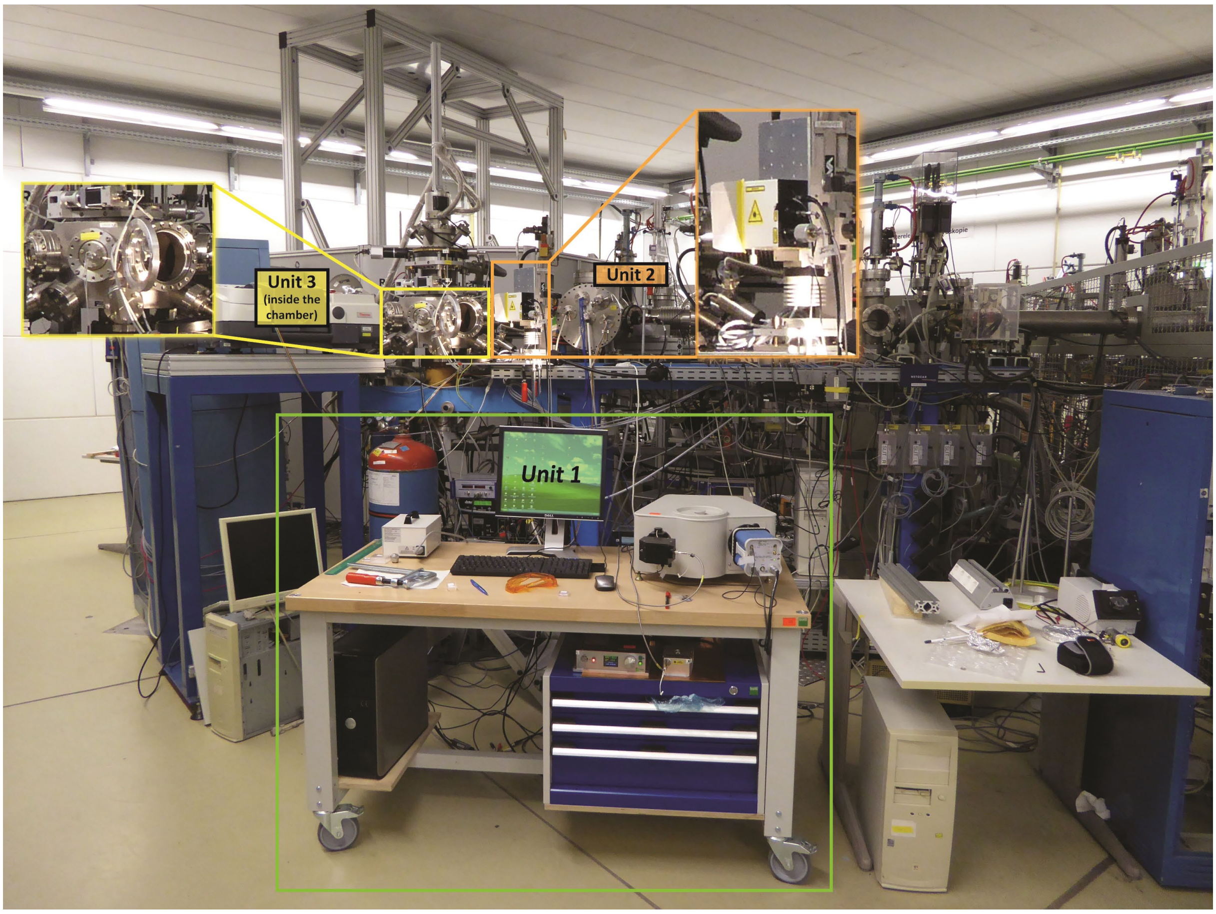

Fig. 11.1: M- branch at GSI, with the Units 1-3 marked.

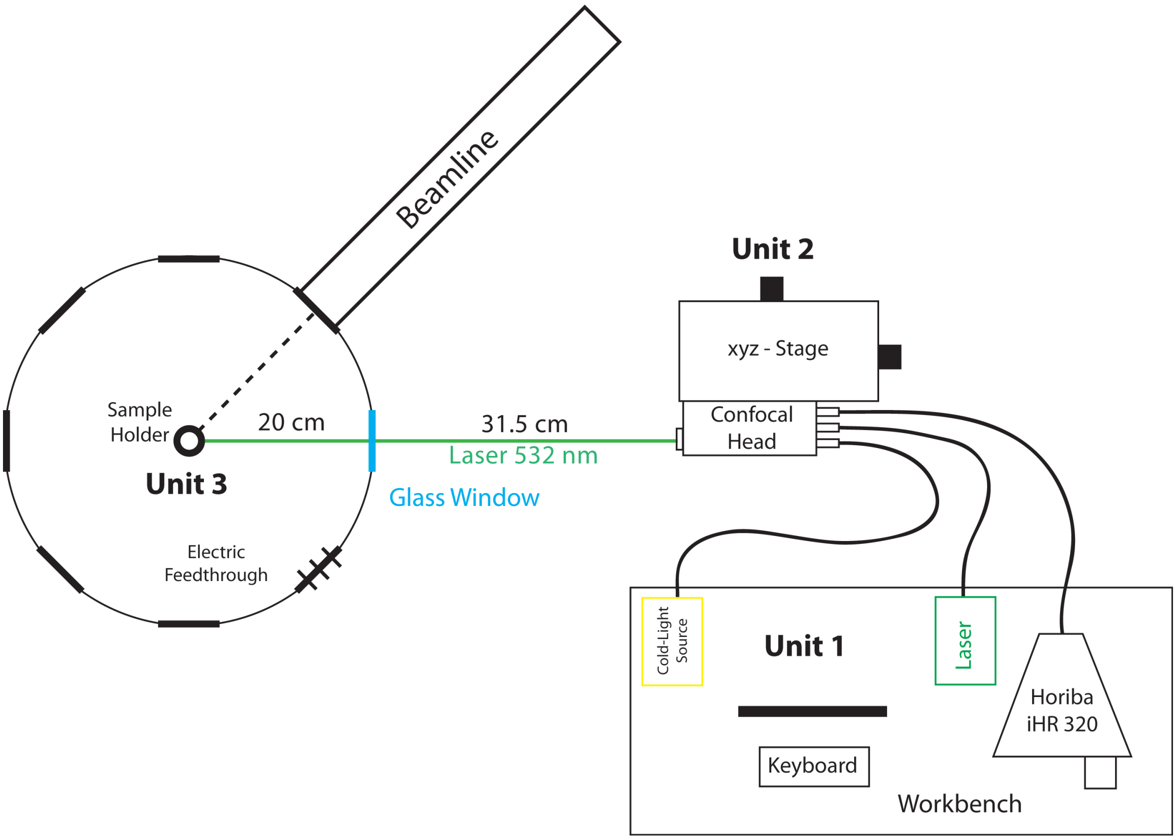

Fig. 11.2: Scheme of the mobile Raman system attached to the M3-beamline at the UNILAC.

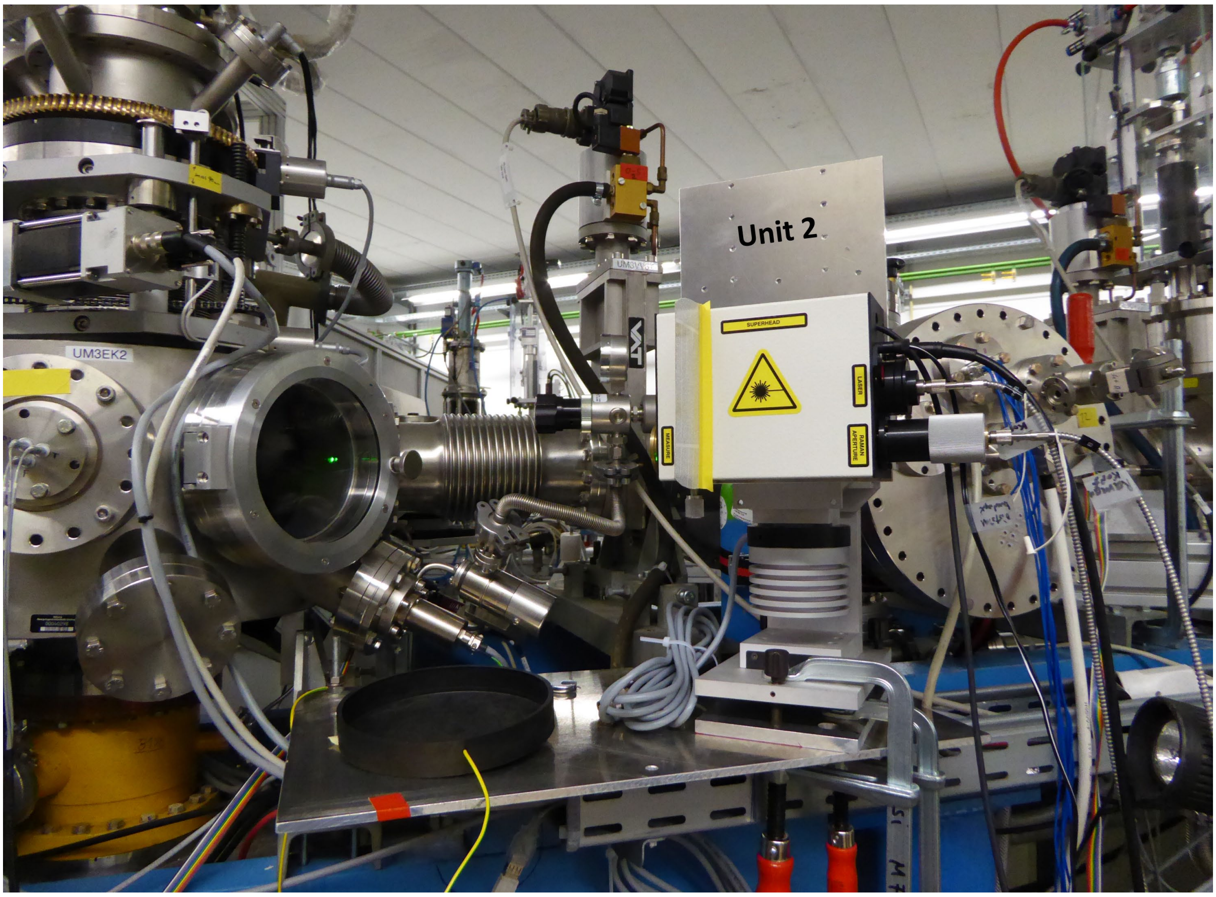

Fig. 11.3: Unit 2 in front of the spectroscopy chamber.

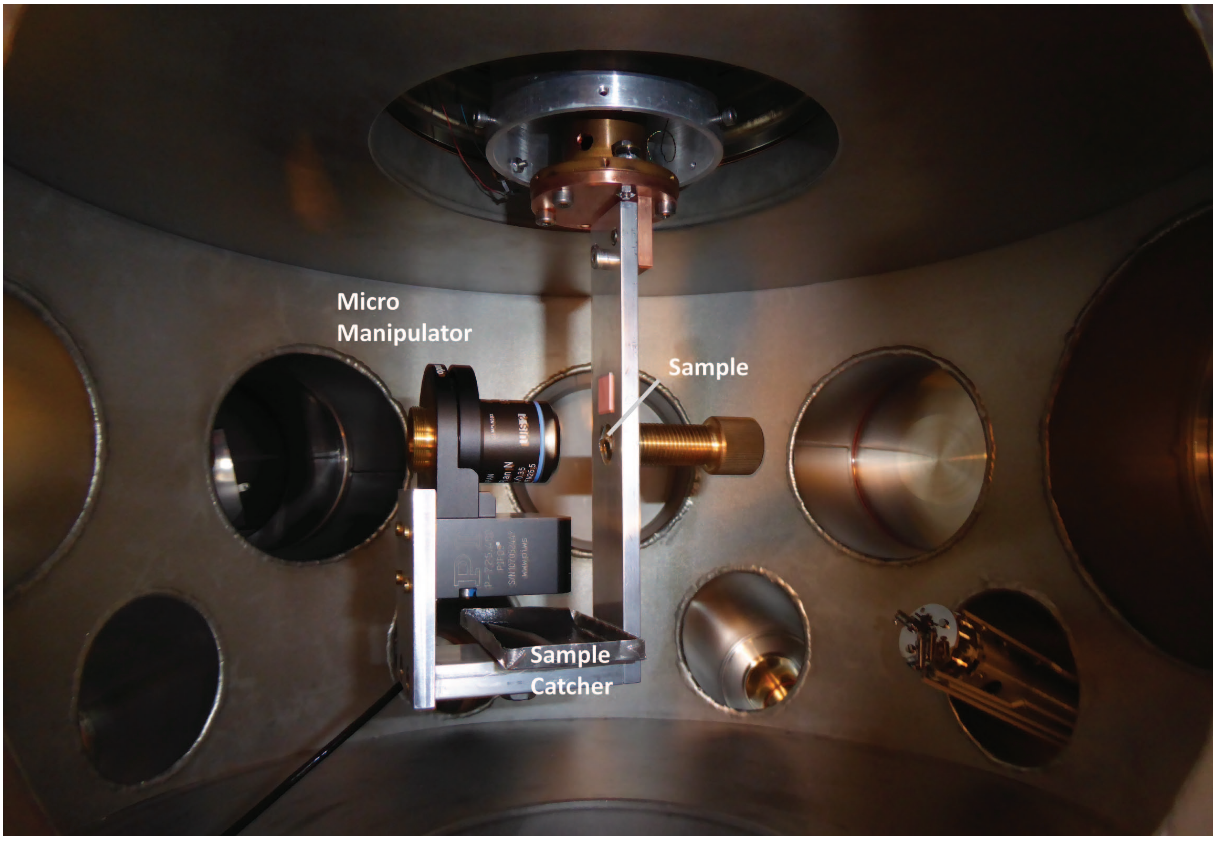

Fig. 11.4: Unit 3 inside the spectroscopy chamber

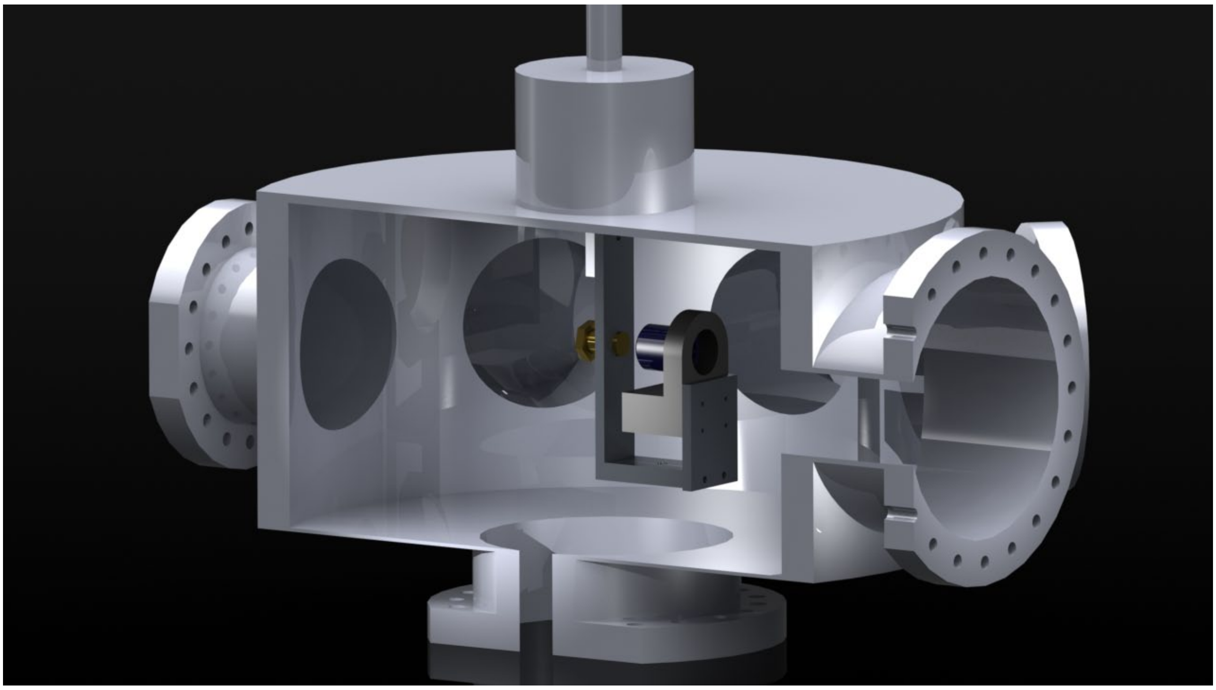

Fig. 11.5: Model of the M3 - spectroscopy chamber with mounted Unit 3. The sample will be mounted on top of the bronze screw.

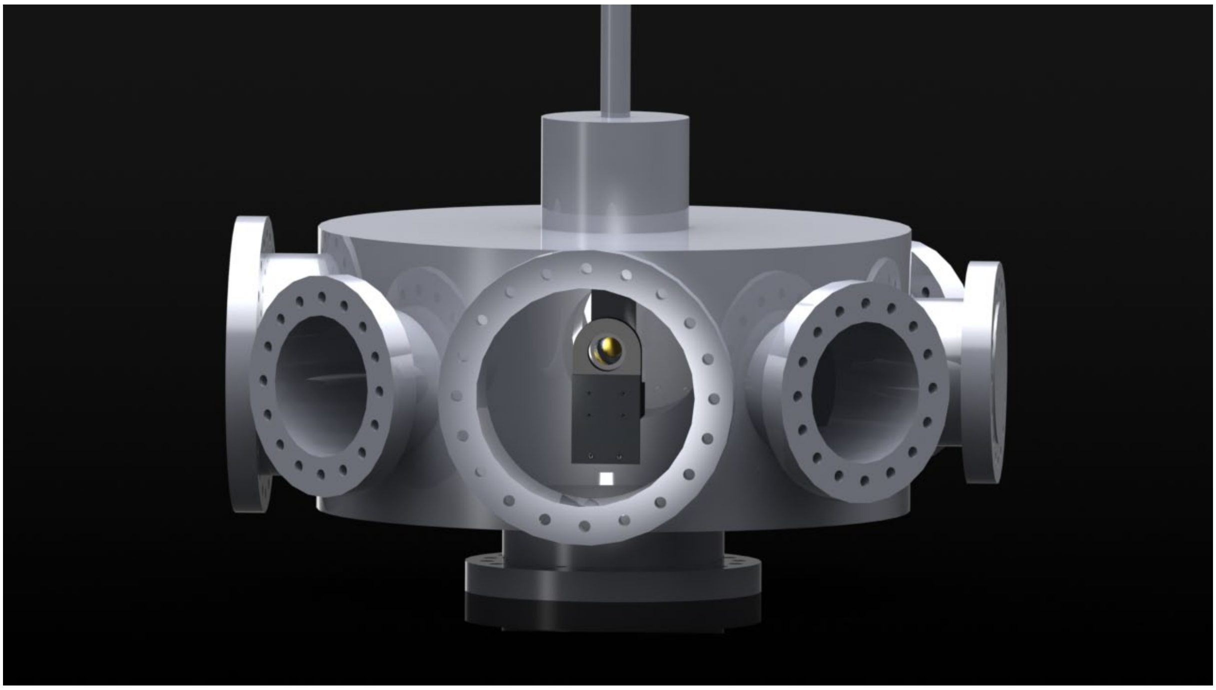

Fig. 11.6: Model of the M3 - spectroscopy chamber with mounted Unit 3. View from outside the chamber as seen from the confocal head.

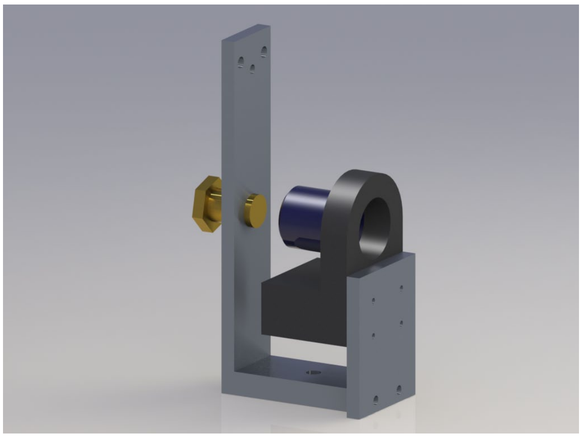

Fig. 11.7: Model of the sample holder designed for this online Raman system at M3, GSI.

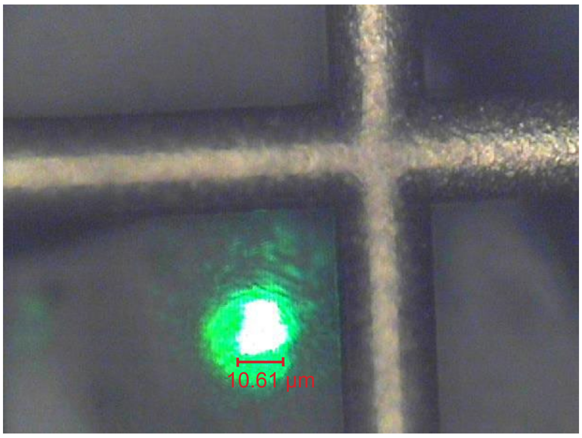

Fig. 11.8: Image of the video system of the online Raman system. The laser spot on the sample has a diameter of approximately 10 µm. The cross visible originates from a calibration pattern.

11.2 METHODS

The Raman spectrometer was attached to the all-purpose irradiation chamber of the M3-beamline at the UNILAC. The M-branch where the online Raman was installed consisted of three experimental beamlines located at GSI, UNILAC.

M1 holds an electron microscope, M2 an online four-circle x-ray diffractometer, and M3, where the online Raman was placed, is a multi in-situ spectroscopy chamber. Besides the Raman spectrometer, it is possible to mount an infrared spectrometer, a UV/Vis spectrometer, an in-situ luminescence spectrometer and an in-situ samples curvature measurement. The final online Raman system developed consists of three main units (Fig. 11.1 & Fig. 11.2):

The first unit consists of a work bench equipped with fixed rollers on which all heavy and large equipment is placed: the ***Horiba Jobin Yvon*** iHR 320 spectrometer with a Pelletier cooled camera, the laser system consisting of a ***Laser Quantum***

Ventus 532 nm Laser with 90 mW power and the laser control unit ***Laser Quantum*** MPC 6000. Additionally, the work bench holds the controlling PC with ***Horiba*** LabSpec 5 software plus peripheral devices and three drawers for smaller accessories.

The second unit (Fig. 11.3) comprises an XYZ - stage (manual controlled) with attached ***Horiba*** Superhead + ***Euromex*** EK1 cold light source, which provides the confocality of the system. This system is mounted with screw clamps in front of the sample chamber window which consists of normal glass.

The third unit is located inside the 400 mm diameter sample chamber (Fig. 11.4, Fig. 11.5 & Fig. 11.6). This third unit of the system consists of the custom-made sample holder with an ***Olympus*** SLMPlan N 50x objective (working distance: 18 mm) attached to a micro manipulator (***Physics Instrument*** PI P-725.4CD) and a device to hold the samples during the experiment (Fig. 11.7). The unit has been designed to guide the laser and the ion beam to the same spot on the sample without hitting and thus affecting the objective mounted on the sample holder. This has been realized with a careful choice of the components, for example the choice of an objective with a matching focal plane. All parts of the third unit are suitable for operation in ultra-high vacuum.

With all units mounted, and the superhead connected via optical fiber to the spectrometer, the laser and the cold light source placed on the workbench, the distance from the superhead to the window is approximately 31.5 cm. The distance from the superhead to the objective entrance is about 51.5 cm, which represents the distance through air covered by the infinity-corrected 50x objective. To achieve a maximum Raman signal the superhead has to be adjusted very carefully with the XYZ-stage. The alignment and subsequent calibration of the system is performed with a silicon chip using its strong 520.7 cm^{-1} Raman band. Samples can be mounted on top of the brass screw that serves as the coarse drive of the sample holder. After placing the sample roughly in position, final focusing is performed with the PI micro-manipulator, which is connected to the control unit (***Physics Instrument*** E-665.CR) via a vacuum feed-through. To finalize the system setup, the Raman controlling PC is connected to the control room via a remote desktop connection.

To test the system's performance in displaying beam-induced changes, calcite ($CaCO_3$) crystals from Chihuahua, Mexico were chosen for the first experiments, because calcite and its fluence dependent changes in Raman spectra are known from offline experiments (PABST et al. 2010). Additionally, macro to micro-crystalline malachite $Cu_2CO_3(OH)_2$ from Katanga (Shaba), DR Congo has been chosen to test the system. As malachite is an anisotropic mineral with different Raman spectra at different orientations determination of the ion-induced material changes by Raman spectroscopy has to be done at the same crystal orientation for all fluences. The new online Raman spectroscopic system fulfils this requirement.

The following Raman bands are important for the malachite sample used in the experiment and will be discussed within the scope of material change caused by swift heavy ion irradiation: two δ HO-Cu^{2+}-OH bending modes at ~145 cm^{-1} and ~154 cm^{-1}, one not specified but characteristic vibration band at ~180 cm^{-1}, δ O-Cu^{2+}-OH bending modes at ~220 cm^{-1}, three ν Cu^{2+}-OH stretching modes at ~351 cm^{-1}, ~434 cm^{-1} and ~538 cm^{-1}, two v1 $(CO_3)^{2-}$ symmetric stretching modes at ~1060 cm^{-1} and ~1100 cm^{-1}, the doubly degenerated v3 $(CO_3)^{2-}$ asymmetric stretching mode at ~1496 cm^{-1} and the hydroxyl vibration modes of OH at 3309 and 3382 cm^{-1}. The interpretation of the Raman bands is taken from published data (FROST et al., 2002; FROST et al., 2011; ČEJKA et al., 2013).

The irradiation of the calcite crystal was performed with 4.8 MeV/u Au ions, the irradiation of the malachite crystal with 4.8 MeV/u Bi ions (both 2 Hz, pulse length 1.2 ms, stopping parameters in Tab. 11-1). After calibration, alignment, and focusing of the Raman system, the crystals

Tab. 11-1: Calculation of the penetration parameters of a calcite crystal at the irradiation with Au ions and Bi ions with an energy of 4.8 MeV/u. Calculation made with SRIM.

Mineral	Ion	Ion Energy [MeV]	dE/dx Elec. [keV/µm]	dE/dx Nuclear [keV/µm]	Projected Range [µm]
Calcite	Au	945	2.66×10^4	4.66×10^1	46.04
Malachite	Bi	1000	3.42×10^4	6.53×10^1	39.00

were exposed to the ion beam in steps from 1×10^9 ions/cm^2 up to a fluence of 1×10^{12} ions/cm^2. Tab. 11-2 provides an overview of the irradiation steps. After each irradiation step, Raman spectra (focused onto the surface) were recorded with 20 s acquisition time and 3 accumulations. The laser spot on the sample is about 10 µm in diameter (Fig. 11.8).

11.3 RESULTS

11.3.1 Calcite ($CaCO_3$)

The Raman spectra of calcite show four major changes during irradiation (Fig. 11.10). The amplitude of the two bands at 156 and 284 cm^{-1} (Ca-bands, GUNASEKARAN et al., 2006; RUTT et al., 1974) decrease with increasing fluence. Both are still occurring at a fluence of 1×10^{12} ions/cm^2. The Raman band at 435 cm^{-1} appears for the first time above a fluence of 2×10^{10} ions/cm^2. With increasing fluence the amplitude of the band at 435 cm^{-1} is increasing and reaches a maximum at 5×10^{11} ions/cm^2. This band is known from former research, but until today the physical meaning of the band is not known. The Raman band at 1087 cm^{-1} (sym. CO_3 stretching) is widening at fluences of more than 5×10^{11} ions/cm^2 and the full width at half maximum increases significantly from 7.4 cm^{-1} (Non-irradiated to 1×10^{11} ions/cm^2) to 9.57 cm^{-1} at a fluence of 1×10^{12} ions/cm^2 (Fig. 11.9).

Tab. 11-2: Irradiation steps for calcite and malachite

Calcite	Malachite
Non-irradiated Ref.	Non-irradiated Ref.
1×10^9 ions/cm^2	1×10^9 ions/cm^2
1×10^{10} ions/cm^2	1×10^{10} ions/cm^2
2×10^{10} ions/cm^2	2×10^{10} ions/cm^2
5×10^{10} ions/cm^2	4×10^{10} ions/cm^2
7×10^{10} ions/cm^2	7×10^{10} ions/cm^2
1×10^{11} ions/cm^2	8×10^{10} ions/cm^2
2×10^{11} ions/cm^2	9×10^{10} ions/cm^2
5×10^{11} ions/cm^2	1×10^{11} ions/cm^2
1×10^{12} ions/cm^2	3×10^{11} ions/cm^2
	5×10^{11} ions/cm^2

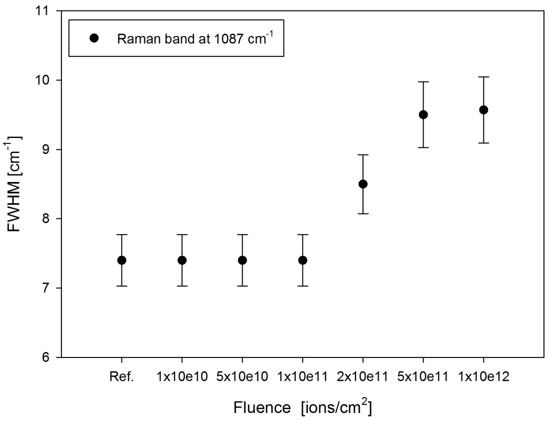

Fig. 11.9: FWHM of the 1087 cm^{-1} band of calcite. Increasing value from a fluence of 2×10^{11} ions/cm^2. Error = 5 % of value

11.3.2 Malachite $Cu_2CO_3(OH)_2$

Swift heavy ion irradiation of macro to micro-crystalline malachite caused significant changes of the Raman spectra with increasing ion fluence. The change in Raman spectra allowed to separate the 10 Raman spectra into 3 distinct groups (Fig. 11.12):

A: 1×10^9 ions/cm^2 – 7×10^{10} ions/cm^2,
B: 8×10^{10} ions/cm^2 – 1×10^{11} ions/cm^2,
C: 3×10^{11} ions/cm^2 – 5×10^{11} ions/cm^2,

Raman spectra of Group A:

With increasing fluences the intensity of all Raman bands decrease (Fig. 11.11). Within the wavelength accuracy the band position does not change within this first group (see Chapter 2).

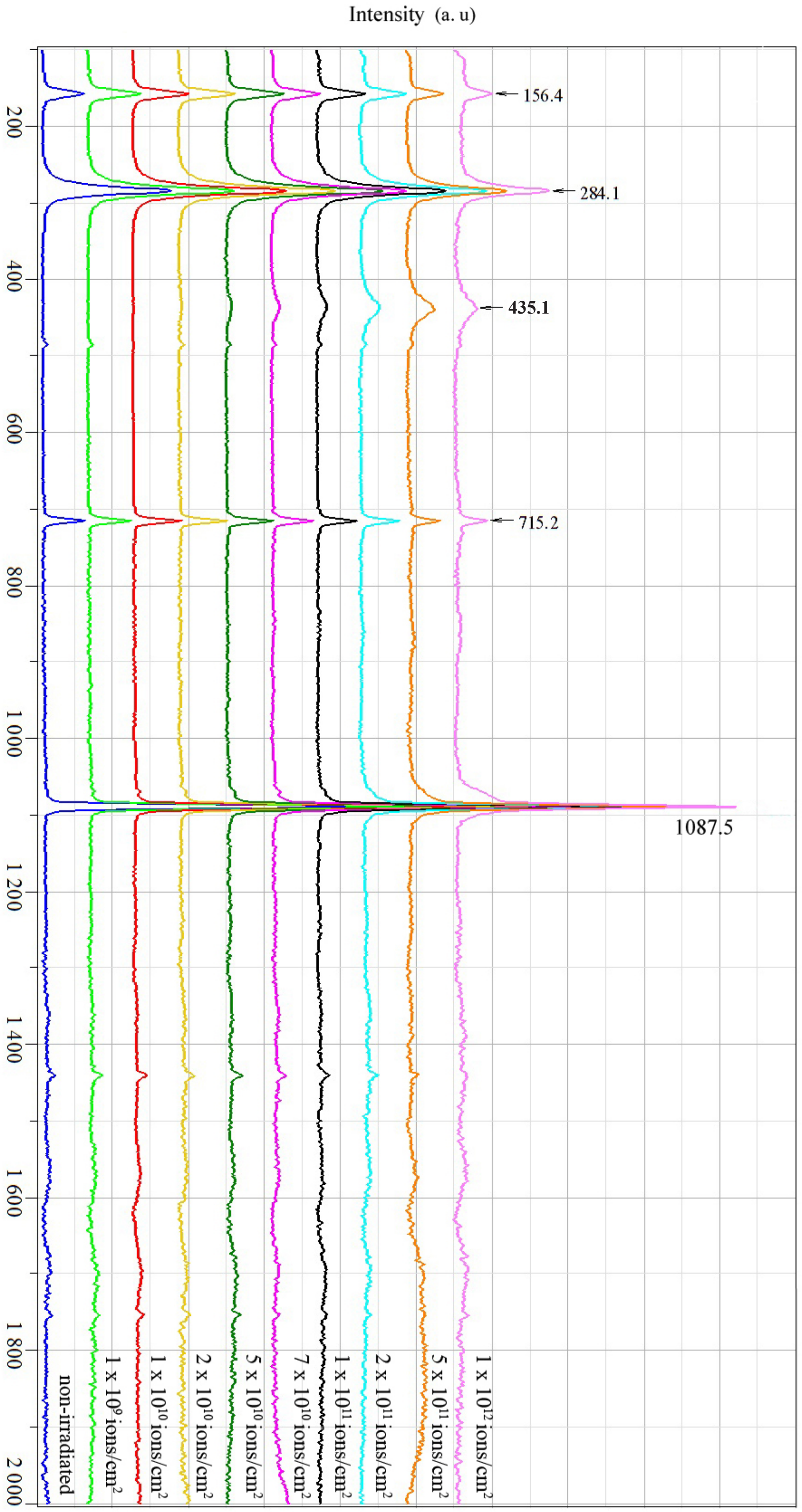

Fig. 11.10: Raman spectra of calcite during irradiation with swift heavy ions (4.8 MeV/u, ^{197}Au). The spectra were baseline corrected and stacked for better comparability.

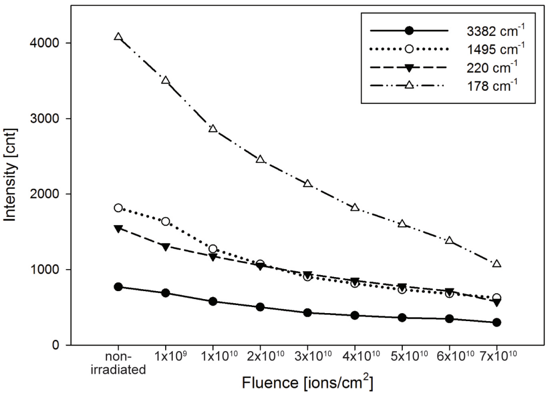

Fig. 11.11: Decrease of intensity of four malachite bands through irradiation with swift heavy ions.

Raman spectra of Group B:

The following Raman bands can still be identified after irradiation with a fluence of 8×10^{10} ions/cm^2: one δ HO-Cu^{2+}-OH bending modes at ~145 cm^{-1}, one not specified but characteristic vibration band at ~180 cm^{-1}, δ O-Cu^{2+}-OH bending modes at ~220 cm^{-1}, the doubly degenerated v3 $(CO_3)^{2-}$ asymmetric stretching mode at ~1496 cm^{-1}. The hydroxyl vibration modes of OH at 3309 and 3382 cm^{-1} are not visible any longer. Nevertheless, the three bands between 110 cm^{-1} and 220 cm^{-1} are superimposed by one broad band. A new Raman band develops at about 1573 cm^{-1}.

The Raman spectrum of a fluence of 9×10^{10} ions/cm^2 is characterized by the broad band between 110 cm^{-1} and 220 cm^{-1} with superimposed clear defined four bands. A new band at 114 cm^{-1} appears in addition to the old three bands. In addition, between 1000 cm^{-1} and 1750 cm^{-1} a new asymmetric broad band appears that is characterized by two distinct new bands at 1364 cm^{-1} and 1573 cm^{-1}. At this fluence, the two new bands reach their maximum of intensity within the whole experiment and decrease in intensity at the next irradiation step (1×10^{11} ions/cm^2). In contrast, the amplitude of the superimposed four Raman bands between 110 cm^{-1} and 220 cm^{-1} increase in intensity up to a fluence of 1×10^{11} ions/cm^2.

Raman spectra of Group C:

At the fluence of 3×10^{11} ion/cm^2 the amplitude of the superimposed four Raman bands between 110 cm^{-1} and 220 cm^{-1} decrease significantly. The Raman band at 1364 cm^{-1} vanished and the Raman band at 1573 cm^{-1} nearly vanished. At a fluence of 5×10^{11}ion/cm^2 the only Raman band that is left over is the broad band between 110 cm^{-1} and 220 cm^{-1} with one stronger Raman band at 218 cm^{-1}. In addition, between 2000 cm^{-1} and 4000 cm^{-1} fluorescence is visible.

11.4 DISCUSSION

Overall, the Raman spectra of calcite indicate the first occurrence of Raman band at 435 cm^{-1} at a fluence of 5×10^{10} cm^{-1}. With increasing fluence the amplitude of this Raman band increase. Therefore, we interpret the formation of the Raman band as caused by the ion irradiation. Separate investigations excluded the formation of CaO as a possible source for the new Raman band.

For malachite, the intensity decrease of the amplitude of all Raman bands between a fluence of 1×10^{9} ion/cm^2 and 7×10^{10}ions/cm^2 (Group A) is related to the change of matter by the irradiation with swift heavy ions.

The most interesting stage of the irradiation of malachite is at a fluence of 9×10^{10} ions/cm^2 (Group B). The four bands between 110 and 220 cm^{-1} decrease in amplitude significantly and are superimposed by one distinct band, which is caused by the vibration of Cu_2O (WANG et al., 2010) These Raman bands keep in all spectra up to a fluence of 5×10^{11} ions/cm^2.

Simultaneously to the new Cu_2O-band, a broad carbon structure between 1000 cm^{-1} and 1750 cm^{-1} with two distinct superimposed Raman bands at 1364 cm^{-1} and 1573 cm^{-1} developed. Similar Raman bands are described in the literature for well-defined carbon structures such as graphene, single wall carbon nanotubes, and others (DRESSELHAUS et al., 2002; DRESSELHAUS et al., 2005; DRESSELHAUS et al., 2002a; MALARD et al.,

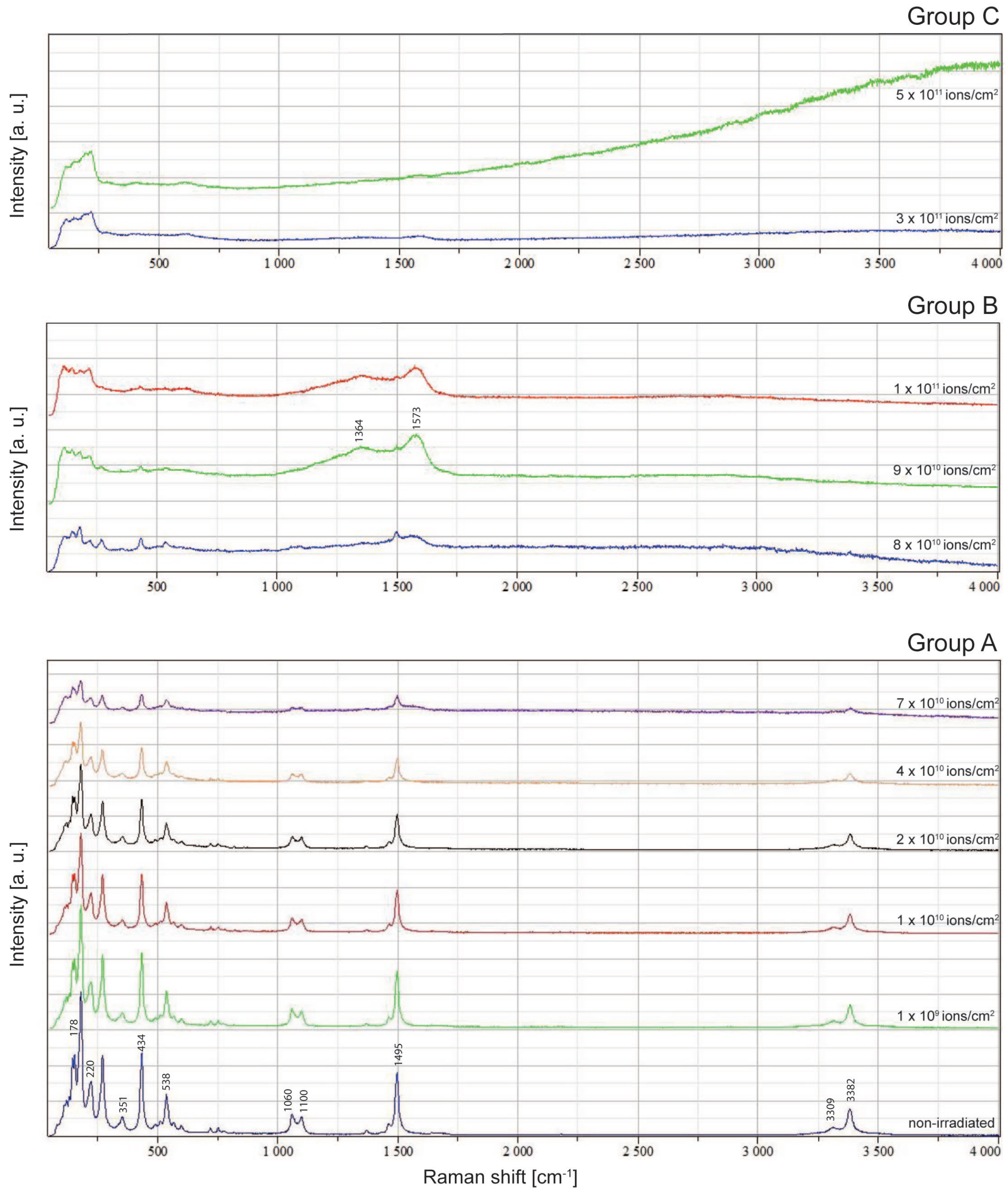

Fig. 11.12: Three groups of Raman spectra of malachite

2009; Saito et al., 2002; Ferrari, 2007; Reich & Thomsen, 2004; Thomsen et al., 2007; Nohara et al., 2005). As the irradiation was continued, the Raman spectra of the "malachite sample" above a fluence of 1×10^{11} ions/cm^2 indicate a loss of these two bands (Group C). Therefore, we interpret the spectra as indicating the destruction of the carbon structure at higher fluences.

11.5 CONCLUSION

11.5.1 Technical Aspect

Overall, the system worked as expected. As benchmark, intensities of 1100 counts at 1 s acquisition time could be achieved for the 520.7 cm^{-1} band of silicon. This intensity is sufficient for all minerals measured during the first irradiation campaign. For example, an intensity of 5500 counts could be achieved at 20 s acquisition time for the 1087 cm^{-1} band of calcite, which resulted in very good spectra.

Critical for all measurements is a proper alignment of the system prior to the experiments. Misalignments of the system cause drastic loss of intensity, and in the worst case they lead to damage to the equipment, for instance if the ion beam hits the objective of Unit 3. All scientific targets specified for the online Raman system previous to the experiments have been achieved. The intensities are usable; the system is sensitive enough to detect even small changes in the spectra caused by irradiation, like the 435 cm^{-1} band of calcite. Anisotropic effects of the samples, for example for malachite, could be eliminated by not moving the sample between the different irradiation steps.

In conclusion, the Raman system can be used as a standard method to investigate material change during swift heavy ion irradiation. The online Raman system is a valuable extension of the M3 measuring system.

11.5.2 Scientific Aspect

The above-described experimental results revealed the formation of Cu_2O by swift heavy ion irradiation and the coating of the malachite with a well-defined carbon structure. Such effects were never observed before. Furthermore, the step wise irradiation and Raman analysis at the same surface location determined the fluence depended change of malachite. It allows continuing with fluence-defined irradiation experiments to create Cu_2O and a coating of carbon nanostructures.

11.6 OUTLOOK

Improvements for the next version of the online Raman system will be a new sample holder which can handle multiple samples. Although the sample exchange itself can be performed within minutes with the current version, it is necessary to open the chamber for every new sample and therefore for every sample a new vacuum has to be pumped, which takes a lot of time. So to save valuable time, it should be possible to mount at least 3 samples on the sample holder. Moreover, the micro-manipulator is able to handle multiple samples, so focusing should not be a problem.

12

ANALYSIS OF IRRADIATED CALCITE CRYSTALS EXCITATED WITH UV-LIGHT

CONTENTS

12.1 MOTIVATION

While irradiating calcite crystals with swift heavy ions, the surveillance cameras of the irradiation chamber and the experimental cave showed a strong luminescence of the calcite crystal during the irradiation (Fig. 12.1- Fig. 12.3) and at higher energies even phosphorescence after shutting down the beam. Although calcite is known to produce luminescence on excitation by for example cathodoluminescence, this behavior, especially the long phosphorescence, is unusual. During literature research about the luminescence of calcite, a manuscript was found, GAFT et al. (2008), investigating the properties of the so-called “Terlingua-Calcite”. The characteristic features of this special calcite from New Mexico, USA are very strong fluorescence in long wave UV (366 nm, pink, Fig. 12.4), in short wave UV (254 nm, light blue) and long phosphorescence on a seconds scale (dark blue). GAFT et al. tried to find out why the luminescence and the phosphorescence are so strong in this particular calcite. They concluded that this was due to effects or defects generated by natural radiation, but they could not find conclusive evidence for this thesis. Due to the fact that the calcite crystal, irradiated in Cave A, had an extremely long phosphorescence of about 30 min, the idea came up, that maybe the structural properties of the irradiated calcite and the Terlingua calcite are the same or at least similar – perhaps the same defects causing phosphorescence were created through ion radiation as through the natural irradiation produced in the Terlingua calcite. When we assume that the processes of the defect building and the defects (or whatever causes the luminescence) itself are nearly the same, the irradiated calcite should re-

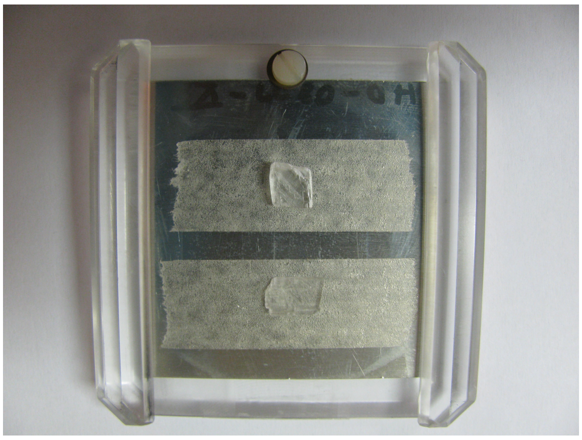

Fig. 12.1: Two calcite crystals, which were used for the luminescence test with an energiy of 11.1 MeV/u.

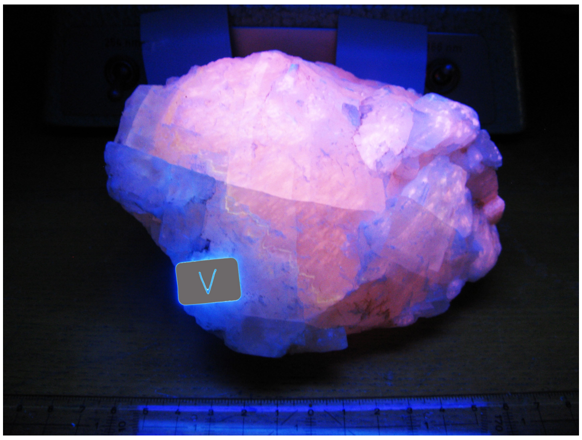

Fig. 12.4: The “Terlingua-Calcite” luminescing pink while irradiated with long wave UV at 366 nm. The “V” is indicating what was defined as the front of the rock.

Fig. 12.2: Two calcite crystals in the irradiation chamber, beam shut off

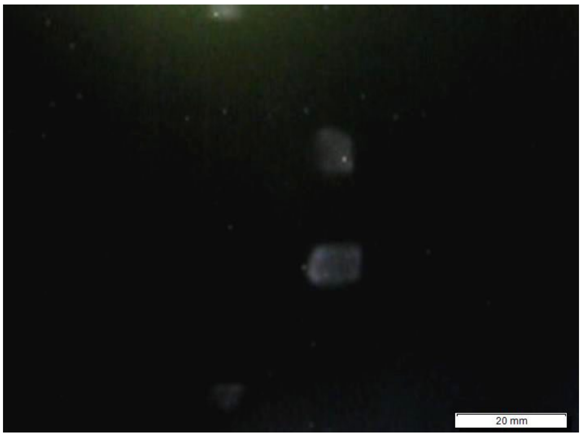

Fig. 12.3: Two calcite crystals in the irradiation chamber, beam on. The luminescence of the crystals is clearly visible.

Fig. 12.5: UV-lamp used for the UV-experiments

Fig. 12.6: UV-lamp used for the UV-experiments. It provides two different wavelength: a short wave UV-light at 254 nm and a long wave UV-light at 366 nm.

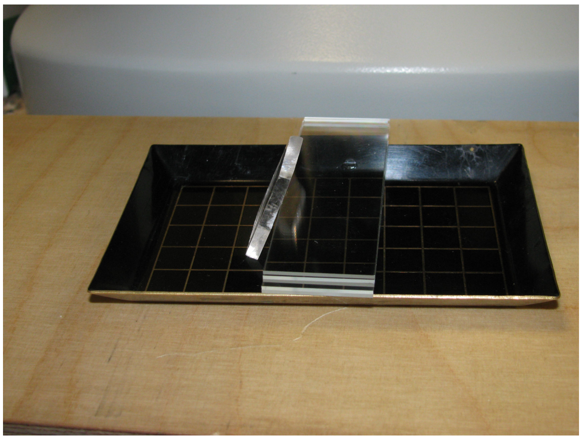

Fig. 12.7: Calcite crystal under the UV-lamp. The image illustrates the position of the crystal.

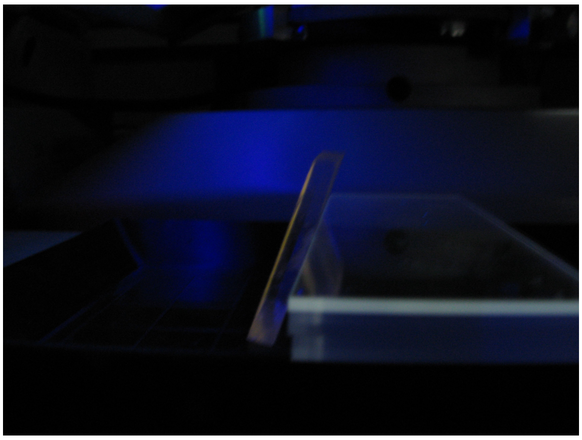

Fig. 12.8: Image of an irradiated crystal (5 x 10^8 ions/cm^2, U) under SW-UV-excitation. The crystal shows a thin greenish-yellowish luminescence on the irradiated side.

act similarly to the Terlingua calcite to UV excitation.

To test the reaction of irradiated calcite crystals to UV excitation, an old “Minuvis, Desaga Heidelberg” UV lamp (Fig. 12.5 & Fig. 12.6) with two wavelengths, long wave UV at 366 nm & short wave UV at 254 nm and a energy of 9 W was used.

12.2 INVESTIGATION WHILE UV LIGHT EXCITATION

12.2.1 Non-irradiated calcite, unetched

The non-irradiated Iceland Spar showed no luminescence, neither at the long wave (LW-UV) excitation at 366 nm nor at short wave (SW-UV) excitation at 254 nm.

12.2.2 Calcite crystal irradiated with medium energy (11.1 MeV/u, UNILAC)

The reaction of calcite crystals irradiated with medium energy (11,1 MeV/u) was tested with a series of calcites irradiated at X0 with fluences from 1×10^{10} to 2×10^{12} and samples irradiated during former beamtimes with 1×10^6, 1×10^7 1×10^8 and 1×10^9 (all Au ions/cm^2).

Testing the different fluences yield a minimum fluence of 1×10^{10} ions/cm^2 for the crystals to react to SW-UV excitation. Below 1×10^{10} ions/cm^2 no fluorescence could be detected with the naked eye. At this fluence applied to the crystal, a greenish to yellowish luminescence around the Bragg Peak area (see information box) which causes the most damage to the crystal lattice through irradiation is visible. The rest of the

Information: The Bragg-Peak

The Bragg peak is a pronounced peak of maximum energy loss on the Bragg curve which plots the energy loss of ionizing radiation during its travel through matter. For protons, α-rays, and other ion rays, the peak occurs immediately before the particles come to rest. This is called Bragg peak, for *William Henry Bragg* who discovered it in 1903.

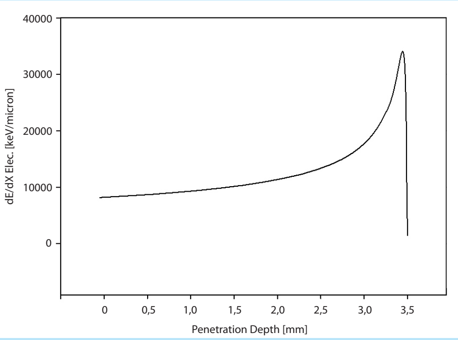

Energy loss of ^{238}U in Calcite. Initial ion energy: 192 MeV/u

crystal shows no reaction to the excitation. Due to the projected range of the swift heavy ions in calcite at 11.1 MeV/u of about 90 µm, only a very thin line on top of the crystal in the direction of the beam is showing fluoresce which can be best seen from underneath, through the transparent crystal. Unfortunately, it is not possible to quantify differences between the strength of the fluorescences without a spectrometer. But it can be stated that the fluorescence is increasing with increasing fluence applied to the crystals and the fluorescence of the 1×10^{10} ions/cm^2 calcite is much weaker than the fluorescence of the higher fluences and barely visible.

A test with a calcite irradiated with 5×10^{10} ions/cm^2 uranium at 8.6 MeV/u showed the same result: a clearly visible greenish yellowish fluorescence (Fig. 12.7 + Fig. 12.8). This shows that the ion used has no effect on the luminescence properties of the crystals. None of the tested crystals had fluorescence with LW-UV excitation.

12.2.3 Other calcites

A calcite was irradiated at Cave A with a very high energy, where the swift heavy ions passed through the crystal without stopping; no luminescence was visible either with SW or LW excitation.

12.3 DISCUSSION

A comparison of the results shows that the presumption of similar reaction of the irradiated calcite crystals and the Terlingua calcite was wrong. The irradiated calcite does not react in the same way. Instead of solving problems, a new problem occurs: what kinds of defects or effects are causing the greenish/yellowish fluorescence? Unfortunately no literature dealing with this problem is available. So the only possibility is a closer look at the results, and possible explanations and observations of the latter, which of course are highly speculative.

The experimental data indicated that the fluorescence only occurs in areas of maximum energy loss (Bragg-Peak area) more or less near the surface of the UNILAC irradiated calcites, which is associated with the penetration depth of only ~ 90 µm. The fact, that the "shot-through SIS calcite" shows no fluorescence visible with the naked eye confirms that a large damage density is needed to create a regime capable of being excited with SW-UV light. If fluorescence is present, it might only be detectable with a very sensitive spectrometer.

Furthermore, the experimental data showed that uranium irradiated calcites exhibit the same fluorescence as gold irradiated calcites - as far as this can be evaluated without a spectrometer. This leads to the conclusion that the damage caused by incoming ions creates a regime which can be excited with SW-UV light to show fluorescence. It is assumed that an uranium ion causes the same kind of damage like a gold ion just in higher volumes, due to the higher energy loss.

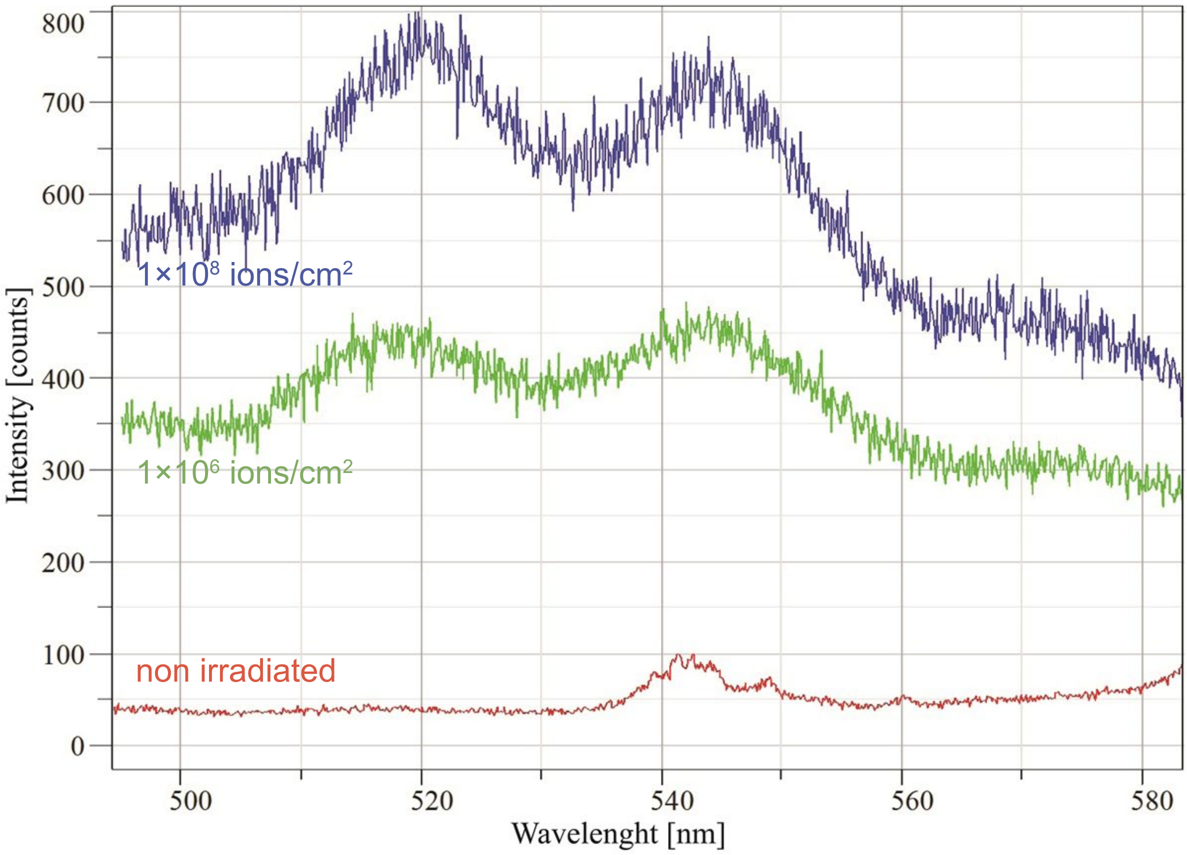

Fig. 12.9: Photoluminescence spectroscopy of calcite crystals irradiated with 1×10^6 and 1×10^8 Au-ions/cm^2 (11.1 MeV/u). Spectra are not shifted. (Detection time 20 s irradiated, 1 s non-irradiated)

12.4 INVESTIGATION WITH AN PHOTOLUMINESCENCE SPECTROMETER WHILE UV LASER EXCITATION

The observation of the fading of the fluorescence with decreasing fluence lead to another test: maybe it is possible to determine the defect concentration, and therefore the fluence applied to irradiated crystals, by measuring the intensity of the fluorescence. This could be a promising, non-destructive analytical technique to quantify defect concentrations in calcite crystals produced by bombardment with heavy ions in the low fluence regime (<1×10^9 Au-ions/cm^2).

To check this method, the samples were investigated with a photoluminescence spectrometer to quantify the luminescence of the irradiated calcite. Subsequently, experiments with UV-stimulated Raman spectroscopy and photoluminescence (PL) were performed to test the luminescence response to UV stimulation. The experiments were performed with the UV-Raman and photoluminescence spectrometer (UV-laser: 244 nm) of Jobin Yvon Horiba. Calcite irradiated with 1×10^6 Au-ions/cm^2 (11.1 MeV/u) shows distinct photoluminescence with bands at about 520 and 545 nm (Fig. 12.9), which matches the greenish, yellowish color of the luminescence light whereas non-irradiated calcite crystals show only a minor peak at 545 nm. Increasing the fluence to 1×10^8 Au-ions/cm^2, the amplitude of both peaks increases (Fig. 12.9). All spectra are taken with the following parameters: grating 300, objective 40x, accumulation 2x, hole 50.

12.5 DISCUSSION

Summarizing the first results, UV-excitation combined with photoluminescence spectroscopy is sensitive enough to detect crystal defects created by heavy ions (11.1 MeV/u ^{197}Au) at a fluence as low as 1×10^6 ions/cm^2. Therefore in principle it should be possible to determine the fluence applied via excitation of the samples with UV light, but many more tests have to be done.

As observed so far, Raman spectroscopy and detection with the UV-excitation (Laser: 244 nm) did not reveal any fluence-related change of the Raman bands.

12.6 OUTLOOK

The next steps would be a detailed and more precise measurements of the fluorescence using the photoluminescence spectrometer to determine the exact frequency and the strength of the visible fluorescence. For this purpose, a series of calcite crystals has to be irradiated with increasing fluence.

Finally, tests with calcite crystals with high uranium content have to be performed, to check whether other natural samples besides the Terlingua calcite show similar reactions to excitation with UV light.

13

Final Conclusion

The following conclusions provide a summary of each chapter, with an emphasis on the most important results and recommendations of the author for possible continuations of the research.

The literature research revealed a vast number of studies dealing with the etching of carbonate minerals, some of them very old. These studies described numerous etching recipes for etching carbonate minerals, and in general, they provided crucial hints on how to approach the etching of carbonate minerals. The literature research of this study covered just a minor part of the literature available. For a complete summary of the literature a whole project is needed, which should be performed by a German native speaker, because most of this literature is written in old-fashioned German.

The new preparation method for the preparation of rocks or minerals without a natural cleavage turned out to be very useful and is fully suitable to prepare samples for ion irradiation. For future applications of the preparation method, further automation would be sensible, due to the limited scope of the present procedure.

The etching experiments with irradiated calcite crystals revealed two useful etching solutions: EDTA + 5 % acetic acid at 21 °C and 0.091 % HNO_3 at 15 °C. The obtained etch pits have a length of about 10 µm and a width of about 8 µm after etching with EDTA + 5 % acetic acid for 20 s, and a length of about 9 µm and a width of about 7 µm after etching with HNO_3 for 4 s. All revealed etch pits are very shallow, with a depth of about 300 nm. The developed etching procedure works for calcite only. The next steps would be to test the procedure for other carbonate minerals apart from dolomite and aragonite, which have been tested and found to be unsuitable for the calcite etching procedure.

The successful visualization of neutron induced tracks on a calcite surface marked a very important stage in this doctoral thesis. This experiment showed that it is generally possible to use calcite for fission-track dating if the uranium content of the sample is high enough. However, before the calcite can be used as a tool for fission-track dating, many preliminary problems have to be solved. For example, comprehensive experiments need to be done on annealing kinetics and the identification of non-induced fission tracks. Ideally, these tasks could be part of a follow-on project, for example a new doctoral thesis.

The reactions of irradiated calcite crystals to excitation with short wave UV light showed an unexpected result, which has various potential applications. Due to the fact that the green luminescence of the irradiated parts fades with decreasing fluence applied, quantifying this luminescence with a spectrometer could provide information about the fluence applied, and therefore about the amount of defects. The UV application has a lot of potential. It is very likely that from this discovery a complete new method of detecting defect concentrations in crystals could be developed; therefore the author strongly recommends performing detailed studies on this topic.

The new online Raman measurement system represents a powerful tool for characterizing irradiated matter with Raman spectroscopy. First experiments with calcite confirmed the functionality of the system by displaying changes in the Raman spectra of calcite, with its new band at 435 cm^{-1}, which are already known from offline experiments. Additionally, first successful tests with the anisotropic mineral malachite proved the advantages of in-situ Raman measurements of matter. The system now needs to be further developed in order to provide a straightforward measurement method at the M3-beamline, which can be used by various research groups to make diverse scientific data available.

In final conclusion, the main research objective was achieved, with the identification of two etching procedures to visualize ion-induced tracks in calcite. The second objective revealed two new approaches to characterizing minerals, or matter in general using non-destructive techniques. Of these, the online Raman spectroscopy represents a fully developed system which is ready to use. The third objective was fulfilled by developing many major and minor improvements to available procedures.

14

REFERENCES

Afarideh, H., Faghih Habibi, M., Hashemi, F., Shokouhi, F., 1993. Uranium content and age determination of various minerals of Iran. Nuclear Tracks and Radiation Measurements 22 (1–4), 753–756.

Alcaraz-Pelegrina, J.M., Martínez-Aguirre, A., 2007. U/Th dating of carbonate deposits from Constantina (Sevilla), Spain. Applied radiation and isotopes : including data, instrumentation and methods for use in agriculture, industry and medicine 65 (7), 798–804.

Andersen, M.B., Stirling, C.H., Potter, E.-K., Halliday, A.N., Blake, S.G., McCulloch, M.T., Ayling, B.F., O'Leary, M., 2008. High-precision U-series measurements of more than 500,000 year old fossil corals. Earth and Planetary Science Letters 265 (1-2), 229–245.

Baumhauer, H., 1894. Die Resultate der Aetzmethode in der krystallographischen Forschung, an einer Reihe von krystallisirten Körpern dargestellt. Verlag von Wilhelm Engelmann, Leipzig, 131 pp.

Becke, F., 1928. Gustav Tschermak zur Erinnerung. Mineralogische und Petrographische Mitteilungen 39 (1-2), I-X.

Bellemans, F., De, *Corte, F., Van, D., Haute, P.*, 1995. Composition of srm and cn u-doped glasses: Significance for their use as thermal neutron fluence monitors in fission track dating. Radiation Measurements 24 (2), 153–160.

Boos, A., 1942. Ätzversuche an Calcit, Rhodochrosit und Siderit. Neues Jahrbuch für Mineralogie 78 (Abt. A), 89–130.

Bragg, W.H., Bragg, W.L., 1913. The Reflection of X-rays by Crystals. Proceedings of the Royal Society of London. Series A 88 (605), 428–438.

Čejka, J., Sejkora, J., Jebavá, I., Xi, Y., Couperthwaite, S.J., Frost, R.L., 2013. A Raman spectroscopic study of the basic carbonate mineral callaghanite Cu2Mg2(CO3)(OH)6·2H2O. Spectrochimica acta. Part A, Molecular and biomolecular spectroscopy 108, 171–176.

Chang, L., Deer, W.A., Howie, R.A., Zussman, J., 1998. Rock-forming Minerals: Non-Silicates, Volume 5B. Geological Society.

Copeland, P., Watson, E.B., Urizar, S.C., Patterson, D., Lapen, T.J., 2007. Alpha thermochronology of carbonates. Geochimica et Cosmochimica Acta 71 (18), 4488–4511.

Cros, A., Gautheron, C., Pagel, M., Berthet, P., Tassan-Got, L., Douville, E., Pinna-Jamme, R., Sarda, P., 2014. 4He behavior in calcite filling viewed by (U–Th)/He dating, 4He diffusion and crystallographic studies. Geochimica et Cosmochimica Acta 125, 414–432.

Daniell, F., 1817. Ueber einige Erscheinungen, die den Auflösungsprozess begleiten. Schweiggers Journal für Chemie und Physik 19, 38–53.

Dawson, J.B., 1962. The geology of Oldoinyo Lengai. Bull Volcanol 24 (1), 349-387.

Dresselhaus, M.S., Dresselhaus, G., Jorio, A., Souza Filho, A.G., Saito, R., 2002. Raman spectroscopy on isolated single wall carbon nanotubes. Carbon 40 (12), 2043–2061.

Dresselhaus, M.S., Dresselhaus, G., Saito, R., Jorio, A., 2005. Raman spectroscopy of carbon nanotubes. Physics Reports 409 (2), 47–99.

Dresselhaus, M.S., Jorio, A., Souza Filho, A.G., Dresselhaus, G., Saito, R., 2002. Raman spectroscopy on one isolated carbon nanotube. Physica B: Condensed Matter 323 (1-4), 15–20.

Ebner, V.v., 1885. Die Lösungsflächen des Kalkspathes und des Aragonites: II. Die Ätzfiguren des Kalkspathes. III. Die Lösungsflächen des Aragonites. Sitzungsber.d. k. k. Akad. d.Wiss. Wien, Abtheilung 2, 91, 760–835.

Fleischer, R.L., Price, P.B., 1963a. Charged Particle Tracks in Glass. J. Appl. Phys. 34 (9), 2903.

Fleischer, R.L., Price, P.B., 1963b. Tracks of Charged Particles in High Polymers. Science 140 (3572), 1221–1222.

Fleischer, R.L., Price, P.B., Walker, R.M., 1975. Nuclear Tracks in Solids: Principles and Applications. University of California Press.

Fleitmann, D., Burns, S.J., Mudelsee, M., Neff, U., Kramers, J., Mangini, A., Matter, A., 2003. Holocene Forcing of the Indian Monsoon Recorded in a Stalagmite from Southern Oman. Science 300 (5626), 1737–1739.

Friedrich, W., Knipping, P., Laue, M., 1913. Interferenzerscheinungen bei Röntgenstrahlen. Annalen der Physik 346 (10), 971–988.

Frost, R.L., 2011. Raman spectroscopy of selected borate minerals of the pinakiolité group. J. Raman Spectrosc. 42 (3), 540–543.

Frost, R.L., Martens, W.N., Rintoul, L., Mahmutagic, E., Kloprogge, J.T., 2002. Raman spectroscopic study of azurite and malachite at 298 and 77 K. J. Raman Spectrosc. 33 (4), 252–259.

Gaft, M., Nagli, L., Panczer, G., Waychunas, G., Porat, N., 2008. The nature of unusual luminescence in natural calcite CaCO3. American Mineralogist 93 (1), 158–167.

Gunasekaran, S., Anbalagan, G., Pandi, S., 2006. Raman and infrared spectra of carbonates of calcite structure. J. Raman Spectrosc. 37 (9), 892–899.

Hoffmann, D.L., Spötl, C., Mangini, A., 2009. Micromill and in situ laser ablation sampling techniques for high spatial resolution MC-ICPMS U-Th dating of carbonates. Chemical Geology 259 (3-4), 253–261.

Holzkämper, S., Mangini, A., Spötl, C., Mudelsee, M., 2004. Timing and progression of the Last Interglacial derived from a high alpine stalagmite. Geophys. Res. Lett. 31 (7), n/a.

Honess, A.P., Jones, J.R., 1937. Etch Figure Investigations with optically Active Solvents. Bulletin of the Geological Society of America 48, 667–722.

Keith, R.E., Gilman, J.J., 1960. Dislocation etch pits and plastic deformation in calcite. Acta Metallurgica 8 (1), 1–10.

Kleber, W., 1938. Zum Mechanismus der Einkristallätzung mit optisch aktiven Substanzen. Zentralblatt der Mineralogie A, 294–301.

Klocke, F., 1878. Ueber die Aetzfiguren der Alaune. Zeitschrift für Krystallografie 2, 126.

Kluge, T., Marx, T., Scholz, D., Niggemann, S., Mangini, A., Aeschbach-Hertig, W., 2008. A new tool for palaeoclimate reconstruction: Noble gas temperatures from fluid inclusions in speleothems. Earth and Planetary Science Letters 269 (3-4), 408–415.

Köhler, A., 1925. Verzeichnis der Arbeiten F. Becke's nach Jahren geordnet. Mineralog. und petrogr. Mitt. 38 (1), VII-XIX.

Krishnaswami, S., Lal, D., Prabhu, N., Tamhane, A.S., 1971. Olivines: Revelation of Tracks of Charged Particles. Science (New York, N.Y.) 174 (4006), 287–291.

Kristjanson, L., 2002. Iceland spar: The Helgustadir Calcite Locality and its influence on the development of science. Journal of Geoscience education (50), 419–427.

Leydolt, F., 1855. Über eine neue Methode, die Structur und Zusammensetzung der Krystalle zu untersuchen, mit besonderer Berücksichtigung der Varietäten des rhomboedrischen Quarzes. Sitzungsber.d. k. k. Akad. d.Wiss. Wien 15, 59–81.

Macdougall, D., Price, P.B., 1974. Attempt to date early South african hominids by using fission tracks in calcite. Science (New York, N.Y.) 185 (4155), 943–944.

Malard, L.M., Pimenta, M.A., Dresselhaus, G., Dresselhaus, M.S., 2009. Raman spectroscopy in graphene. Physics Reports 473 (5-6), 51–87.

Okrusch, M., Matthes, S., 2010. Mineralogie Eine Einfuhrung In Die Spezielle Mineralogie, Petrologie Und Lagerstattenkunde. Springer.

Neff, U., 2001. Massenspektrometrische Th/U-Datierung von Höhlensintern aus dem Oman: Klimaarchive des asiatischen Monsuns. Ph. D. Thesis.

Niggemann, S., Mangini, A., Mudelsee, M., Richter, D.K., Wurth, G., 2003. Sub-Milankovitch climatic cycles in Holocene stalagmites from Sauerland, Germany. Earth and Planetary Science Letters 216 (4), 539–547.

Nohara, L.B., Petraconi Filho, G., Nohara, E.L.-s., Kleinke, M.-c.U., Rezende, M.C. Evaluation of carbon fiber surface treated by chemical and cold plasma processes. Materials Research 8, 281–286.

Nomarski, G., 1955. Nouveau dispositif pour l'observation en contraste de phase différentiel. Journal de Physique et Le Radium (16), 88.

Pabst, S., Burchard, M., Glasmacher, U.A., Miletich, R., Neumann, R.:, Schuster, B.: Trautmann, C., 2011. Radiation damage in heavy ion-irradiated carbonate minerals investigated by Raman and infrared spectroscopy, in: Scientific Report 2010. GSI Helmholtzzentrum für Schwerionenforschung, Darmstadt, p. 379.

Picht, O., 2010. Growth and characterization of bismuth telluride nanowires. Heidelberg, Univ., Diss.

Price, P.B., Fleischer, R.L. Identification of Energetic Heavy Nuclei With Solid Dielectric Track Detectors: Applications to Astrophysical and Planetary Studies.

Price, P.B., Walker, R.M., 1962a. A new track detector for heavy particle studies. Physics Letters 3 (3), 113–115.

Price, P.B., Walker, R.M., 1962b. Observations of Charged-Particle Tracks in Solids. Journal of Applied Physics 33 (12), 3400–3406.

Reich, S., Thomsen, C., 2004. Raman spectroscopy of graphite. Philosophical transactions. Series A, Mathematical, physical, and engineering sciences 362 (1824), 2271–2288.

Rutt, H.N., Nicola, J.H., 1974. Raman spectra of carbonates of calcite structure. Journal of Physics C: Solid State Physics 7 (24), 4522–4528.

Saito, R., Jorio, A., Souza Filho, A.G., Grueneis, A., Pimenta, M.A., Dresselhaus, G., Dresselhaus, M.S., 2002. Dispersive Raman spectra observed in graphite and single wall carbon nanotubes. Physica B: Condensed Matter 323 (1-4), 100–106.

Scheidegger, Y., Kluge, T., Kipfer, R., Aeschbach-Hertig, W., Wieler, R., 2008. Paleotemperature reconstruction using noble gas concentrations in speleothem fluid inclusions. PAGES News (16), 10–12.

Schiedt, B., 2007. Characterization and application of ion track-etched nanopores. Dissertation.

Scholz, D., Mühlinghaus, C., Mangini, A., 2009. Modelling δ13C and δ18O in the solution layer on stalagmite surfaces. Geochimica et Cosmochimica Acta 73 (9), 2592–2602.

Schweizer, V., Grotzinger, J., Jordan, T.H., Press, F., Siever, R., 2007. Press/Siever - Allgemeine Geologie. Spektrum Akademischer Verlag.

Sippel, R.F., Glover, E.D., 1964. Fission Damage in Calcite and the Dating of Carbonates. Science (New York, N.Y.) 144 (3617), 409–411.

Spötl, C., Mangini, A., 2002. Stalagmite from the Austrian Alps reveals Dansgaard–Oeschger events during isotope stage 3. Earth and Planetary Science Letters 203 (1), 507–518.

Thomas, J. M., Renshaw, G. D., 1965. Dislocations in calcite and some of their chemical consequences. Trans. Faraday Soc. 61 (0), 791–796.

Thomsen, C., Reich, S., 2007. Raman Scattering in Carbon Nanotubes, in: Cardona, M., Merlin, R. (Eds.), Light Scattering in Solid IX, vol. 108. Springer Berlin Heidelberg, pp. 115-234.

Wagner, G., Van den Haute, Peter, 1992. Fission track dating. Kluwer Academic Publishers.

Wang, N., Cao, X., Cai, X., Xu, Y., Guo, L., 2010. Porous cuprite films: facile solution deposition and their application for nitrite sensing. The Analyst 135 (8), 2106–2110.

Wondratschek, H., 1971. Will Kleber, Nachruf. Fortschritte der Mineralogie 48 (2), 175.

Zaitsev, A.N., Keller, J., 2006. Mineralogical and chemical transformation of Oldoinyo Lengai natrocarbonatites, Tanzania. Peralkaline Rocks A special issue dedicated to Henning Sørensen PERALK2005 Workshop 91 (1–4), 191–207.

Ziegler, J.F., Ziegler, M.D., Biersack, J.P., 2010. SRIM – The stopping and range of ions in matter (2010). Nuclear Instruments and Methods in Physics Research Section B: Beam Interactions with Materials and Atoms 268 (11–12), 1818–1823.

15

APPENDIX

APPENDIX

15.1 List of Figures

15.2 LIST OF TABLES

15.3 COPYRIGHT OF PHOTOS & SKETCHES NOT PRODUCED BY THE AUTHOR

3.1	Martin Okrusch, Siegfried Matthes, 2010. Mineralogie Eine Einführung In Die Spezielle Mineralogie, Petrologie Und Lagerstättenkunde. Springer.
3.3	Public domain
3.4	Bundesanstalt für Geowissenschaften und Rohstoffe, D-Hannover (2004) Grundlage: Geologische Karte der Bundesrepublik Deutschland 1:1000000, A. VOGES et al.; 1993
3.5	Photo by Immanuel Giel http://commons.wikimedia.org/wiki/File:White_Cliffs_of_Dover_02.JPG
3.9	Photo by GSI Helmholtzzentrum für Schwerionenforschung, C. Grau
3.10	Photo: GSI Helmholtzzentrum für Schwerionenforschung, a) GSI Helmholtzzentrum für Schwerionenforschung
5.8	Witec

15.4 LIST OF ALL SAMPLES USED IN THIS STUDY

Tab. 15-1 shows all samples used for this thesis.

Etching Series	Mineral	Sample Number	Etchant	Concentration	Temperature [°C]	Time (max etched) [s]	Ion	Fluence [ions/cm²]	Energy [MeV/u]	Sonstiges
1	Dolomite	Dol-I-2b	NaOH	saturated	20	3600	Au	10^7	11.1	
2	Calcite	CC-I-13e	NaOH	10 mol	20	450	Au	10^6	11.1	
3	Calcite	CC-I-13f	NaOH	10 mol	20	450	Au	10^6	11.1	
4	Calcite	CC-I-13g	NaOH	10 mol	20	180	Au	10^6	11.1	
5	Calcite	CC-I-13h	NaOH	10 mol	20	180	Au	10^6	11.1	
6	Calcite	CC-I-13i	NaOH	10 mol	20	600	Au	10^6	11.1	
7	Calcite	CC-I-13j	NaOH	10 mol	20	600	Au	10^6	11.1	
8	Calcite	Cc-I-13k	NaOH	10 mol	20	270	Au	10^6	11.1	afterwards etching with EDTA + 5 % Acetic Acid
9	Calcite	Cc-13l	EDTA + Acetic Acid	5%	20	20	Au	10^6	11.1	
10	Calcite	CC-13m	NaOH	12 mol	20	450	Au	10^6	11.1	
11	Calcite	CC-13n	NaOH	10 mol	20	1200	Au	10^6	11.1	
12	Calcite	CC-13o	NaOH	10 mol	20	600	Au	10^6	11.1	
13	Calcite	LZ-1	NaOH	10 mol	RT	66 h	XXX	XXX	XXX	Longterm experiment
14	Calcite	LZ-2	EDTA + Acetic Acid	5%	RT	66 h	XXX	XXX	XXX	Longterm experiment
15	Calcite	CC-13p	EDTA + Acetic Acid	5%	25	15	Au	10^6	11.1	
16	Calcite	CC-13q	EDTA + Acetic Acid	1%	22	10	Au	10^6	11.1	
17	Calcite	Cc-I-13t	EDTA + Acetic Acid	1%	22,5	10	Au	10^6	11.1	
18	Aragonite	Ar-II-4	EDTA + Acetic Acid	1%	20	180	Au	10^7	11.1	
19	Dolomite	Dol-I-9c	EDTA + Acetic Acid	1%	21	60	Au	10^6	11.1	
20	Calcite	XXX	EDTA + Acetic Acid	5%	RT	20	Au	10^6	11.1	no result due to bad preperation
21	Calcite	Cc-I-13r	EDTA + Acetic Acid	5%	20,4	20	Au	10^6	11.1	Series 1 (Chapter 5)
22	Calcite	Cc-I-13r2	EDTA + Acetic Acid	4%	20,3	20	Au	10^6	11.1	Series 1 (Chapter 5)
23	Calcite	Cc-I-13r3	EDTA + Acetic Acid	3%	21	20	Au	10^6	11.1	Series 1 (Chapter 5)
24	Calcite	Cc-I-13r4	EDTA + Acetic Acid	2%	20,9	20	Au	10^6	11,1	Series 1 (Chapter 5)
25	Calcite	Cc-I-13r5	EDTA + Acetic Acid	1%	21,2	20	Au	10^6	11.1	Series 1 (Chapter 5)
26	Calcite	Cc-I-13r6	EDTA + Acetic Acid	0,50%	21,1	20	Au	10^6	11.1	Series 1 (Chapter 5)

Tab. 15-1: Samples used in this study

Etching Series	Mineral	Sample Number	Etchant	Concentration	Temperature [°C]	Time (max etched) [s]	Ion	Fluence [ions/cm²]	Energy [MeV/u]	Sonstiges
27	Calcite	Cc-I-13s	EDTA + Acetic Acid	0%	20,7	20	Au	10^6	11.1	Series 1 (Chapter 5)
28	Calcite	Cc-I-13t	EDTA + Acetic Acid	0%	20,8	20	Au	10^6	11.1	Series 2 (Chapter 5)
29	Calcite	Cc-I-13u	EDTA + Acetic Acid	0,50%	20,3	20	Au	10^6	11.1	Series 2 (Chapter 5)
30	Calcite	Cc-I-13v	EDTA + Acetic Acid	1%	20,6	20	Au	10^6	11.1	Series 2 (Chapter 5)
31	Calcite	Cc-I-13w	EDTA + Acetic Acid	2%	19,8	20	Au	10^6	11.1	Series 2 (Chapter 5)
32	Calcite	Cc-I-13x	EDTA + Acetic Acid	2.5%	20,6	20	Au	10^6	11.1	Series 2 (Chapter 5)
33	Calcite	Cc-I-13y	EDTA + Acetic Acid	3%	21	20	Au	10^6	11.1	Series 2 (Chapter 5)
34	Calcite	Cc-I-13z	EDTA + Acetic Acid	3.5%	20,6	20	Au	10^6	11.1	Series 2 (Chapter 5)
35	Calcite	Cc-I-13aa	EDTA + Acetic Acid	4%	20,6	20	Au	10^6	11.1	Series 2 (Chapter 5)
36	Calcite	Cc-I-13ab	EDTA + Acetic Acid	5%	20,4	20	Au	10^6	11.1	Series 2 (Chapter 5), Sputtered with Gold for REM
37	Calcite	Cc-I.8a	EDTA + Acetic Acid	5%	20,4	15	U	10^7	11.1	
38	Calcite	Cc-A	EDTA + Acetic Acid	5%	20,5	20	XXX	XXX	XXX	
39	Calcite	Cc-B-1	EDTA + Acetic Acid	5%	20,7	0	XXX	XXX	XXX	Exploded during heating experiment
40	Calcite	Cc-I-8b	EDTA + Acetic Acid	5% in 1:10 dillution	20,6	3600	U	10^7	11.1	
41	Calcite	Cc-WI-1	EDTA + Acetic Acid	5%	20,5	15	XXX	XXX	XXX	from Wismut AG
42	Calcite	Cc-B-2	EDTA + Acetic Acid	5%	20,7	20	XXX	XXX	XXX	
43	Calcite	Cc-B-3	EDTA + Acetic Acid	5%	20,7	20				
44	Calcite	Cc-WI-2	EDTA + Acetic Acid	5%	20,1	5	XXX	XXX	XXX	from Wismut for first experiments with natural Uranium content
45	Calcite	Cc-WI-3	EDTA + Acetic Acid	5%	20,1	5	XXX	XXX	XXX	from Wismut for first experiments with natural Uranium content
46	Calcite	Cc-WI-4	EDTA + Acetic Acid	5%	20,1	5	XXX	XXX	XXX	from Wismut for first experiments with natural Uranium content
47	Calcite	Cc-WI-5	EDTA + Acetic Acid	5%	20,1	5	XXX	XXX	XXX	from Wismut for first experiments with natural Uranium content
48	Calcite	Cc-B-4	EDTA + Acetic Acid	5%	20,1	20	XXX	XXX	XXX	heated: 200°C for 100h
49	Calcite	Cc-I-13ac	EDTA + Acetic Acid	5%	20,5	20	Au	10^6	11.1	heated: 400°C for 100h
50	Calcite	Cc-B-5	EDTA + Acetic Acid	5%	20,1	20	XXX	XXX	XXX	heated: 400°C for 100h

Continuation of Table 3-5: Samples used in this study

Etching Series	Mineral	Sample Number	Etchant	Concentration	Temperature [°C]	Time (max etched) [s]	Ion	Fluence [ions/cm^2]	Energy [MeV/u]	Sonstiges
51	Calcite	Cc-I-13ad1	EDTA + Acetic Acid	5%	20,4	20	Au	10^6	11.1	heated: 200°C for 100h
52	Calcite	Cc-I-13 ad2	EDTA + Acetic Acid	5%	20,1	20	Au	10^6	11.1	Reference for ES 53 (bad)
53	Calcite	Cc-I-13 ae1	EDTA + Acetic Acid	5%	20,1	20	Au	10^6	11.1	heated: 500°C for 100h
54	Calcite	Cc-I-13 ae2	EDTA + Acetic Acid	5%	20,1	5	XXX	XXX	XXX	Reference for ES 53
55	Calcite	Cc-I-10a	EDTA + Acetic Acid	5%	20,4	20	Au	10^6	11.1	heated: 300°C for 100h
56	Calcite	Crystal lost before etching								
57	Calcite	Cc-I-17	EDTA + Acetic Acid	5%	20,4	20	Au	107	11.1	
58	Calcite	Crystal lost before etching								
59	Calcite	Cc-D	EDTA + Acetic Acid	5%	20,1	5	XXX	XXX	XXX	
60	Calcite	Cc-I-13af	HNO_3	10%	20,4	15	Au	10^7	11.1	
61	Calcite	Cc-I-13ag	EDTA + Acetic Acid	5%	20,4	20	Au	10^6	11.1	heated: 220°C for 100h
62	Calcite	Cc-I-13ah	EDTA + Acetic Acid	5%	20,4	20	Au	10^6	11.1	heated: 240°C for 100h
63	Calcite	Cc-I-13ai	EDTA + Acetic Acid	5%	20,4	20	Au	10^6	11.1	heated: 260°C for 100h
64	Calcite	Cc-I-13aj	EDTA + Acetic Acid	5%	20,4	20	Au	10^6	11.1	heated: 280°C for 100h
65	Calcite	Cc-IV-4	EDTA + Acetic Acid	5%	20,4	20	Au	10^6	11.1	Test with sawed crystalls
66	Calcite	Cc-IV-5	EDTA + Acetic Acid	5%	20,4	20	Au	10^7	11.1	Test with sawed crystalls
67	Calcite	Cc-I-10	EDTA + Acetic Acid	5%	20,4	20	Au	10^6	11.1	Dirt Test
68	Calcite	Wi-5	EDTA + Acetic Acid	5%	20,4	10	XXX	XXX	XXX	
69	Calcite	Cc-VI	EDTA + Acetic Acid	5%	20,4	20	Au	10^8	11.1	
70	Calcite	Cc-S1-I	EDTA + Acetic Acid	5%	20,4	20	Au	10^8	11.1	
71	Calcite	CC_S1_II	EDTA + Acetic Acid	5%	20,4	20	Au	10^8	11.1	
72	Calcite	Cc_VII_6	EDTA + Acetic Acid	5%	RT	20	Au	10^6	11.1	First test with embedded Samples
73	Calcite	Cc_V_12	EDTA + Acetic Acid	5%	RT	5	Au	10^6	11.1	
74	Calcite	Cc_V_14	HNO_3	0,91%	RT	15	Au	10^6	11.1	
75	Does not exist									
76	Calcite	Cc_V_13	HNO_3	0,91%	RT	3	Au	10^6	11.1	
77	Calcite	Cc_V_11	HNO_3	0,091%	RT	5	Au	10^6	11.1	
78	Calcite	Cc_V_24	HNO_3	0,91%	21	8	Au	10^6	11.1	HNO_3 Experiments, bad crystall Experiment repeated in ES 84

Continuation of Table 3-5: Samples used in this study

Etching Series	Mineral	Sample Number	Etchant	Concentration	Temperature [°C]	Time (max etched) [s]	Ion	Fluence [ions/cm²]	Energy [MeV/u]	Sonstiges
79	Calcite	Cc_V_26a	HNO_3	0,091%	21	8	Au	10^6	11.1	HNO_3 Experiments
80	Calcite	Cc_V_21	HNO_3	0,009%	21	8	Au	10^6	11.1	HNO_3 Experiments
81	Calcite	Cc_V_25a	HNO_3	0,91%	15	8	Au	10^6	11.1	HNO_3 Experiments
82	Calcite	Cc_V_25b	HNO_3	0,091%	15	8	Au	10^6	11.1	HNO_3 Experiments
83	Calcite	Cc_V_20	HNO_3	0,009%	15	8	Au	10^6	11.1	HNO_3 Experiments
84	Calcite	Cc_IV_28	HNO_3	0,91%	21	8	Au	10^6	11.1	HNO_3 Experiments
85	Carbonatite	FuR2a	HNO_3	0,091%	15	12	Au	10^6	11.1	
86	Calcite	Cc_V_44	HNO_3	0,091%	15	4	Au	10^6	11.1	
87	Calcite	Cc_V_117	HNO_3	0,091%	15	4	Au	10^6	11.1	Angle irradiation
88	Carbonatite	WiRe 1	HNO_3	0,091%	15	4	XXX	XXX	XXX	Etching for FRM II experimet
89	Carbonatite	WiRe 3	HNO_3	0,091%	15	8	XXX	XXX	XXX	Etching for FRM II experimet
90	Carbonatite	WiRe 2	HNO_3	0,091%	15	8	XXX	XXX	XXX	Etching for FRM II experimet
91	Carbonatite	BRRE 1	HNO_3	0,091%	15	8	XXX	XXX	XXX	Etching for FRM II experimet
92	Carbonatite	KaRe1	HNO_3	0,091%	15	4	XXX	XXX	XXX	Etching for FRM II experimet
93	Carbonatite	FuS1	HNO_3	0,091%	15	4	XXX	XXX	XXX	Etching for FRM II experimet
94	Carbonatite	FUR1	HNO_3	0,091%	15	4	XXX	XXX	XXX	Etching for FRM II experimet
95	Calcite	ZKE 2	HNO_3	0,091%	15 °C	2	XXX	XXX	XXX	ZKE 2
96	Calcite	Cc-0912-x	HNO_3	0,091%	15 °C	4	Au	10^6	11.1	Test for 95
97	Calcite	CC-TC-II	EDTA + Acetic Acid	5%	21	20	Au	10^6	11.1	Test for 98, crystall lost
98	Calcite	CC-ZKE-I	EDTA + Acetic Acid	5%	21	15	XXX	XXX	XXX	
99	Calcite	Testcc	HNO_3	0,091%	15	2	Au	10^6	11.1	Test for 100
100	Calcite	CC-ZKE G4	HNO_3	0,091%	15	2	XXX	XXX	XXX	
101	Malachite	Ma 1	HNO_3	0,091%	15	10	Au	10^6	11.1	
102	Calcite	CC_v_53	HCl	1,000%	RT	30	Au	10^6	11.1	
103	Calcite	CC_V_52a	Ch_2O_2	10,000%	RT	30	Au	10^6	11.1	
104	Foil	SD_0912_ XII	NaOH	6m	50	50	Au	10^6	11.1	
105	Calcite	CC_V_53b	EDTA + Acetic Acid	5,000%	21	20	Au	10^6	11.1	Corresponding crystal to 104
106	Calcite	Cc_VI_31	HNO_3	0.091%	21	4	Au	10^6	11.1	

Continuation of Table 3-5: Samples used in this study

Etching Series	Mineral	Sample Number	Etchant	Concentration	Temperature [°C]	Time (max etched) [s]	Ion	Fluence [ions/cm²]	Energy [MeV/u]	Sonstiges
107	Calcite	Cc_V_30	HNO_3	0.091%	21	4	Au	10^6	11.1	
108	Calcite	Cc_V_39	HNO_3	0.091%	21	4	Au	10^6	11.1	
109	Calcite	Cc_V_41	HNO_3	0.091%	21	8	Au	10^6	11.1	
110	Calcite	Cc_V_56	HNO_3	0.091%	15	4	Au	10^6	11.1	Irradiated under 15°
111	Calcite	Cc_V_75	HNO_3	0.091%	15	4	Au	10^6	11.1	Irradiated under 45°
112	Calcite	Cc_V_57	HNO_3	0.091%	15	4	Au	10^6	11.1	Irradiated under 15°
113	Dolomite	Dol_Bal	EDTA + Acetic Acid	5%	21	20	Au	10^6	11.1	

15.5 SAMPLE USED IN THE ANNEALING EXPERIMENTS

Tab. 15-2: Samples used in the annealing experiments.

Etching Series	Ion	Fluence [Ions/cm^2]	Energy [MeV/u]	dE/dx [keV/µm]	Proj. Range [µm]	Etching solvent	Etching Times [s]	Annealing Temp. [°C]
31	^{197}Au	10^6	11,1	24,5	94	EDTA + 5% Acetic Acid	5, 10, 15, 20	not annealed
36	^{197}Au	10^6	11,1	24,5	94	EDTA + 5% Acetic Acid	5, 10, 15, 20	not annealed
43	N.I.	N.I.	N.I.	N.I.	N.I.	EDTA + 5% Acetic Acid	5, 10, 15, 20	not annealed
51	^{197}Au	10^6	11,1	24,5	94	EDTA + 5% Acetic Acid	5, 10, 15, 20	200
48	N.I.	N.I.	N.I.	N.I.	N.I.	EDTA + 5% Acetic Acid	5, 10, 15, 20	200
61	^{197}Au	10^6	11,1	24,5	94	EDTA + 5% Acetic Acid	5, 10, 15, 20	220
62	^{197}Au	10^6	11,1	24,5	94	EDTA + 5% Acetic Acid	5, 10, 15, 20	240
63	^{197}Au	10^6	11,1	24,5	94	EDTA + 5% Acetic Acid	5, 10, 15, 20	260
64	^{197}Au	10^6	11,1	24,5	94	EDTA + 5% Acetic Acid	5, 10, 15, 20	280
55	^{197}Au	10^6	11,1	24,5	94	EDTA + 5% Acetic Acid	5, 10, 15, 20	300
49	^{197}Au	10^6	11,1	24,5	94	EDTA + 5% Acetic Acid	5, 10, 15, 20	400
50	N.I.	N.I.	N.I.	N.I.	N.I.	EDTA + 5% Acetic Acid	5, 10, 15, 20	400
53	^{197}Au	10^6	11,1	24,5	94	EDTA + 5% Acetic Acid	5, 10, 15, 20	500
54	N.I.	N.I.	N.I.	N.I.	N.I.	EDTA + 5% Acetic Acid	5	500

15.6 GEOCHEMISTRY OF CALCITE

Tab. 15-3: Geochemical analysis of the used calcite

Analyte	SiO_2	Al_2O_3	Fe_2O_3	MgO	CaO	Na_2O	K_2O	TiO_2	P_2O_5	MnO	Cr_2O_3	Ni	Sc
Unit	%	%	%	%	%	%	%	%	%	%	%	µg/g	µg/g
MDL	0,01	0,01	0,04	0,01	0,01	0,01	0,01	0,01	0,01	0,01	0,002	20	1
Calcite Sample 1	<0.01	<0.01	<0.04	0,45	58,63	<0.01	<0.01	<0.01	<0.01	0,02	<0.002	<20	<1
Calcite Sample 2	<0.01	<0.01	<0.04	<0.01	58,08	<0.01	<0.01	<0.01	<0.01	0,04	<0.002	<20	<1

Analyte	LOI	Sum	Ba	Be	Co	Cs	Ga	Hf	Nb	Rb	Sn	Sr	Ta
Unit	%	%	µg/g	µg/g	µg/g	µg/g	µg/g	µg/g	µg/g	µg/g	µg/g	µg/g	µg/g
MDL	-5,1	0,01	1	1	0,2	0,1	0,5	0,1	0,1	0,1	1	0,5	0,1
Calcite Sample 1	40,9	99,95	3	<1	<0.2	<0.1	<0.5	<0.1	<0.1	<0.1	<1	175,8	<0.1
Calcite Sample 2	41,9	99,97	2	<1	<0.2	<0.1	<0.5	<0.1	<0.1	<0.1	<1	157,8	<0.1

Analyte	Th	U	V	W	Zr	Y	La	Ce	Pr	Nd	Sm	Eu	Gd
Unit	µg/g	µg/g	µg/g	µg/g	µg/g	µg/g	µg/g	µg/g	µg/g	µg/g	µg/g	µg/g	µg/g
MDL	0,2	0,1	8	0,5	0,1	0,1	0,1	0,1	0,02	0,3	0,05	0,02	0,05
Calcite Sample 1	<0.2	<0.1	<8	1,0	<0.1	0,7	1,9	2,3	0,23	1,1	0,14	0,05	0,16
Calcite Sample 2	<0.2	<0.1	<8	0,7	<0.1	2,4	6,7	8,3	0,81	2,9	0,38	0,14	0,41

Analyte	Tb	Dy	Ho	Er	Tm	Yb	Lu	TOT/C	TOT/S	Mo	Cu	Pb	Zn
Unit	µg/g	µg/g	µg/g	µg/g	µg/g	µg/g	µg/g	%	%	µg/g	µg/g	µg/g	µg/g
MDL	0,01	0,05	0,02	0,03	0,01	0,05	0,01	0,02	0,02	0,1	0,1	0,1	1
Calcite Sample 1	0,02	0,17	<0.02	0,07	<0.01	<0.05	0,01	13,58	<0.02	<0.1	0,1	0,3	<1
Calcite Sample 2	0,06	0,24	0,05	0,13	0,02	0,11	0,01	13,50	<0.02	<0.1	0,1	0,3	<1

Analyte	Ni	As	Cd	Sb	Bi	Ag	Au	Hg	Tl	Se
Unit	µg/g	µg/g	µg/g	µg/g	µg/g	µg/g	ng/g	µg/g	µg/g	µg/g
MDL	0,1	0,5	0,1	0,1	0,1	0,1	0,5	0,01	0,1	0,5
Calcite Sample 1	<0.1	0,6	<0.1	<0.1	<0.1	1,0	1,8	0,02	<0.1	<0.5
Calcite Sample 2	1,0	1,1	<0.1	<0.1	<0.1	<0.1	0,7	0,02	<0.1	<0.5

15.7 LIST OF ABSTRACTS & PUBLICATIONS

15.7.1 Publications

GSI Scientific Reports:

Dedera, S., Glasmacher, U.A., Burchard, M., Trautmann, C., 2012. Annealing of dislocations and heavy-ion-induced tracks in calcite, in: Scientific Report 2011, 2012-1. GSI Helmholtzzentrum für Schwerionenforschung, Darmstadt, p. 689.

Dedera, S., Glasmacher, U.A., Burchard, M., Trautmann, C., 2012. Etching of heavy ion tracks in calcite, in: Scientific Report 2011, 2012-1. GSI Helmholtzzentrum für Schwerionenforschung, Darmstadt, p. 689.

Dedera, S., Glasmacher, U.A., Burchard, M., Trautmann, C., 2013. Optimized etching of swift heavy ion tracks in calcite, in: Scientific Report 2012, 2013-1. GSI Helmholtzzentrum für Schwerionenforschung, Darmstadt, pp. 400 p.

Dedera, S., Schöppner, N., Glasmacher, U.A., Burchard, M., Trautmann, C., 2014. New approach to investigate irradiated calcite crystals – UV Raman and Photoluminescence with UV excitation, in: Scientific Report 2013, 2014-1. GSI Helmholtzzentrum für Schwerionenforschung, Darmstadt.

Dedera, S., Glasmacher, U.A., Burchard, M., Trautmann, C., *Bender, M., Severin, D*., 2015. Installation of in-situ Raman measurements at the M-Branch, in: Scientific Report 2014, 2015-1. GSI Helmholtzzentrum für Schwerionenforschung, Darmstadt.

Dedera, S., Schöppner, N., Glasmacher, U.A., Burchard, M., Trautmann, C., *Bender, M., Severin*, D., 2015. First Results of in-situ Raman measurements of ion-irradiated calcite, in: Scientific Report 2014, 2015-1. GSI Helmholtzzentrum für Schwerionenforschung, Darmstadt.

15.7.2 Submitted Manuscripts

Submitted to NIM-B, Shim 2015 Proceedings

Technical Specifications of an Online Raman Measurements System

Sebastian Dedera[1], Michael Burchard[1], Ulrich A. Glasmacher[1], Christina Trautmann[2,3], Daniel Severin[2], Markus Bender[2]

[1] Institute of Earth Sciences, University of Heidelberg Im Neuenheimer Feld 234, 69120 Heidelberg
[2] GSI Helmholtzzentrum für Schwerionenforschung Planckstrasse 1, D-64291 Darmstadt, Germany
[3] Materials Science Divisions, TU Darmstadt, Alarich-Weiss-Straße 2, 64287 Darmstadt, Germany

Abstract

A new online Raman system has been developed and tested for the irradiation of matter with swift heavy ions at the M-branch of the UNILAC at GSI (GSI Helmholtzzentrum für Schwerionenforschung) Darmstadt. The system consists of a Raman spectrometer, a 532 nm laser system, a confocal head, and a unit located inside of the 400 mm diameter spectroscopy chamber (M3-branch) consisting of a sample holder with an 50x objective. Successful measurements with the new systems have been performed on calcite ($CaCO_3$) crystals while irradiation with Au-ions, in which the mineral could be measured at the same spot for all fluences. This prevents the measurements of being affected by anisotropic effects, which can lead to wrong data especially for measurements of anisotropic crystals or materials such as malachite $Cu_2CO_3(OH)_2$. The Raman spectra show a new peak at 435 cm^{-1} for calcite above fluences of 1×10^{10} ions/cm^2.

Submitted to NIM-B, Shim 2015 Proceedings

Online Raman Measurements of Calcite and Malachite During irradiation with Swift Heavy Ions

Sebastian Dedera[1], Michael Burchard[1], Ulrich A. Glasmacher[1], Nicole Schöppner[1], Christina Trautmann[2,3], Daniel Severin[2]

[1] Institute of Earth Sciences, University of Heidelberg Im Neuenheimer Feld 234 69120 Heidelberg
[2] GSI Helmholtzzentrum für Schwerionenforschung, Planckstrasse 1, D-64291 Darmstadt, Germany
[3] Materials Science Divisions, TU Darmstadt, Alarich-Weiss-Straße 2,64287 Darmstadt, Germany

Abstract

A new online Raman System, which was installed at M3-beamline at the UNILAC, GSI Helmholtzzentrum für Schwerionenforschung Darmstadt was used for first spectroscopic measurements. Calcite and malachite samples have been irradiated in steps between 1×10^{9} ions/cm^{2} and 1×10^{12} ions/cm^{2} with Au ions (calcite) and Bi ions (malachite) at an energy of 4.8 MeV/u. Calcite revealed a new Raman band at 435 cm^{-1} and change of the half height width for the 1087 cm^{-1} Raman band.

The Raman bands of malachite change significantly with increasing fluence. Up to a fluence of 7×10^{10} ions/cm^{2}, all existing bands decrease in intensity. Between 8×10^{10} ions/cm^{2} and 1×10^{11} ions/cm^{2} a broad Cu_2O-band between 110 cm^{-1} and 220 cm^{-1} occur, which superimposes the pre-existing Raman bands. Additionally, a new broad band between 1000 cm^{-1} and 1750 cm^{-1} is formed, which is interpreted as a carbon coating, such as graphene or single-walled carbon nanotubes. In contrast to the Cu_2O-band, the carbon band vanished through further irradiation of the sample.

15.7.3 Abstracts

Workshop Ionenstrahlen und Nanostrukturen Augsburg 2012

Visualization von Schwerionenspuren in Kalzit mittels Ätzen

Dedera, S [1]., Glasmacher, U.A [1]., Burchard, M.[1], Trautmann C.[2],
[1]Institut für Geowissenschaften, Universtität Heidelberg, [2]GSI Darmstadt

Karbonatminerale wie zum Beispiel Kalzit ($CaCO_3$) sind in der Natur in großen Mengen vorhanden, etwa in Karbonatgesteinen. Das Lösungsverhalten von Karbonatmineralen setzt sich aus der Ätzrate von ungestörter Kristalloberfläche, der Ätzrate entlang von Dislokationen und der Ätzrate durch den Zerfall von ^{238}U entstandenen Spaltspuren zusammen. Da die Anzahl der Spaltspuren eine Funktion vom Urangehalt und Zeit sind, stellt die Ätzrate von Spaltspuren einen wichtigen Baustein im generellen Verständnis für das Lösungsverhalten von Kalzit dar. Desweiteren sind weder Dislokationen noch Spaltspuren gleichmäßig im Kristall verteilt. Diese Inhomogenität kann zu selektiver Lösung von Kalziten und damit von Karbonatgestein in der Natur führen.

Da der Urangehalt von natürlichem Kalzit stark variiert und somit die natürlichen Ionenspuren inhomogen im Kristall verteilt sind, wurden die Kristalle im UNILAC, GSI Darmstadt mit Schwerionen bestrahlt. Es wurden Fluenzen von 10^6 ^{238}U ions/cm^2 und 10^6, 10^7 und 10^8 ^{197}Au ions/cm^2 mit Energien von 4,8 und 11,1 MeV/u angelegt. Um die künstlich erzeugten Spuren eindeutig zu identifizieren wurden vor der Bestrahlung hexagonale Waben auf den Kristallen befestigt um bestrahlte und nicht bestrahlte Zonen auf den Kristallen zu erzeugen.

Folgende Ätzlösungen wurden getestet: Ameisensäure (CH_2O_2), Natronlauge (NaOH), Salzsäure (HCl), Salpetersäure (HNO_3) und Na—Ethylenediaminetetraacetic (EDTA) + 0,5-5% Essigsäure im Verhältnis 1:1. Experimente ergaben, dass Na-Ethylenediaminetetraacetic acid (EDTA) + 0,5-5% Essigsäure im Verhältnis 1:1 für 20 s die brauchbarste Ätzlösung ist. Die Ätzgruben zeigen lineares Wachstum und haben eine pseudohexagonale Form. Die Flächendichte der Ätzgruben auf den Kristallen entspricht der angewandten Fluenz. Experimente mit stark verdünnten Ätzlösungen (1:10) ergaben, dass sich die Form und Größe von Ätzgruben durch Verdünnung der Ätzlösungen kontrollieren lassen.

Kontrollätzungen von unbestrahlten Kristallen und Ausheilexperimente zeigen, dass man Baufehler und Spaltspuren in Kalzitkristallen an ihren unterschiedlichen Ausheilungsverhalten unterscheiden kann. Nach 100 h bei 260 °C zeigen die geätzten Oberflächen der Kalzite, dass Defekte hervorgerufen durch Bestrahlungen bei 260 °C für 100 h ausheilen, wohingegen Baufehler der Kristalle immer noch ätzbar sind.

Swift Heavy ions in Matter (SHIM) Kyoto 2012

Visualization of heavy ion tracks in calcite by etching techniques

Dedera, S.[1], Burchard, M.[1], Glasmacher, U.A.[1], Trautmann, C.,[2,3]
[1] University of Heidelberg, [2] Technical University Darmstadt, [3] GSI Darmstadt,

Carbonate minerals, for example calcite, dolomite or aragonite contain uranium in small amount which leads to damages in the crystal lattice due to the decay of the uranium isotopes. This study aims to visualize these damages and to describe and quantify them. To develop the etching techniques natural calcite crystals were irradiated with 10^6 ^{197}Au ions/cm^2 of 11.1 MeV/u at the UNILAC, GSI Darmstadt. Prior to the experiment the surface of calcite crystals was covered with a hexagonal mask to create irradiated and non-irradiated areas. Experiments showed that reproducible results are achieved with Na-Ethylenediaminetetraacetic acid (EDTA) + 0.5- 5% Acetic acid in 1:1 proportion for 20 s (± 0.25 s) [1] etching time and an etching temperature of 21 °C (± 1 °C).

Three types of etch pits (Type I, A, B) could be identified. Type I etch pits have a pseudo-hexagonal shape with a tiny hole in the middle and occur on irradiated surfaces. Width and length of the etch pits increase linear as a function of the etching time. Their areal density match the ion fluence applied. Therefore, Type I etch pits are designated as etch pits of etched ion tracks. The shape of Type A is similar to Type I but without a tiny hole. Type B etch pits differ significantly from Type I, they are more shallow, look like a flat depression on the crystal surface, and have no tiny hole. Minor amount of Type A and B etch pits occur on irradiated and non-irradiated areas. It is proposed that Type A and B etch pits represent etched dislocations.

To differentiate between etched ion tracks and dislocations calcite crystals have been re-heated to reveal possible differences in the annealing behavior of ion tracks and disloca-tions. Non-etched, ion-irradiated calcite samples were heated for 100 h at temperatures be-tween 200 – 500 °C. After heat treatment the samples were etched. The areal density of the etch pits Type I reduces dramatically between 240 and 260 °C from the fluence applied (10^6 ^{197}Au ions/cm^2) to a value of 0.04 * 10^6 etch pits/cm^{-2}. The only etch pits revealed above 260 °C are of Type A and Type B. For comparison, we exposed non-irradiated calcite crystals to the same annealing processes (100 h, 200–500 °C). The non-irradiated calcite crystal revealed the same areal density (0.04 * 10^6 etch pits/cm^2) at all temperatures in-cluding non-reheated samples. In conclusion, ion tracks in calcite anneal between 240 and 260 °C whereas dislocations do not anneal at the applied temperatures which provides a tool to differentiate between etched ion tracks and etched dislocations.

References

[1] D. MacDougall, P. B. Price, Attempt to Date Early South African Hominids by Using Fission Tracks in Calcite, Science 185, 943-944, (1974)

European Materials Research Society (EMRS), Straßburg, 2013

Swift heavy ion induced surface modification of calcite ($CaCO_3$) visualized by various techniques

Dedera, S. (1), Glasmacher, U.A. (1), Burchard, M.(1), Trautmann, C.(2), (3)
(1) University of Heidelberg, (2) Technical University Darmstadt, (3) GSI Darmstadt,

Natural calcite crystals were irradiated with 10^6 ^{197}Au ions/cm^2 of 11.1 MeV/u at the UNILAC, and with 1^{08} ^{238}U ions/cm^2 of ^{192} MeV/u at SIS18, GSI Darmstadt to create artificial surface and in depth damage. Prior to the experiment the surface of calcite crystals was covered with a hexagonal mask to create irradiated and non-irradiated areas.

Different approaches have been undertaken to visualize the damage caused by swift heavy ions: One possibility are etching techniques at which Na-Ethylenediaminetetraacetic acid (EDTA) + 0.5 - 5% Acetic acid in 1:1 proportion and highly diluted HNO_3 as etching so-lution turned out to be suitable and reproducible. The resulting etch pits show linear growth and have a size of about 12µm (±1) after 20s of etching (EDTA), respectively 15 µm (±2) after 4s of etching (HNO3). Etching has the advantages of visibility of the etch pits with an optical microscope and an easy control of size, shape and areal density of the etch pits.

Another approach to investigate surface modifications are spectrographical and advanced imaging methods. Different techniques have been tried out (Raman, IR, AFM, and SEM) of which raman spectroscopy provides the best results. Heavily irradiated areas show new, previously unknown bands correlating with decreasing established bands.

Workshop: Ionenstrahlen in Forschung und Anwendung, Leipzig, 2013

Dedera, S., U. A. Glasmacher, M. Burchard and C. Trautmann. “Mit Relativistischen Ionen Bestrahlte Karbonate- Bestrahlungs Und Charakterisierungsmethoden.” In Workshop Ionenstrahlphysik 2013. Leipzig, Germany, 2013

Without Abstract

Radiation Effects in Insulators, Helsinki, 2013

Swift Heavy Ion induced Surface Modification of Calcite ($CaCO_3$) visualized by Various Techniques

S. Dedera[1]*, U.A. Glasmacher[1], M. Burchard[1] and C. Trautmann[2,3]

[1]Institute of Earth Sciences, University of Heidelberg, Germany
[2]Department of Material Sciences, Technical University Darmstadt, Germany
[3]Gesellschaft für Schwerionenforschung Darmstadt, Germany
Email: Sebastian.Dedera@geow.uni-heidelberg.de

Natural calcite crystals (Iceland Spar, 12991 collection Heidelberg) were irradiated with 10^6 ^{197}Au ions/cm^2 of 11.1 MeV/u at the UNILAC, and with 10^8 ^{238}U ions/cm^2 of 192 MeV/u at SIS18, GSI Darmstadt to create artificial surface and in depth damage. Prior to the experiment the surface of calcite crystals was covered with a hexagonal mask to create irradiated and non-irradiated areas.

Different approaches have been undertaken to visualize the damage caused by swift heavy ions. One possibility is the application of etching techniques that have a long history in geosci-ences. First etching of calcite has been performed by Hones and Jones in 1937 [1] and Boos in 1942 [2] to reveal the crystal structure of calcite. Keith and Gilmann [3] tested in 1960 various etching solutions and indicated clearly the possibility to reveal localized etch pits. Sippel and Glover [4] described in 1964 the first successful etching experiments to reveal etch pits of spontaneous and induced fission tracks. From the huge amount of etching solutions used in these papers, Na-Ethylenediaminetetraacetic acid (EDTA) + 0.5- 5% Acetic acid in 1:1 pro-portion and highly diluted HNO_3 as etching solution turned out to be suitable and re-producible. The resulting etch pits show linear growth and have a size of about 12µm (±1) after 20 s of etching (EDTA), respectively 15 µm (±2) after 4 s of etching (HNO_3). Etching has the advantages of visibility of the etch pits with an optical microscope and an easy control of size and shape of the etch pits by using different etching solutions.

Another approach to investigate surface modifications, especially for the calcite irradiated with high energies at SIS18, are spectrographical and advanced imaging methods. Different tech-niques have been tried out (Raman, IR, UV/Vis, UV excitation, AFM, and SEM) of which Raman spectroscopy provides the best results. Heavily irradiated areas show new, previously unknown bands correlating with decreasing established bands.

[1] A. Boos, 1942. Ätzversuche an Calcit, Rhodochrosit und Siderit, N. Jahrbuch f. Mineralo-gie, 89-130.
[2] A.P. Honess, J.R. Jones, 1937. Etch figure investigations with optically active solvents. Bull. Geol. Soc. Am. 48, 667-722.
[3] R.E. Keith & J.J. Gilman, 1960. Dislocation Etch Pits and Plastic Deformation in Calcite", Acta Metallurgica 8.
[4] R.F. Sippel, E.D. Glover, 1964. Fission Damage in Calcite and the Dating of Carbonates. Sciences 144, 409-411.

Workshop Ionenstrahlen & Nanostrukturen, Paderborn, 2014

Lumineszenz - Experimentalplatz im Cave A am SIS, GSI Darmstadt

S. Dedera[a], U.A. Glasmacher[a], M. Burchard[a], C. Trautmann[b,c]
[a] Institut für Geowissenschaften, Universität Heidelberg
[b]GSI, Darmstadt
[c] Technische Universität Darmstadt
Sebastian.Dedera@geow.uni-heidelberg.de

Im Frühjahr 2014 wurde ein mobiler Lumineszenzstrahlplatz für das Cave A am SIS entwickelt, konstruiert und gebaut: Die Vorgaben an den Lumineszenzstrahlplatz waren unter anderem: spektroskopische und optische Überwachung der Proben. Das Ergebnis dieser Vorgaben ist ein PVC-Kubus (Abb.1) mit 10 cm Kantenlänge, 4 Zugängen für Mess- und Beobachtungsinstrumente, sowie einem flexiblem Probenhaltersystem.

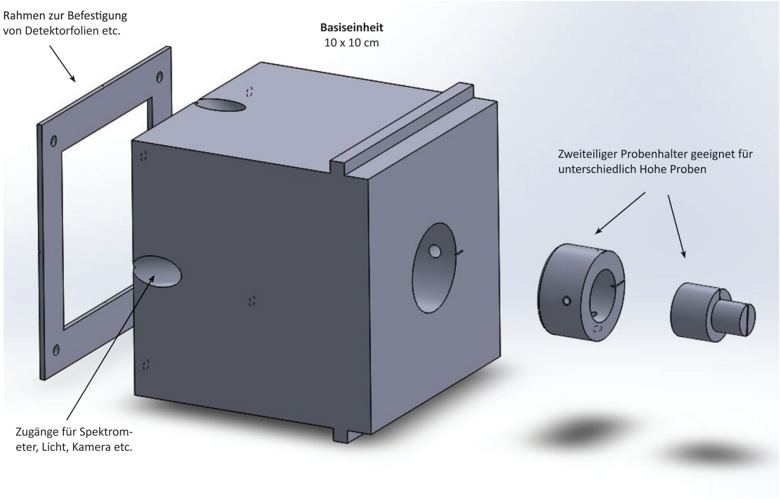

Abbildung 1: Neuentwickelter Lumineszenzstrahlplatz.

In Vorversuchen wurden im August 2012 Kalzitkristalle [$CaCO_3$] mit 1 x 10_{11} Ionen/cm^2 ^{238}Uran bei 192 MeV/n bestrahlt und dabei mit Hilfe der Überwachungskamera des Cave A eine starke Fluoreszenz und eine ausgeprägte Phosphoreszenz von mindestens 20 min festgestellt. Aufgrund dieser Eigenschaften wurde auch bei den Experimenten im März 2014 Kalzit gewählt um den neuen Lumineszenz - Experimentalplatz zu testen.

Die während und nach der Bestrahlung mit ^{208}Bi-Ionen (180 MeV/n) erfassten Daten zeigen eine rötliche Ionolumineszenz mit einem Maximum bei 616 nm. Nach der Bestrahlung mit einer Fluenz von ca. 1 x 10^9 Ionen/cm^2 lässt sich eine starke Phosphoreszenz mit 2 Abklingkurven beobachten: ein schnelles Abklingen, das nach etwa 7 min nicht mehr zu sehen ist und danach in ein Plateau übergeht, welches das langsame Abklingen repräsentiert. Dieses ist auch 50 min nach Abschalten des Strahles noch zu detektieren.

Prinzipiell sind mit dem neuen Lumineszenz - Experimentalplatz Untersuchungen von Festkörpern, Gasen und Flüssigkeiten unter variablen Temperaturen möglich.

Thermo, Charmonix, 2014

Visualization of neutron induced fission tracks in calcite

Sebastian Dedera[1], Ulrich A. Glasmacher[1], Michael Burchard[1]

[1] Institute of Earth Sciences, University of Heidelberg, Germany

An etching technique was developed to visualize ion tracks in calcite that are induced by irradiation with swift heavy U-ions of a total high energy of about 2.1 GeV [1-2] at the UNILAC, GSI Darmstadt. The next step was to develop an etching technique able to visualize fission tracks induced by ions of about 160 MeV energy, which is more similar to natural processes but about 13 times less than the total particle energy used at the UNILAC.

Therefore, in two experiments calcite crystals have been covered with (a) CN-5 uranium glass to check the areal density of fission tracks displayed on the calcite crystal (Fig.1), and (b) with a polished epoxy mount bearing zircon single crystals. These packages where irradiated with thermal neutrons (1 x 10^{15} neutrons/cm^2) at the FRM II in Munich to induce ^{235}U-based fission tracks with energies of about 160 MeV in the calcite crystal. To reveal the induced fission tracks the calcite crystals have been etched with the established etching procedures. The etching revealed clear defined etch pits of about 5 µm length and 4 µm width which are visible under an optical microscope. These etch pits are similar in shape than the etch pits caused by swift heavy ion irradiation (Fig 2).

The experiments proof that it is possible to visualize fission tracks in calcite. This technique might open a new branch of thermochronologic dating that provides a whole new archive: the U-bearing carbonate minerals and, therefore, carbonate rocks.

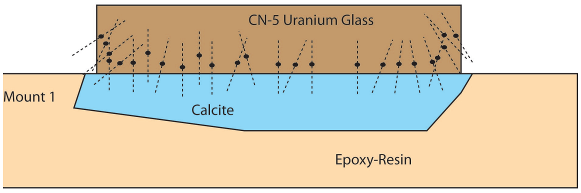

Figure 1: Sketch of the uranium glass – calcite experiment. The uranium glass is positioned directly on the polished calcite crystal and, therefore, provides a direct supply of fission tracks into the calcite.

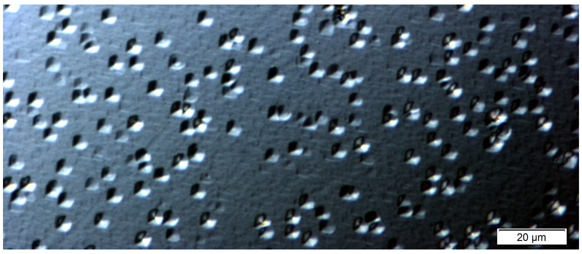

Figure 2: Etch pits on the calcite crystal surface. They have a pseudo-pentagonal shape and a size of about 5 µm in length and 4 µm in width.

References

1. Dedera, S., Glasmacher, U.A., Burchard, M. & Trautmann, C. Preparation of Carbonate Rocks for Irradiation with Swift Heavy Ions. (In Preparation)
2. Dedera, S., Glasmacher, U.A., Burchard, M. & Trautmann, C. Visualization of Heavy Ion Tracks in Calcite by EDTA etching techniques. (In Preparation)

Swift Heavy Ions in Insulators (SHIM), Darmstadt, 2015

In situ Raman Measurements of Calcite and Malachite during the Irradiation with Swift Heavy Ions

Sebastian Dedera[1], Ulrich A. Glasmacher[1], Michael Burchard[1], Daniel Severin[2], Christina Trautmann[2,3]
[1]Institute of Earth Sciences, University of Heidelberg, Germany;
[2]GSI, Darmstadt, Germany, 3Technische Universität Darmstadt, Germany

Raman spectroscopy is widely used in geosciences and materials research to characterize radiation damage caused by accelerated heavy ions or by fission fragments from natural radioactive decay processes. Ion beam induced modifications are typically analyzed long after the irradiation and outside of the irradiation chamber. To study the evolution of the material change with increasing fluence, the irradiation of a series of sample with swift heavy ions was necessary in the past.

Here we present a project designed to monitor online and in-situ Raman spectra prior, during, and shortly after ion irradiation. This approach has the advantage that the same sample location is analyzed for all fluences and thus a fluence series becomes independent of sample inhomogeneities and crystallographic orientation effects. A confocal Raman spectroscopic setup was developed and installed at the experimental irradiation chamber of the M3-beamline (UNILAC, GSI, Darmstadt). The system was tested by irradiating trigonal calcite ($CaCO_3$) with 4.8 MeV/u Au ions , (2 Hz, 1.2 ms pulse length) and monoclinic malachite ($Cu_2(CO_3)(OH)_2$) with 4.8 MeV/u Xe ions (5 Hz, 1.2 ms pulse length). The in-situ recorded Raman spectra indicate an increase of defect bands with increasing fluence and a significant change in amplitude and shape of the malachite Raman bands. We demonstrate that the new confocal Raman system is a powerful tool, to investigate changes of matter prior, during, and shortly after irradiation with swift heavy ions.

Eidesstattliche Versicherung gemäß § 8 der Promotionsordnung der Naturwissenschaftlich-Mathematischen Gesamtfakultät der Universität Heidelberg

1. Bei der eingereichten Dissertation zu dem Thema

Visualization of Ion-Induced Defects in Calcite

handelt es sich um meine eigenständig erbrachte Leistung.

2. Ich habe nur die angegebenen Quellen und Hilfsmittel benutzt und mich keiner unzulässigen Hilfe Dritter bedient. Insbesondere habe ich wörtlich oder sinngemäß aus anderen Werken übernommene Inhalte als solche kenntlich gemacht.

3. Die Arbeit oder Teile davon habe ich wie folgt/bislang nicht[1] an einer Hochschule des In- oder Auslands als Bestandteil einer Prüfungs- oder Qualifikationsleistung vorgelegt.

Titel der Arbeit:____

Hochschule und Jahr:______________________________________

Art der Prüfungs- oder Qualifikationsleistung:____________________

4. Die Richtigkeit der vorstehenden Erklärungen bestätige ich.

5. Die Bedeutung der eidesstattlichen Versicherung und die strafrechtlichen Folgen einer unrichtigen oder unvollständigen eidesstattlichen Versicherung sind mir bekannt.

Ich versichere an Eides statt, dass ich nach bestem Wissen die reine Wahrheit erklärt und nichts verschwiegen habe.

Ort und Datum Unterschrift

---

[1] Nicht Zutreffendes streichen. Bei Bejahung sind anzugeben: der Titel der andernorts vorgelegten Arbeit, die Hochschule, das Jahr der Vorlage und die Art der Prüfungs- oder Qualifikationsleistung.

12/2012